Majorana Zero Modes in Tubular Nanowires

Kristján Óttar Klausen

Dissertation submitted to the Department of Engineering at Reykjavík University in partial fulfillment of the requirements for the degree of Doctor of Philosophy

October 7, 2022

Thesis Committee:

Andrei Manolescu, Supervisor
Professor, Reykjavik University, Iceland

Sigurður I. Erlingsson, Co-supervisor
Professor, Reykjavik University, Iceland

Viðar Guðmundsson, Advisor
Professor, University of Iceland, Iceland

Examiner:

Habib Rostami,
Nordita Assistant Professor, Stockholm University, Sweden

To the clueless yet courageous youth,
that carefree dream and seek the truth.
To the wise and careful elders,
who guide, provide and shelter.

iv

Contents

List of Figures

Majorana Zero Modes in Tubular Nanowires

Kristján Óttar Klausen

Abstract

Majorana zero modes have recently been proposed as a solution to obtain fault-tolerant quantum computation. They are quasiparticle excitations in quantum systems at the nanoscale with the potential to function as qubits, the basic building blocks of quantum computers. Their topological properties hold promise to counter the decoherence problem, where quantum coherence is lost due to coupling with the environment, which is one of the main challenges for upscaling the number of qubits in a quantum computer. In this work, Majorana zero modes in core-shell nanowire systems are investigated. Core-shell nanowires are tubular conductors that commonly have polygonal cross-section geometry due to crystallographic qualities. Semiconductors with proximity-induced superconductivity, large g-factors and Rashba spin-orbit coupling, can be tuned by an external magnetic field to host Majorana zero modes. Corner-localization of the lowest energy states in polygonal core-shell nanowires allows for hosting multiple Majorana zero modes within a single nanowire system. Three-dimensional nanowires are modeled using the Bogoliubov-de Gennes Hamiltonian, which is solved numerically by diagonalization. Effects of variable core and shell geometry are analyzed and triangular wires with hexagonal cores are found to have particularly large energy separations between the first and second groups of energy states, which is favorable for experimental hosting of Majorana zero modes. Braiding in such a system is discussed and for the realization of real space braiding, a dual core wire is suggested to include the necessary degrees of freedom for the simplest non-commutative braiding operation. The relation between Andreev reflection and propagation of the superconductivity property is studied by modeling partially proximitized wire shells, with radial, angular and longitudinal interfaces, corresponding to common experimental platforms. Varying compatibility is found with Andreev reflection. Flux-periodic oscillations in the energy spectra of proximitized shells are explored along with the effects of geometry, Zeeman and spin-orbit interaction. Instances are shown where the periodicity of the lowest energy state is found to separately display normal, superconducting and fractional flux quanta. To gain insight into the structure of topological invariants, the first Chern number in particular, Stokes' theorem for bivector-valued fields is analyzed and visualized using geometric calculus. The findings show how the multiple components necessary for the emergence of Majorana zero modes each have complex subtleties and interdependencies, and in what way they should be investigated to come closer to the technological realization of Majorana zero modes.

Keywords: Majorana, nanowires, superconductivity, topological order.

Acknowledgments

Without the support of my wife's uncle and dear friend Guðni Ólafur Brynjólfsson (Olli), I never would have embarked on this journey. Takk fyrir stuðninginn Olli. My career plan after the masters program was to become an electrician due to my fascination with electromagnetism. I had just started living with my wife at Olli's place, a two apartment house in Reykjavík, when an opportunity for a Ph.D. opened up. I was hesitant however to begin a Ph.D. program since the reaction of most people when I told them I was considering so, can be summarized by this quote from a colleague at the time: "Why do you have a need to torture yourself?". I sought Olli's guidance on the matter and he firmly gave me the following advice: "One must become proficient in that which he has undertaken". This struck me, as a Ph.D. is a necessary step towards becoming proficient in physics.

My M.S. supervisor Viðar Guðmundsson encouraged me in a similar manner. I told him of my plans of becoming an electrician so I could better understand what could be done with electromagnetism in practice. Viðar responded that indeed such practical knowledge is beneficial but a man with questions like mine must go forward in physics. Thank you Viðar for watching over me.

Therefore, thanks to encouragement by elders and mentors, I applied for the Ph.D. position, researching Majorana Zero Modes in tubular nanowires under the supervision of Andrei Manolescu and Sigurður I. Erlingsson.

Thank you Andrei for your patience and support. I have learned a great deal from your experienced outlook on many aspects of physics.

Thank you Siggi for the pointers, insights and lectures. Your down to earth approach to physics has been a refreshing wind in the program.

I had the pleasure of working alongside Anna Sitek, a visiting professor from Wrocław University of Science and Technology, dziękuję Anna for all of the help.

I thank the Lord for the GNU community as Gfortran, Kubuntu, LaTeX and Gnuplot were all invaluable tools in this endeavor.

Last but not least, I would like to thank my wife Kristrún for all of her support, warmth and understanding.

Chapter 1

Introduction

Recent advances in fabrication of materials at the nanoscale have made the building blocks of quantum computers a realistic possibility. The quest to create quantum computers has been likened to the Space Race in the 20th-century, since encryption of government data is based on a problem that quantum computers can solve with much more ease than standard computers [1].

The qubit forms the basis of a quantum computer and experimentally realizing a system of multiple qubits is necessary for quantum computation. A promising candidate for a stable qubit are Majorana zero modes (MZM), also known as Majorana bound states [2], which have been shown to be have capabilities for fault-tolerant quantum computation [3]. Recently the Nanophysics Center at Reykjavik University published novel results of MZM being hosted in prismatic core-shell nanowires [4,5]. The current project was motivated by that research. Its aim was to investigate the stability of multiple MZM in prismatic tubular nanowires and dependent interactions, to answer the research question if such nanowires are suitable for their hosting and manipulation.

Majorana zero modes get their name from the Italian physicist Ettore Majorana. In the year 1937 he published a paper with a solution of the Dirac equation describing neutral particles which were their own antiparticles, thus annihilating each other on contact [6]. Particles with this property have since been called Majorana fermions [7]. In superconductors, mixed states of electrons and holes can emerge as quasiparticle excitations behaving in a similar way [8]. The phenomena that exactly mimics Majorana fermions are zero energy states, known as Majorana zero modes (MZM), localized near defects or boundaries in topological superconductors [9]. MZM are an example of Ising anyons which have non-commutative exchange statistics, an essential feature for fault-tolerant topological quantum computation [10].

The word *topological* refers to a phase of matter which is stable with respect to perturbations of the bulk and depends only on the properties of the boundary [11].

Systems with topological phases of matter, offer the possibility of topological invariants in the energy spectrum and play a prominent part in the current race for quantum computation [12, 13]. By closing and reopening of gaps in the energy spectra, edge states emerge, which are robust to environmental perturbations [14, 15]. Topological superconductors can be engineered by combining standard superconductors with semiconductors [8]. Semiconductor nanowires with proximity induced superconductivity have become key elements in various platforms proposed to realize qubits and other evolving technologies at the quantum scale [16–18]. Currently one of the most promising platforms for realizing MZM are hybrid superconductor-semiconductor devices [19]. When a metal comes in contact with a superconductor, the superconductivity can be said to leak into the metal making it superconducting up to a certain depth. This process of proximity-induced superconductivity is one of three necessary ingredients, along with Zeeman splitting and strong spin-orbit coupling, for engineering topological superconductors [8].

Core-shell nanowires are radial heterojuctions consisting of a core which is enveloped by one or more layers of different materials. Due to the crystallographic structure they usually have polygonal cross sections [20–34], but circular wires have also been fabricated [35]. Using a conducting material for the shell and an insulating one for the core, a single wire becomes a prismatic tubular conductor. Sharp corners of the cross section impose non-uniform electron localization along the circumference of the tube so that low energy electrons are accumulated in the vicinity of sharp edges, while carriers of higher energy are shifted to the facets [36–39]. If the shell is very thin then the low-energy electrons are depleted from the facets and the shell becomes a multiple-channel system consisting of well-separated 1D electron channels situated along the edges. Due to their unique localization and a variety of other interesting properties, core-shell nanowires have been extensively investigated in the last two decades [40, 41], showing promise in multiple applications such as lasers [42], energy harvesting devices [43, 44] and photovoltaics [45]. By n-doping of a semiconductor shell, the chemical potential can be moved into the conduction band such that electrons become the only charge carriers and the shell behaves effectively as a metal with the effective mass of the semiconductor. Earlier investigations have indicated that due to 1D electron channels along the sharp edges of prismatic tubes, multiple Majorana zero modes can be hosted in a single core-shell nanowire [4, 46]. However only if the electron-hole coherence length is larger than the whole structure, can the shell be considered fully proximitized and electron-hole coherence can be expected to be uniform.

Experimental evidence of MZM in a nanowire system was considered to be found in the year 2012 [47] and further demonstrated in the year 2018 within a full-shell nanowire system [48]. In the past few years a multitude of systems have been proposed and tested both theoretically and experimentally. However, concerns emerged in 2020 that experimental signatures may have been over-interpreted [49] as other physical phenomena such as Andreev bound states, could result in a zero-bias con-

ductance peak, which was considered to be one of the main experimental signatures of MZM. What the field is calling for now is more fundamental research of the complex interactions occurring in the hybrid systems [13]. The current work includes several attempts to answer that call.

In the following sections of this introductory chapter, foundational concepts of topology in condensed matter systems are defined, with respect to the development leading up to the pursuit of MZM in nanowires. Chapter 2, based on [50], covers the basics of superconductivity theory to motivate and define the Bogoliubov-de Gennes equations, which allow for the description of proximity induced superconductivity in the nanowire model and calculation of excited quasiparticle states. Original results from numerical simulations of the core-shell system are presented in Chapters 3 to 5. In Chapter 3, the effects of variable core and shell geometry on the hosting and stability of Majorana zero modes in hexagonal and triangular nanowires are investigated. Moreover, braiding in the nanowire end plane is discussed and the necessity for a dual core wire argued [46]. Chapter 4 explores Andreev reflection and electron-hole coherence within a partially proximitized shell of a core-shell nanowire. Three cases of radial, angular and longitudinal partial proximitization are studied, comparable to common platforms for hosting Majorana zero modes [51]. Magnetic flux-periodic oscillations in proximitized core-shell nanowires are explored and compared with the Little-Parks oscillations in Chapter 5. In order to gain insight into the structure of topological invariants, the first Chern number in particular, geometric algebra is used to visualize the boundary theorem of geometric calculus for bivector valued fields in Chapter 6. A brief summary of the work and conclusions are found in Chapter 7.

1.1 Quantum computers

Quantum computers are based on *qubits* as opposed to bits, the information building blocks of classical computers. A standard bit can have two values, zero or one, whereas the qubit is a linear combination of two states, spanning a two dimensional state space which can be graphically represented by the Bloch sphere, Fig. 1.1, where a pure state of the qubit can take any value of a point on the surface of the two dimensional spherical shell. Instead of having either the value zero or one as in the case of the classical bit, the qubit can be a superposition of the two,

$$|\psi\rangle = \zeta|0\rangle + \eta|1\rangle, \tag{1.1}$$

where $\zeta, \eta \in \mathbb{C}$. The graphical representation of states as points on the surface of a sphere, Fig. 1.1, suffices even though ζ, η are complex numbers due to the probability axiom

$$|\zeta|^2 + |\eta|^2 = 1. \tag{1.2}$$
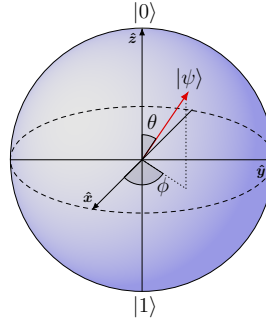
Figure 1.1: The Bloch sphere.

The information capacity of multiple classical bits scales as n^2 where n is the number of bits. The information capacity of qubits however scales as 2^n. Proof by induction shows that $2^n > n^2$ for $n \geq 5$.

By writing the qubit as a vector, quantum logic gates can be written as matrix transformations acting on the qubit. Taking the NOT gate, X, as an example,

$$X \begin{bmatrix} \eta \\ \zeta \end{bmatrix} = \begin{bmatrix} 0 & 1 \\ 1 & 0 \end{bmatrix} \begin{bmatrix} \eta \\ \zeta \end{bmatrix} = \begin{bmatrix} \zeta \\ \eta \end{bmatrix}, \tag{1.3}$$

which interchanges $|0\rangle$ and $|1\rangle$. The normalization condition must be conserved by the operation, so any qubit transformation T has to be unitary, $TT^{\dagger} = I$, where I is the identity matrix. The NOT gate can be recognized as the Pauli matrix σ_x and together with the other two,

$$\sigma_y = \begin{bmatrix} 0 & -i \\ i & 0 \end{bmatrix} \text{ and } \sigma_z = \begin{bmatrix} 1 & 0 \\ 0 & -1 \end{bmatrix}, \tag{1.4}$$

forms the Pauli group of gates X, Y, Z corresponding to π rotations around the denoted axis on the Bloch sphere [52]. The Pauli group is a subgroup of the Clifford group C_n, which is an n-qubit subgroup of $U(2^n)$. The Clifford group is generated by the Hadamard gate H and phase gate S acting on a single qubit along with the qubit pair gate CNOT $\Lambda(\sigma_x)$, where

$$H = \frac{1}{\sqrt{2}} \begin{bmatrix} 1 & 1 \\ 1 & -1 \end{bmatrix}, S = \begin{bmatrix} 1 & 0 \\ 0 & i \end{bmatrix} \text{ and } \Lambda(\sigma_x) = \begin{bmatrix} I & 0 \\ 0 & \sigma_x \end{bmatrix}. \tag{1.5}$$

These three gates combined with the phase-shift T gate,

$$T = \begin{bmatrix} 1 & 0 \\ 0 & e^{\frac{i\pi}{4}} \end{bmatrix}, \tag{1.6}$$

form a set for universal quantum computation, so that any unitary operation can be expressed by an appropriate combinations of these gates [52–54].

Quantum computers are not necessarily more efficient that classical computers in all cases but for certain algorithms, the speedup in calculations can be substantial. Grover's algorithm [55] results in a quadratic speedup of finding an element with specified properties within an unknown search space, demonstrating how quantum search algorithms can be faster than its classical counterpart. Shor's algorithm [56], based on the quantum Fourier transform [57], provides an exponential speedup in computing discrete logarithms and prime factoring of integers - both of which are used in cryptography. In the event of a fabrication of a powerful multi qubit quantum computer, classic cryptographic methods may be at risk, which is fuelling research into post-quantum cryptography [58].

The most evident practicality of quantum computers is simulating quantum systems more efficiently [59]. Breakthroughs across multiple fields such as molecular modelling, artificial intelligence and meteorology have been theorized by the use of quantum computers. At the time of writing, the 127-qubit IBM Eagle is the most powerful quantum processor made to date, Fig. 1.2. It is based on the superconducting charge transmon qubit [60].
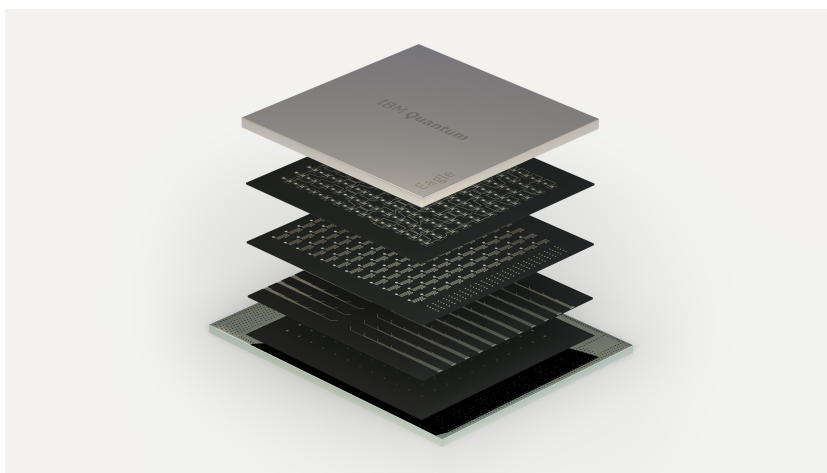
Figure 1.2: The 127-qubit quantum processor by IBM [61].

The IBM Quantum System One, Fig. 1.3, was the first circuit based quantum computer presented for commercial purposes in 2019 and contains 20-qubits. Dr. Matthias Troyer at Microsoft's quantum computing division recently stated [62] that around 50 thousand qubits are needed to enter the commercial regime of quantum computing, where real benefits can be reaped. In that light, quantum computers are not to be expected in the coming years, but rather in the coming decades.
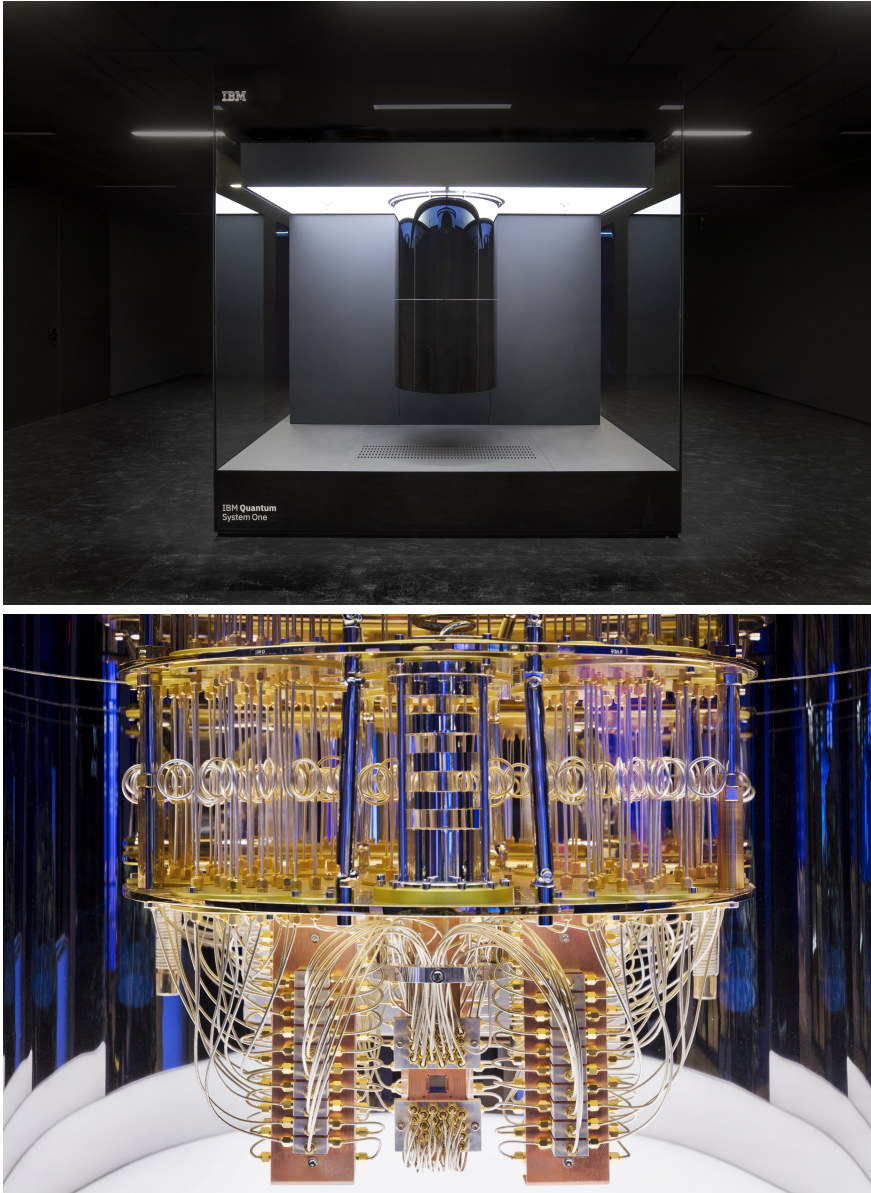
Figure 1.3: Quantum System One by IBM in Ehningen, Germany. Exterior view [63] (upper panel) and interior view [64] (lower panel).

One of the main challenges in fabricating large scale quantum computers in decoherence, in which the superposition state of qubits is lost due to external perturbations. Another challenge is accumulation of errors in repeated applications of quantum gates [65]. The latter can be countered by quantum error-correction codes [66] but the former by isolation of the system from the environment. Perfect isolation of a system is practically unfeasible however, as the system has to be interacted with to obtain an outcome following a computation.

Remarkably, both problems of decoherence and error accumulation can be solved by implementing topologically protected qubits [67]. As an illustrative example of topological protection, consider a knot on a string, Fig. 1.4. The knot is robust with respect to perturbations of the string as the string can be moved, shaken, twisted, pulled on, heated and cooled to a certain degree - all without influencing the knot. Furthermore, operations on the knot itself such as adding a crossing are independent of the state of the string. The prime knots in Fig. 1.4 are topologically distinct, as one can not be continuously deformed into another. To add a loop or crossing, the string will have to be cut.
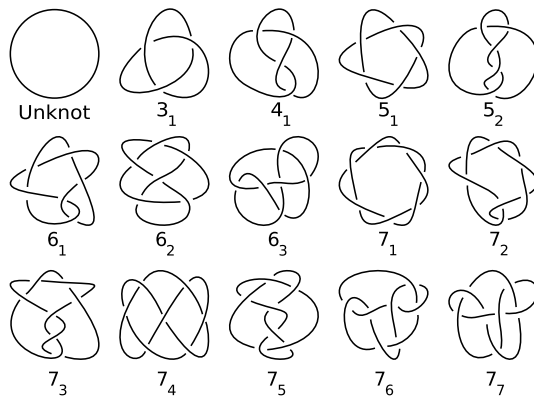
Figure 1.4: The unknot and the prime knots with up to seven crossings. Public domain image.

Knots in strings as well as holes in manifolds are familiar examples of topological invariants. Generally, that which is invariant with respect to a continuous deformation of system is a topological invariant. In an analogous manner, bound states of certain Hamiltonians are topological invariants in the energy spectrum, which can also have the potential for fault-tolerant quantum computation [15].

1.2   Continuous transformations of physical systems

Continuous deformations of a physical system can be described by continuous transformations of its Hamiltonian. The Hamiltonian $\hat{H}$ describes the total energy of a system, its eigenvalues E_n give the energy spectrum of the system and its eigenvectors $|n\rangle$ provide a basis for the state space. Consider a system described by a Hamiltonian $\hat{H}(\mathbf{r})$ that is adiabatically transformed by variation of a given parameter $\mathbf{r}(t) = \mathbf{r}_t$, in a time interval from $t = 0$ to $t = T$ such that $\mathbf{r}(0) = \mathbf{r}(T)$. In the parameter space, this amounts to a transportation around a closed loop, C [68]. At each instant the eigenstates of the system $|n(\mathbf{r}_t)\rangle$, satisfy

$$\hat{H}(\mathbf{r})|n(\mathbf{r})\rangle = E_n(\mathbf{r})|n(\mathbf{r})\rangle \,. \tag{1.7}$$

The time evolution of the state vector, $|\psi(t)\rangle$ is described by Schrödinger's equation,

$$\hat{H}(\mathbf{r}_t)|\psi(t)\rangle = i\hbar|\psi(t)\rangle \,. \tag{1.8}$$

Although the end point equals the initial point following the transformation along the closed loop C, the state acquires a phase factor

$$|\psi(t)\rangle = e^{i\alpha}|n(\mathbf{r}_t)\rangle, \tag{1.9}$$

which is composed of two distinct scalar valued parts [68], $\alpha = \beta + \gamma$. The temporal dynamical phase is given by

$$\beta_n = -\frac{1}{\hbar}\int_0^T E_n(\mathbf{r}_t)\,dt \,, \tag{1.10}$$

whilst the spatial geometric phase, also known as the Berry phase, is

$$\gamma_n(C) = i\oint_C \langle n(\mathbf{r}_t)|\nabla_{\mathbf{r}}\,n(\mathbf{r}_t)\rangle \cdot d\mathbf{r} \,. \tag{1.11}$$

Geometric phases have been found to describe a plethora of phenomena in various systems such as electric polarization and the quantum Hall effect [69, 70]. They have been shown to be conceptually equal to the mathematical notion of holonomy [71]. Fig. 1.5(a) shows an example of geometric holonomy, where a tangent vector transported along a closed path on the surface of a sphere obtains a phase θ induced by the curvature of the sphere. A similar phenomena is found in complex analysis of the logarithmic function [72], Fig. 1.5(b). To describe how the vector changes as it is parallel transported along the curve, a geometric *connection* is defined which is a covariant derivative that prescribes in what way the vector changes with respect to transport along the curve.
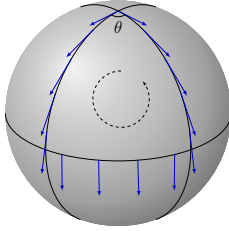
(a) A tangent vector parallel transported along a closed curve on the surface of a sphere aquires a phase θ which is the holonomy of the affine connection.
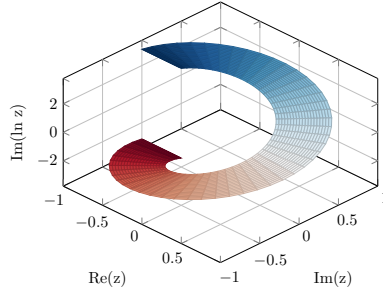
(b) Complex component of the complex logarithm on the principal branch $\theta \in [-\pi, \pi]$ for $r \in [0.5, 1]$.

Figure 1.5: Examples of holonomy for curved (a) and flat (b) connections.

In the same way the Berry connection,

$$\mathbf{A}_n(\mathbf{r}) = i\langle n(\mathbf{r}_t)|\nabla_\mathbf{r}\, n(\mathbf{r}_t)\rangle, \tag{1.12}$$

describes how the eigenvectors transform with respect to the transformation in the parameter space. This leads to the following expression for the geometric phase, which has the same form as the Aharonov-Bohm phase,

$$\gamma_n(C) = \oint_C \mathbf{A}_n \cdot d\mathbf{r}\,. \tag{1.13}$$

The Berry connection is a vector potential for the gauge-invariant Berry curvature,

$$\mathbf{B}_n(\mathbf{r}) = \nabla_\mathbf{r} \times \mathbf{A}_n(\mathbf{r}), \tag{1.14}$$

which is analogous to a magnetic field in the parameter space. This analogy has been shown to hold with respect to Faraday's law of electromagnetic induction, as the time derivative of the Berry curvature of Bloch bands induces a motive force on wavepackets within unit cells of a crystal lattice [73–75]. Interestingly, near a twofold degeneracy of an energy state, $E_n = E_m$, the Berry curvature takes a form identical to a magnetic monopole [68, 70],

$$\mathbf{B}_m(\mathbf{r}) = \frac{1}{2}\frac{\mathbf{r}}{r^3}\,. \tag{1.15}$$

To understand why the monopole structure emerges in the parameter space, consider an electron in a magnetic field where the energy of aligned and anti-aligned spin differ. If the energies of the two converge in parameter space, two anti-parallel magnetic moments coexists in that point, necessitating a magnetic monopole.

Integrating the Berry curvature over a two dimensional surface $S = \partial V$ in the parameter space, containing a degeneracy point, results in a topological invariant

$$\oiint_S \mathbf{B}_m \cdot d\mathbf{S} = \iiint_V \nabla \cdot \mathbf{B}_m \, dV = \frac{4\pi}{2} = 2\pi, \qquad (1.16)$$

as this integral value is invariant with respect to deformations of S. The divergence of $\mathbf{B}_n$ is zero everywhere except the origin wherein the degeneracy singularity can be seen as a hole of sorts. This kind of a topological invariant is well known in algebraic topology as the first Chern number, C_1 [76] and in general

$$C_1 = \frac{1}{2\pi} \oiint_S \mathbf{B}_N \cdot d\mathbf{S} = N \in \mathbb{Z}, \qquad (1.17)$$

where N is the number of monopoles of strength $\pm \frac{1}{2}$ within S.

From here we can deduce the notion that physical systems are topologically equivalent if their Hamiltonians can be continuously deformed into one another, without crossing such a degeneracy point. This also implies the need for a gap in the energy spectrum in order for such a gap closing to occur.

If an energy state E_n is d-fold generate the Berry connection becomes a $d \times d$ vector-valued matrix [77], and therefore non-commutative (non-Abelian) with elements

$$[\mathcal{A}_n]_{ab}(\mathbf{r}) = i\langle n_a(\mathbf{r}_t)|\nabla_\mathbf{r} n_b(\mathbf{r}_t)\rangle, \qquad (1.18)$$

where a and b are basis labels within the degeneracy eigenvector subspace $|n_d\rangle$. The Berry curvature generalizes to a tensor with the following components [78],

$$[\mathcal{F}_{\mu\nu}]_{ab} = (\partial_\mu A_\nu - \partial_\nu A_\mu)_{ab} + i([A_\mu, A_\nu])_{ab}. \qquad (1.19)$$

This expression reduces to (1.14) in the case of no degeneracies, $a = b = 1$ and commuting elements of the Berry connection. The non-Abelian Berry phase becomes

$$U_n(C) = \mathcal{P} \exp\left(\oint_C \mathcal{A}_n \cdot d\mathbf{r}\right) \qquad (1.20)$$

where $\mathcal{P}$ denotes path-ordering, necessitated by the non-commutativity of $\mathcal{A}_n$ [8]. In the same way that the Abelian Berry connection is analogous to the $U(1)$ symmetric magnetic vector potential, the non-Abelian Berry connection can give rise to higher dimensional gauge potentials [77]. The group $U(n)$ consists af all complex valued $n \times n$ matrices, unitary and closed under matrix multiplication. The $SU(n)$ group has the additional property of determinant one [79]. The electromagnetic interaction in quantum mechanics arises from scalar phase symmetry of the wavefunction, whilst more complex local gauge symmetries are necessary to describe other fundamental

interactions such as $SU(2)$ for the electroweak interactions of quarks [80]. In $SU(2)$ gauge symmetry, the phase factor generalizes to $e^{i\boldsymbol{\alpha}\cdot\boldsymbol{\tau}}$, where three phase angles form the vector $\boldsymbol{\alpha} = (\alpha_1, \alpha_2, \alpha_3)$ and $\boldsymbol{\tau} = (\tau_1, \tau_2, \tau_3)$ is a matrix valued vector consisting of,

$$\tau_1 = \frac{1}{2}\begin{bmatrix} 0 & 1 \\ 1 & 0 \end{bmatrix}, \tau_2 = \frac{1}{2}\begin{bmatrix} 0 & -i \\ i & 0 \end{bmatrix} \text{ and } \tau_3 = \frac{1}{2}\begin{bmatrix} 1 & 0 \\ 0 & -1 \end{bmatrix}, \tag{1.21}$$

which can be recognized as the Pauli matrices (1.3), (1.4), times a factor 1/2. From here arises the idea of using non-Abelian Berry phases for quantum computation [81]. Using the subspace of degenerate energies, quantum information can be encoded and operated on by the $SU(n)$ phases of the holonomy [81]. As a simple example of such a non-trivial phase factor, let $\boldsymbol{\alpha} = (2\theta, 0, 0)$. Then $\boldsymbol{\alpha}\cdot\boldsymbol{\tau} = \theta\sigma_x$ and the phase factor becomes

$$e^{i\boldsymbol{\alpha}\cdot\boldsymbol{\tau}} = \exp\left(i\theta\sigma_x\right) = \mathbb{1}\cos(\theta) + i\sigma_x\sin(\theta) = \begin{bmatrix} \cos(\theta) & i\sin(\theta) \\ i\sin(\theta) & \cos(\theta) \end{bmatrix}. \tag{1.22}$$

1.3 Topological quantum computation

In a seminal paper, Kitaev [15] proposed using non-Abelian anyons as a means for fault-tolerant quantum computation. Anyons are two-dimensional quasiparticles with non-trivial exchange statistics. In three dimensions, the effect of interchanging two particles is dictated by the spin-statistics theorem where particles are either integer spin bosons or half-integer spin fermions. The interchange of particles results in a phase factor,

$$|\Psi_{ab}\rangle = e^{i\theta}|\Psi_{ba}\rangle, \tag{1.23}$$

where bosons correspond to $\theta = 0$ and fermions to $\theta = \pi$. In both cases, a double exchange returns the system to its initial state. For anyons however, the phase can in theory take an arbitrary value [67] so that

$$|\Psi_{ab}\rangle \rightarrow e^{i2\theta}|\Psi_{ab}\rangle \neq |\Psi_{ab}\rangle. \tag{1.24}$$

Non-Abelian anyons have the additional property that the order of their exchange matters [3] and their exchange phase is of the non-Abelian kind discussed in the previous section. Therefore, quantum logic gates (1.5) can be encoded by moving non-Abelian anyons around one another, effectively braiding their world lines [82]. A particle in space traces out a curve in spacetime, termed worldline. Exchanging the location of two anyons traces out a crossing of their worldlines. The worldlines of a system with three non-Abelian anyons form a basis for the three strand braid group, Fig. 1.6. By various brading operations in a system of multiple non-Abelian anyons, quantum computation can be implemented [67].
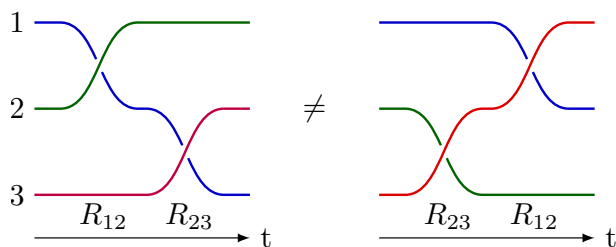
Figure 1.6: Non-commutative property of the three strand braid group.

In order for anyonic exchange statistics to emerge, the particles have to be confined to a plane [83] and can be considered to exists in (2+1) spacetime. In a system of two particles, consider moving one around the other along a closed path C_1, Fig. 1.7. The position of each particle forms a singularity in their joint configuration space. The loop C_1 can not be continuously deformed to the loop C_2 without crossing over the blue particle, if the transformation is confined to the plane of the loop. In three space dimensions however, the loop could be deformed above the blue particle. Looping one particle around the other can be done both clockwise and counter clockwise with the winding number taking integer values in $\mathbb{Z}$ [83].
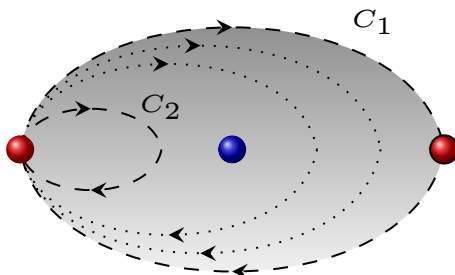
Figure 1.7: Emergence of the first homotopy group in particle exchange paths confined to a plane (shaded).

As so often is the case for applications of mathematical concepts in physics, mathematicians have long ago categorized and generalized the phenomena of winding something around another thing, as homotopy groups [79]. Informally, the ways of winding n-dimensional spheres around a space X is denoted by the fundamental homotopy group $\pi_n(X)$. As an example, winding a rubber band around a sphere will always result in a trivial loop as the rubber band can slide of the sphere, therefore $\pi_1(S^2) = 0$ where S^2 denotes a sphere. However, a plane can be wrapped around a sphere infinitely often both clockwise and counter-clockwise, $\pi_2(S^2) = \mathbb{Z}$. A common example from everyday life is wrapping something in a bag multiple times by re-

peatedly twisting and folding the bag over the object. The connection between topology and the fundamental homotopy group lies in the fact that a topological space X has a hole with an $n-$dimensional boundary, if and only if an $n-$dimensional sphere can not be shrunken to a point everywhere within it [79], in which case $\pi_n(X) \neq 0$.

Remarkably, the kind of systems which can be expected to host topological states can be mapped out by considering all possible symmetries of Hamiltonians [84]. The topological invariants emerge as homotopy groups of defects, described by $\pi_0(X)$ where X is the classifying space of the Hamiltonian, see Appendix A. The non-trivial value $\pi_0 \neq 0$ denotes that there is an interval (hole with a zero-dimensional boundary) in the parameter space of the Hamiltonian, separating two topologically distinct phases of the system.

1.4 Majorana fermions and zero modes

Topological phase transitions are phase transitions not described by symmetry breaking and were considered as early as the seventies in terms of two dimensional lattices in strong magnetic fields [85]. Topological order has been found to be necessary to understand critical features of a wide range of phenomena such as high-temperature superconductivity and the quantum Hall effect [86]. In searching for more systems with topological order, Kitaev [87] proposed a simple 1D model of a proximitized wire known as the Kitaev chain, consisting of electrons with fixed spin and a gapped energy spectrum. The Hamiltonian can be written as the sum over all j-sites in terms of fermionic annihilation and creation operators, a_j and $a_j^\dagger$ respectively,

$$H_1 = \sum_j \left(-t(a_j^\dagger a_{j+1} + a_{j+1}^\dagger a_j) - \mu(a_j^\dagger a_j - 1/2) + \Delta a_j a_{j+1} + \Delta a_{j+1}^\dagger a_j^\dagger \right), \quad (1.25)$$

where t denotes the hopping energy, μ the chemical potential and $\Delta = |\Delta|e^{i\theta}$ is the induced superconducting gap. By rewriting the Hamiltonian (1.25) in terms of Majorana operators with the superconducting phase embedded,

$$\gamma_{2j-1} = e^{i\theta/2}a_j + e^{-i\theta/2}a_j^\dagger \text{ and } \gamma_{2j} = -ie^{i\theta/2}a_j + ie^{-i\theta/2}a_j^\dagger, \quad (1.26)$$

the Hamiltonian takes the form

$$H_1 = \frac{i}{2} \sum_j \left(-\mu\gamma_{2j-1}\gamma_{2j} + (t + |\Delta|)\gamma_{2j}\gamma_{2j+1} + (-t + |\Delta|)\gamma_{2j-1}\gamma_{2j+2} \right). \quad (1.27)$$

Depending on the strength of the hopping amplitude t and value of the chemical potential μ, the Majorana operators either couple within each site separately or between adjacent sites, in which the Majorana operator at each end becomes unpaired. In this way the Kitaev chain has a trivial phase, Fig. 1.8(a) and a non-trivial phase, 1.8(b).

(a) $\mu < 0, t = |\Delta| = 0$:

(b) $\mu = 0, t = |\Delta| > 0$:
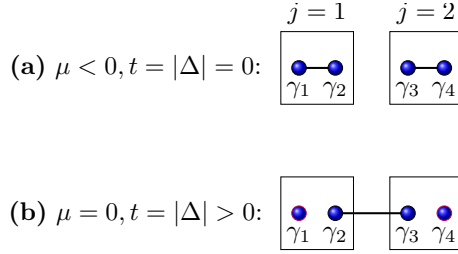
Figure 1.8: Minimal example of topologically distinct phases of the Kitaev chain [87]. Only two sites are shown as the properties hold for n-sites due to translational invariance. (a) Trivial phase of the Kitaev chain, with no unpaired Majorana zero modes. (b) Topological phase of the Kitaev chain with unpaired Majorana zero modes at the boundaries.

The non-trivial phase is onset at $\mu = 0$ where the Majorana end pairs become degenerate zero energy states, hence the name Majorana zero modes. As the non-trivial phase can not be entered without closing the energy gap the two phases are topologically distinct, in line with the theory set forth in the preceding sections. The topological invariant of the Kitaev chain is labeled with the two element set $\mathbb{Z}_2 = \{0, 1\}$, denoting the trivial and topological phase, respectively. The notation comes from the quotient group $\mathbb{Z}_2 = \mathbb{Z}/(2\mathbb{Z}) = \{0, 1\}$ which can be explained as the set of remainders following division of an element from $\mathbb{Z}$ by an element from $2\mathbb{Z}$, which is zero for even numbers and one for odd numbers.

As there is no planar confinement in the Kitaev chain, the system is not sufficient for quantum computation but the edge states can in theory function as a quantum memory [87]. Majorana zero modes have been shown to emerge from vortices in planar systems as well [88] but in both proposals, a specific type of superconductivity is needed to fix the spin degree of freedom. In particular, p-wave superconductivity is needed as opposed to the more standard s-wave superconductivity [89]. The difference is similar to the difference between s- and p-orbitals of atoms, in that they differ by a quanta of angular momentum. In s-wave superconductivity, the long-range pairing responsible for the superconducting property has a spin singlet basis

$$|s\rangle_s = |\uparrow\downarrow - \downarrow\uparrow\rangle, \tag{1.28}$$

whilst in p-wave superconductivity a spin-triplet basis emerges [90] where parallel spin pairing is allowed for,

$$|s\rangle_p = |\uparrow\uparrow\rangle + |\downarrow\downarrow\rangle + |\uparrow\downarrow + \downarrow\uparrow\rangle. \tag{1.29}$$

To see why the spin alignment is required for Majorana zero modes to begin with, consider the properties of the Majorana operators in general. The Majorana operators

γ are anti-commutative (non-Abelian) [13], for a pair γ_1 and γ_2 we have

$$\gamma_1\gamma_2 = -\gamma_2\gamma_1. \tag{1.30}$$

Generally stated,

$$\{\gamma_i^A, \gamma_j^B\} = \gamma_i^A\gamma_j^B + \gamma_j^B\gamma_i^A = 2\delta_{ij} \tag{1.31}$$

where δ_{ij} is the Kronecker delta

$$\delta_{ij} = \begin{cases} 0 & \text{if } i \neq j, \\ 1 & \text{if } i = j. \end{cases} \tag{1.32}$$

In accordance with the definition of the Majorana fermions being their own anti-particle, the γ-operators fulfill the Majorana condition

$$\gamma = \gamma^\dagger, \tag{1.33}$$

which requires Majorana fermions to be charge neutral. Furthermore, this condition implies that a pair of Majorana states will annihilate on contact. In this way, Majorana zero modes can be fused together resulting in either the vacuum or an unpaired fermion, in a system of degenerate zero modes, depending on the occupation level of the resulting fermionic level [67]. Using a pair of Majorana operators, annihilation and creation operators of fermions can be written as

$$a = \frac{1}{2}(\gamma_1 + i\gamma_2) \text{ and } a^\dagger = (\gamma_1 - i\gamma_2). \tag{1.34}$$

Now, for *s*-wave superconductivity, quasiparticles can be described by electron and hole components u and v with the operator

$$d = ua_\uparrow^\dagger + va_\downarrow. \tag{1.35}$$

The adjoint is

$$d^\dagger = v^*a_\downarrow^\dagger + u^*a_\uparrow, \tag{1.36}$$

in which case $d \neq d^\dagger$, even at zero energy where $u = v$ due to the opposite spins, hence the need for *p*-wave superconductivity [9]. As *p*-wave superconductivity is rarely found in nature, mainly in the superfluid phase of Helium-3 [90], this was one of the major obstructions towards experimental realization of Majorana zero modes. However, a breakthrough occurred in 2010 with the realization of effectively spinless phases of superconductivity by combining the proximity effect, Zeeman interaction and strong spin-orbit coupling in semiconductor nanowires [91–93].

Following that proposal, the field developed rapidly in both theory and experiment with various superconductor-semiconductor hybrid systems theorized, fabricated and investigated [94]. The most common nanowire systems consist of a solid

semiconducting nanowires in proximity to a parent superconductor, considered to realize the 1D Kitaev chain [95]. Core-shell nanowire systems are only beginning to be explored experimentally in the context of Majorana Zero Modes [96]. In a core-shell nanowire, the prismatic cross-section geometry becomes important due to the electron localization in the corner areas, which in the case of a thin shell, induces effectively 1D wires along each edge [4], see further Chap. 3. Ultimately, fusing and braiding Majorana zero modes is to implemented for quantum computation so having multiple Majorana Zero Modes capable of interacting in a single nanowire system is beneficial in that regard. In particular, a plane confinement is necessary for braiding and the nanowire end planes, in theory, provide such a plane.

In order to encode n number of qubits, $2n$ Majorana states are needed along with 2^n near degenerate states, necessary for the non-Abelian Berry phases to allow for quantum gates. Interchanging two Majorana zero modes, and Ising anyons in general, gives rise to more complex phase than in U(1) symmetry, namely a non-commutative unitary transformation introduced in the previous section,

$$\Psi \rightarrow \exp\left(i\frac{\pi}{4}\sigma_z\right)\Psi, \tag{1.37}$$

which corresponds to a braiding operation [14] of the total state $|\Psi\rangle$ of multiple Majoranas. However, this operation alone is not sufficient for universal quantum computation [67]. The phase gate, Eq. (1.6), is needed additionally, which would not be topological in essence. Other kinds of anyons, most notably the Fibonacci anyons [97], are capable of universal topological quantum computation, but they are even more difficult to realize experimentally. Formulations of hybrid approaches using Ising anyons show promise [98] and variations on the theme are ongoing [99].

Although fabrication of nanostructures has seen immense advancements in recent years, experimental realization of Majorana zero modes is in the beginning stages, with their manipulation being further in the future. At the time of writing, although there have been multiple observations in diverse systems of experimental indicators consistent with Majorana zero modes [100], mainly zero-bias conductance peaks, these indicators are not necessarily in one-to-one correspondence with the presence of Majorana zero modes as other phenomena, disorder and Andreev bound states, can induce matching conductance signatures [101]. In spite of recent setbacks in experimental realization of Majorana Zero Modes [102], the original proposal of using non-Abelian anyons for quantum computation [15] to tackle the decoherence problem in the scaling up of quantum computers, still stands. The topological approach will likely continue to play a major role in the development and bring about discoveries and investigations of related physical phenomena, inspired by the race for quantum supremacy.

Chapter 2

Theory of Superconductivity

Superconductivity was discovered in 1911 by Heike K. Onnes as a sudden disappearance of electrical resistance at a critical temperature [103]. Materials with this property are called superconductors. A current flowing in a superconductor is often referred to as a supercurrent. Ideally, provided that a low enough temperature is maintained, a supercurrent can persists indefinitely.

2.1 London equations

The basic equations relating the electric- and magnetic field to the superconducting current density are known as the London equations [104]

$$\boldsymbol{E} = \frac{\partial}{\partial t}\left(\Lambda \boldsymbol{J_s}\right), \tag{2.1a}$$

$$\boldsymbol{B} = -\boldsymbol{\nabla} \times \left(\Lambda \boldsymbol{J_s}\right). \tag{2.1b}$$

Note that here **B** denotes the microscopic flux density. The constant

$$\Lambda = \frac{m}{n_s e^2} \tag{2.2}$$

implies that the London equations describe forces acting on free electrons of mass m and charge e with the superconducting electron number density n_s [104]. These two equations can be combined into a single equation via the magnetic vector potential since

$$\boldsymbol{E} = -\frac{\partial \boldsymbol{A}}{\partial t}, \tag{2.3}$$

$$\boldsymbol{B} = \boldsymbol{\nabla} \times \boldsymbol{A} \tag{2.4}$$

and thus

$$\boldsymbol{A} = -\Lambda \boldsymbol{J_s}, \tag{2.5}$$

which means that the supercurrent is directly proportional to the magnetic vector potential. This relation can be motivated by the fact that the canonical momentum

$$\boldsymbol{p} = m\boldsymbol{v} + e\boldsymbol{A} \tag{2.6}$$

has a net zero expectation value in the ground state [105]. The average velocity then becomes

$$\langle v_s \rangle = -\frac{e\boldsymbol{A}}{m} \ . \tag{2.7}$$

Assuming uniform flow [106], the current will be

$$\boldsymbol{J_s} = \rho \langle v_s \rangle = n_s e \langle v_s \rangle \ , \tag{2.8}$$

and therefore,

$$\boldsymbol{J_s} = -\frac{\boldsymbol{A}}{\Lambda} \ . \tag{2.9}$$

Fritz London [107] noted that this description of superconductivity "is characterized not by an infinite value of the electrical conductivity, but rather by a new relation between the magnetic field and electric current."

Comparing Eq. (2.1a) with Ohm's law

$$\boldsymbol{J} = \sigma \boldsymbol{E} \ , \tag{2.10}$$

where σ is the conductance, we see that the difference lies in the time dependence. Using Eq. (2.3) we can write Ohm's law as

$$\boldsymbol{J} = -\sigma \frac{\partial \boldsymbol{A}}{\partial t} \ . \tag{2.11}$$

Considering the magnetic vector potential as momentum per charge, we see that in classical conductivity current flows when momentum changes in time whilst in superconductivity the charge momentum directly gives rise to the supercurrent.

2.2   Penetration depth and the Meissner effect

When an external magnetic field is applied to a superconductor, a supercurrent is induced in a layer with a thickness defined by the penetration depth. The supercurrent itself induces a magnetic field which expels the external magnetic field, so the magnetic field lines of the external field sway around the superconductor, Fig. 2.1.

Combining Eq. (2.1b) with the classical equation

$$\boldsymbol{\nabla} \times \mathbf{B} = \mu_0 \mathbf{J} \tag{2.12}$$

along with the relation

$$\boldsymbol{\nabla} \times (\boldsymbol{\nabla} \times \mathbf{B}) = -\nabla^2 \mathbf{B} \ , \tag{2.13}$$

one obtains

$$\nabla^2 \mathbf{B} = \frac{1}{\lambda_L^2} \mathbf{B}, \tag{2.14}$$

where

$$\lambda_L = \sqrt{\frac{m}{\mu_0 n_s e^2}} \tag{2.15}$$

is the London penetration depth. It describes the thickness of the layer in which the surface currents flow in the Meissner effect, Fig. 2.1.
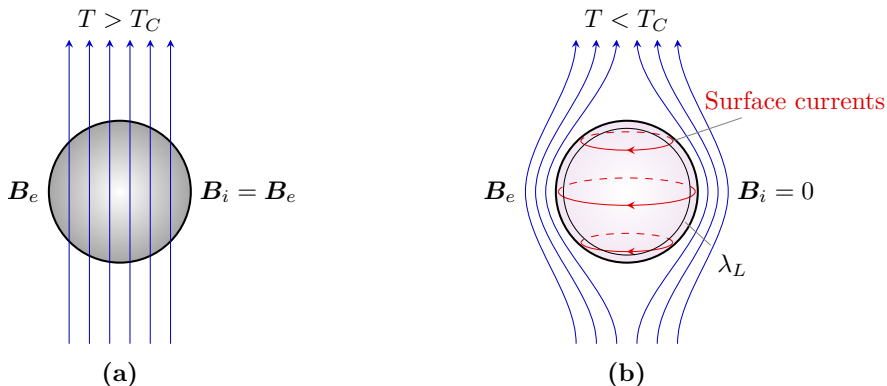
Figure 2.1: **(a)** An external magnetic field $\mathbf{B}_e$ applied to a sample at temperature T above the critical temperature T_C permeates the sample. **(b)** The Meissner effect: An external magnetic field applied to a superconductor is expelled by surface currents flowing in the outer layer of thickness λ_L.

A superconductor in an external magnetic field displays near perfect diamagnetism, apart from the penetration depth of the magnetic flux which can be likened to the classical skin depth of fields in normal conductors. It is worth noting that if the superconductor has a hole, such as a hollow cylinder, the surface currents of the outer and inner surface cancel and the magnetic field flows through unaltered [108].

The temperature dependence of the penetration depth has been empirically found to be [106]

$$\lambda_F(T) \cong \lambda_F(0) \frac{1}{\sqrt{1 - (T/T_C)^2}}, \tag{2.16}$$

where $\lambda_F(0)$ is the penetration depth at zero temperature. If the total density of conduction electrons, n, equals the superconducting electron number density n_s then

$$\lambda_F(0) = \sqrt{\frac{m}{\mu_0 n e^2}} \ . \tag{2.17}$$

Experiments have shown that the superconducting penetration depth of various samples is always larger than $\lambda_F(0)$, which leads to the definition of another key concept in the theory of superconductors: the coherence length [105].

2.3   Coherence length and the Ginzburg–Landau theory

In the literature on superconductors there are two concepts termed the coherence length [108], they differ in their temperature dependence. We begin by introducing the temperature independent coherence length due to Pippard [109].

Temperature independent Pippard coherence length/range

Equation (2.9) is valid in the case of uniform flow or slowly varying drift velocity of the electrons, when electron velocities have negligible variance over a specific distance, ξ_0 [106]. If that is not the case, a generalized model in needed. There is an accurate analogy with Ohm's law, Eq. (2.10), which brakes down when the classical penetration depth becomes similar in magnitude to the mean free path, ℓ, of electrons in the metal. Then, one has to take into account the mean value of the electric field around each point in a volume with radius ℓ. The generalized equation is

$$\mathbf{J}(\mathbf{r}) = \frac{3\sigma}{4\pi\ell} \int_V \frac{\mathbf{R}[\mathbf{R} \cdot \mathbf{E}(\mathbf{r}')]}{\mathbf{R}^4} e^{-R/\ell} \, d\mathbf{r}', \tag{2.18}$$

where $\mathbf{R} = \mathbf{r} - \mathbf{r}'$ and the integral is over the total volume of the metal. In the same manner the London equation (2.9) can be generalized with

$$\mathbf{J}(\mathbf{r}) = \frac{3}{4\pi\xi_0\Lambda} \int_V \frac{\mathbf{R}[\mathbf{R} \cdot \mathbf{A}(\mathbf{r}')]}{\mathbf{R}^4} e^{-R/\xi} \, d\mathbf{r}', \tag{2.19}$$

where ξ is the general coherence length for impure metals or alloys, given in terms of the coherence length of a pure metal ξ_0 and the mean free path ℓ [106],

$$\frac{1}{\xi} = \frac{1}{\xi_0} + \frac{1}{\ell}. \tag{2.20}$$

If the magnetic vector potential $\mathbf{A}(\mathbf{r})$ is constant in a volume of radius ξ_0 we obtain the London equation (2.9) from Eq. (2.19).

There exists the following argument for the coherence length based on the uncertainty principle. The superconducting phenomena comes into play at the critical temperature T_C and the electrons have momentum of the order $\Delta p \approx k_B T_C / v_F$ where k_B is the Boltzmann constant and v_F is the Fermi velocity. Then according to

the uncertainty principle

$$\Delta x \geq \frac{\hbar}{2\Delta p} = a\frac{\hbar v_F}{k_B T_C} =: \xi_0, \tag{2.21}$$

with a being a material constant [105]. As a final note on the conceptual meaning of the coherence length, it can be shown that the wavefunction of a single Cooper pair, which will be discussed in Sec. 2.8, has a spatial extent of the same order of magnitude as ξ_0 [108]. The theories of London and Pippard contain neither wavefunctions nor Cooper pairs and are both based purely on electrodynamical phenomenology.

Temperature dependent Ginzburg-Landau coherence length

Before a microscopic theory of superconductivity was formulated, Ginzburg and Landau put forth a theory based mostly on intuition [108]. The need for a more general model than that of the London equations was evident due to their prediction of a negative surface energy at the interface between the superconducting and normal state, in contradiction to the observed positive surface energy [110]. They introduced an effective wavefunction describing superconducting electrons locally with

$$\left|\psi(\mathbf{r})\right|^2 = n_s(\mathbf{r}), \tag{2.22}$$

where n_s is the superconducting electron number density. Ginzburg-Landau (GL) theory is semi-classical and was a precursor of the quantum mechanical BCS theory. For future reference we note that there is a formal analogy with the BCS pairing potential to this effective wavefunction (2.22) and that they are in fact directly proportional [106].

The equations governing the behavior of the wavefunction are obtained by defining the free energy of the superconductor in a magnetic field and minimizing it with respect to the magnetic vector potential [105]. For a superconductor with constant electron density and no external field, the free energy can be expanded as

$$E = \alpha\left|\psi\right|^2 + \frac{\beta}{2}\left|\psi\right|^4, \tag{2.23}$$

where $\alpha(T) \propto (T - T_C)$ and $\beta(T_C)$ are coefficients of the expansion and functions of the temperature and critical temperature respectively [111]. If ψ is assumed to be slowly varying near the critical temperature T_C, another term has to be added to the free energy [110]

$$E = \alpha\left|\psi\right|^2 + \frac{\beta}{2}\left|\psi\right|^4 - \frac{\hbar^2}{2m^*}\left|\boldsymbol{\nabla}\psi\right|^2, \tag{2.24}$$

where m^* refers to an unknown phenomenological mass. In order to have the last term invariant with respect to the gauge of the vector potential, the gradient is made

covariant with

$$E = \alpha|\psi|^2 + \frac{\beta}{2}|\psi|^4 - \frac{1}{2m^*}|(-i\hbar\nabla - e^*\mathbf{A})\psi|^2 \qquad (2.25)$$

where e^* is the phenomenological charge, which later turned out to be the charge of an electron pair $e^* = 2e$. Finally, an external magnetic field $\mathbf{B} = \nabla \times \mathbf{A}$ is added, leading to the GL free energy [111],

$$E = \alpha|\psi|^2 + \frac{\beta}{2}|\psi|^4 - \frac{1}{2m^*}|(-i\hbar\nabla - e^*\mathbf{A})\psi|^2 + \frac{1}{2\mu_0}|\nabla \times \mathbf{A}|^2 \, . \qquad (2.26)$$

Minimizing this free energy with respect to the magnetic vector potential $\mathbf{A}$ and assuming the Coulomb gauge, one obtains the following set of equations,

$$\frac{1}{2m^*}(i\hbar\nabla + e^*\mathbf{A})^2\psi = \left(\alpha + \beta|\psi|^2\right)\psi \, , \qquad (2.27)$$

$$\mathbf{J}_s = \frac{-i\hbar e^*}{2m^*}\left(\psi^\dagger\nabla\psi - \psi\nabla\psi^\dagger\right) - \frac{e^{*2}}{m^*}|\psi|^2\mathbf{A} \, . \qquad (2.28)$$

These are known as the Ginzburg-Landau (GL) equations [112]. By considering a trivial case of the first equation in one dimension in terms of reduced variables, one gets the temperature dependent GL coherence length [106]

$$\xi_{GL}(T) = \hbar\,|2m^*\alpha(T)|^{-\frac{1}{2}}, \qquad (2.29)$$

describing the space in which ψ varies slowly with negligible energy increase. In the case of a pure superconductor well below the critical temperature, the GL coherence length and the temperature independent Pippard coherence length are equal [105].

By considering the second GL equation (2.28) with the approximation that the value of ψ in weak fields is the same as the constant equilibrium value, ψ_0, in the absence of an external field, one obtains a London type equation

$$\mathbf{J}_s = -\frac{e^{*2}}{m^*}|\psi_0|^2\mathbf{A} \, . \qquad (2.30)$$

We should then be able to derive a penetration depth as in Sec. 2.2. For the sake of diversity, let us derive it in terms of the magnetic vector potential with the classical correspondence to the current,

$$\nabla^2\mathbf{A} = -\mu_0\mathbf{J} \, . \qquad (2.31)$$

Then

$$\nabla^2\mathbf{A} = \frac{\mu_0 e^{*2}|\psi_0|^2}{m^*}\,\mathbf{A} = \frac{1}{\lambda_{GL}^2}\,\mathbf{A} \qquad (2.32)$$

and so

$$\lambda_{GL} = \sqrt{\frac{m^*}{\mu_0 e^{*2}|\psi|^2}}, \qquad (2.33)$$

which has the same form as Eq. (2.15) given the condition of Eq. (2.22). The magnetic field therefore penetrates the superconductor up to the penetration depth λ_L. The induced surface currents follow the magnetic vector potential field lines, Fig. 2.1.

The temperature dependence of the GL penetration depth λ_{GL} near T_C is found to be the same as that of the GL coherence length ξ_{GL} [106] and thus a dimensionless temperature independent parameter can be defined as,

$$\kappa = \frac{\lambda_{GL}}{\xi_{GL}} . \qquad (2.34)$$

This parameter is known simply as the *GL parameter* and its value for a pure standard superconductor is much less than unity which implies $\lambda_{GL} << \xi_{GL}$. Solving the GL equations with the proper boundary conditions, a positive surface energy for the junction of a normal and superconducting material is obtained, in alignment with experiments [105]. Abrikosov [113] considered the case when $\lambda_{GL} > \xi_{GL}$ when discussing surprising experimental results of Zavaritskii and found that at the exact value $\kappa = 2^{-1/2}$, the surface energy between a superconducting and a normal layer becomes zero and above that value it becomes negative. Superconductors with $\kappa > 2^{-1/2}$ were first called superconductors of the second group but are today known as type-II superconductors. Conversely, for type-I superconductors, $\kappa < 2^{-1/2}$.

2.4 Insulator-Superconductor junctions

Consider the junction of an insulator and a type-I superconductor. By solving Eq. (2.14) in one dimension, the magnetic field is found to be exponentially dampened in the superconductor

$$\mathbf{B}(x) = \mathbf{B_e} \exp\left(-\frac{x}{\lambda}\right), \qquad (2.35)$$

which is plotted in Fig. 2.2 where λ is the penetration depth from Eq. (2.33). To estimate the superconducting state density, Eq. (2.27) can be solved in one dimension with the assumption that no current passes the boundary to obtain [106]

$$\frac{\psi(x)}{\psi_0} = \tanh\left(\frac{x}{\sqrt{2}\,\xi_{GL}}\right) , \qquad (2.36)$$

where ψ_0 describes the superconducting state in the absence of magnetic fields and currents. Since $\lambda_{GL} < \xi_{GL}$, Fig. 2.2 applies to type-I superconductors.
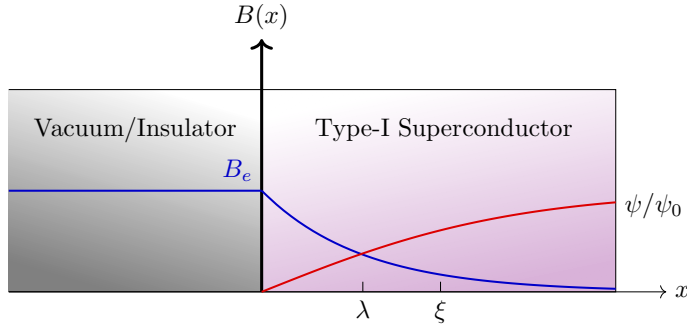
Figure 2.2: The magnetic flux density B along with the superconducting pair density wavefunction ψ of a type-I superconductor where the coherence length ξ is larger than then penetration depth λ.

2.5   Type I vs. type II superconductors

When applying magnetic fields to matter, one has to take into account the magnetization in the material itself, **M**, from the collective atomic magnetic momenta [114,115]. The measured average local magnetic field **B** is influenced by the magnetization such that the magnetic field strength becomes

$$\mathbf{H} = \frac{1}{\mu_0}\mathbf{B} - \mathbf{M} \, , \tag{2.37}$$

where **H** is the the magnetic field strength corresponding to the free current density. This distinction can be made in superconductors, but a thermodynamic approach is needed to incorporate the phase change from the superconducting state to the normal state, that occurs at the thermodynamic critical magnetic field strength H_C [116]. The temperature dependence of the critical magnetic field strength H_C for type-I superconductors, Fig. 2.3, has been empirically found to be [108]

$$H_C(T) = H_0 \left[1 - \left(\frac{T}{T_C} \right)^2 \right] \, . \tag{2.38}$$

In type-II superconductors there exists an intermediate state between the normal phase and the type-I superconducting phase [106]. With increasing external magnetic field strength, the magnetic field starts to penetrate the bulk of the superconductor in an effect known as flux pinning [117] or quantum locking, Fig. 2.4. This type-II superconducting phase transition is said to occur at the lower critical magnetic field strength

$$H_{C_1}(T) \approx \frac{\ln(\kappa)}{\sqrt{2}\kappa} H_C(T) \, . \tag{2.39}$$
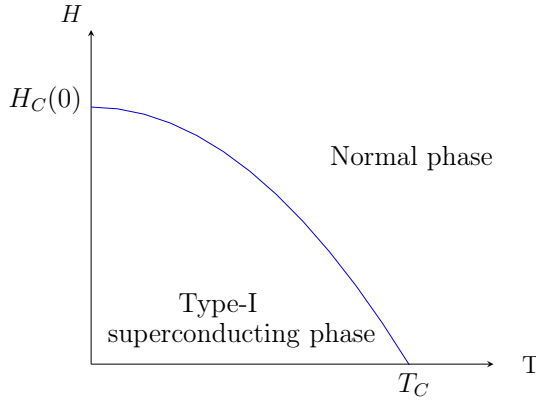
Figure 2.3: Temperature dependence of the type-I critical magnetic field H_c.

The penetrating magnetic field lines induce vortices in the bulk of material, Fig. 2.5, which have the curious effect of locking the material in place with the magnetic field lines, allowing for stable magnetic levitation [118].
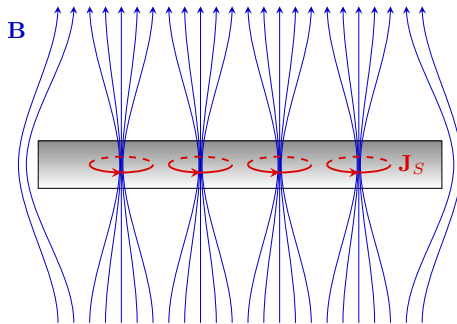
Figure 2.4: Flux pinning of a type-II superconductor in the intermediate state. The external magnetic field **B** penetrates the bulk, forming currents J_S.

Further increasing the external magnetic field strength, the intermediate flux pinning state is lost at the upper critical field,

$$H_{C_2}(T) = \sqrt{2}\kappa\, H_C(T)\,. \tag{2.40}$$

The relation for H_{C_2} in Eq. (2.40) is only valid for an infinite medium [105]. In reality the superconducting phase is never completely lost at H_{C_2}. A superconducting sheath [106] persists up to the third critical magnetic field strength with an exact relation

$$H_{C_3} = 1.695\, H_{C_2}\,. \tag{2.41}$$
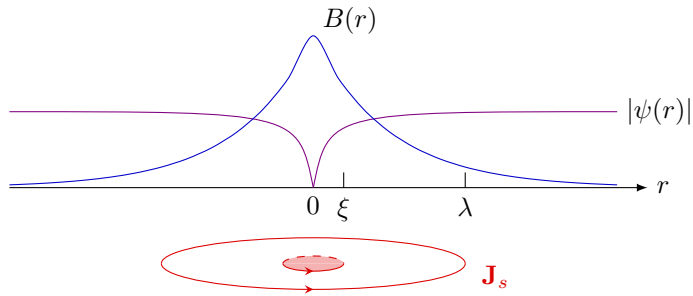
Figure 2.5: Sketch of the structure of a vortex in a type-II superconductor. The vortex core size is on the scale of ξ with the corresponding currents decaying with λ. The microscopic magnetic flux density $B(r)$ has its maximum value in the center of the vortex where the density of the superconducting states becomes zero [105].

Superconducting sheath effects can be suppressed with a normal metal coating [119]. The multiple critical magnetic field dependencies for a type-II superconductors are plotted in Fig. 2.6.
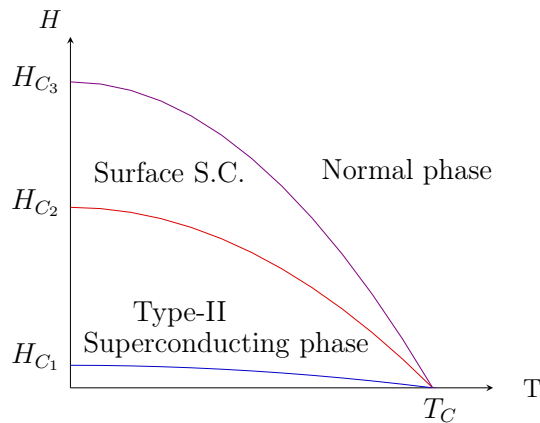
Figure 2.6: Temperature dependence of the type-II critical magnetic field strength.

2.6 Flux quantization

Rewriting the GL supercurrent expression in (2.28) with $\psi = |\psi|e^{i\theta}$ and integrating around a closed contour C within a superconductor gives [120]

$$\oint_C \mathbf{A} \cdot d\boldsymbol{\ell} + \frac{m^*}{e^{*2}} \oint_C |\psi|^{-2} \mathbf{J_S} \cdot d\boldsymbol{\ell} = \frac{\hbar}{e^*} \oint_C \boldsymbol{\nabla}\theta \cdot d\boldsymbol{\ell} . \tag{2.42}$$

The left hand side is F. Londons *fluxoid*, Φ_0, found to be a constant for magnetic fluxes through superconductors with holes, like superconducting rings and cylinders [107]. Assuming the wavefunction ψ is single valued, the right hand side integral must be an integer multiple n of 2π to ensure the same values of ψ after a phase cycle, therefore the fluxoid is quantized,

$$\Phi_0 = \frac{\hbar}{e^*} 2\pi n, \text{ where } n \in \mathbb{N}. \tag{2.43}$$

As discussed in Sec. 2.8, the charge e^* describes a pair of electrons, giving the value of the superconducting flux quantum as

$$\Phi_0^{SC} = \frac{2\pi\hbar}{2e} = \frac{h}{2e} \approx 2 \cdot 10^{-15} \text{ T} \cdot \text{m}^2 . \tag{2.44}$$

Alternatively, Eq. (2.42) can be seen as an expression of the canonical momentum

$$\mathbf{p} = m\mathbf{v} + q\mathbf{A}. \tag{2.45}$$

Along with the expression for the supercurrent velocity, Eq. (2.9), we can see that Eq. (2.42) essentially describes the canonical momentum, with

$$\mathbf{p} = e^*\mathbf{A} + m\mathbf{v_s} = \hbar\boldsymbol{\nabla}\theta, \tag{2.46}$$

where θ is the phase of the wavefunction like before. As Feynman noted in Ref. [121], the quantity $\hbar\boldsymbol{\nabla}\theta$ is the canonical momentum itself. The wavefunction phase can be written in terms of the gauge function χ as they are related by

$$\theta = \frac{e^*}{\hbar}\chi. \tag{2.47}$$

Rewriting Eq.(2.42) with the canonical momentum gives

$$\oint \mathbf{p} \cdot d\boldsymbol{\ell} = n \cdot \Phi_0 , \tag{2.48}$$

which is analogous to the Bohr-Sommerfeld quantum condition, formulated to describe the quantization of angular momentum of an atom [105].

2.7 Josephson junctions

An interesting phenomenon occurs when two superconductors are coupled by a thin insulating barrier, Fig. 2.7. If the phases of the wavefunctions on either side differ, a current flows without any applied voltage [122]. The effect can be understood as a kind of tunneling but an intuitive argument for the effect is as follows. A difference in the phases results in a gradient of the phase function through the junction, which is equal to a magnetic vector potential (charge momentum) from (2.46). Therefore, according to (2.9), a current will flow. The expression for the supercurrent in a Joseph-
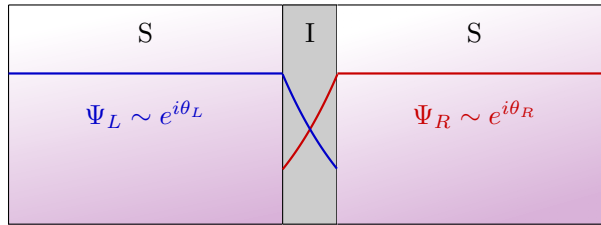
Figure 2.7: Superconductor-Insulator-Superconductor junction, known as a Josephson junction. Current can flow through the insulating barrier in the absence of an applied voltage, due to a phase difference between the superconductors.

son junction, the Josephson current, is given by the sine of the phase difference of wavefunctions in the junction

$$J = J_0 \sin(\Delta\theta), \tag{2.49}$$

where J_0 is the maximum current, which can be calculated from geometric properties of the junction [123]. Recent fabrications of Josephson junctions have been made more complex, for example using a semiconducting barriers, quantum dots and ferromagnetic materials [124]. Junctions with topological insulators have been proposed as Majorana platforms [125]. Majorana zero modes are also expected to emerge for junctions with topological superconductivity. However, they also host Andreev bound states, considered to be formed by multiple Andreev reflections (see Sec. 2.10) that have similar experimental signatures [126].

A superconducting quantum interference device (SQUID), Fig. 2.8, can be made by connecting two junctions in parallel [127]. When an external magnetic field is applied perpendicular to the plane of the structure, the current in the upper branch flows against the magnetic vector potential whilst the current in the lower branch flows along with it, inducing a phase difference between the two branches, analogous to the Aharanov-Bohm effect. The phase difference leads to oscillations of the current with the external magnetic field strength. The maximum amplitude of the current occurs for integer numbers of the flux quantum, Eq. (2.44) [121].
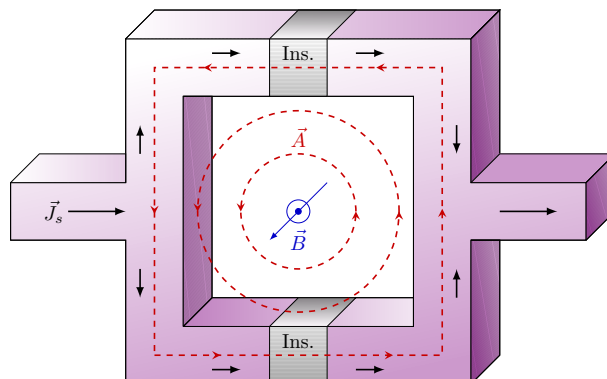
Figure 2.8: A superconducting quantum interference device (SQUID) consists of two parallel Josephson junctions. The whole structure is made of a superconducting material, apart from two thin insulating barriers in the upper and lower branch. The supercurrent $\vec{J}_s$ splits into the upper and lower branch. A magnetic field $(\vec{B})$ is applied perpendicular to the plane, out of the page, resulting in the magnetic vector potential $(\vec{A})$, shown in red.

2.8 Microscopic Theory

Both the London and Ginzburg-Landau models of superconductivity describe the collective behaviour of the superconducting elements, without any fundamental description of the superconducting state itself. After their development, experiments revealed that there is no change in the crystal lattice structure of a material when it enters the superconducting phase [108], however different isotopes of elements result in different critical temperatures [128], implying that the lattice affects the conduction of electrons in the superconducting state.

Phonons are quanta of lattice vibrations. The microscopic interaction between superconducting states is microscopically attributed to phonon emission-absorption events between a pair of electrons, having momentum of the same magnitude but opposite orientation, Fig. 2.9. Such a pair is called a Cooper pair [129]. Pair formation of fermions with this kind of momentum configuration, into composite bosons, is energetically favourable due to the slightly positive lattice interaction V. The effect only becomes dominant below T_C. As noted in Sec. 1.4, other pairing interactions occur in non-conventional superconductors.
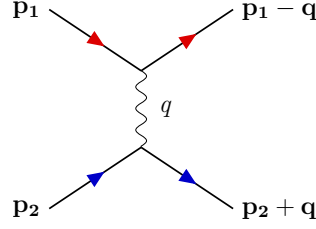
Figure 2.9: A particle with momentum $\mathbf{p_1}$ emits a phonon of momentum q which is absorbed by another particle of momentum $\mathbf{p_2}$ [106].

2.8.1 Second quantization technique

In order to describe the quantum mechanics of many-particle systems it is convenient to use the complete orthogonal basis of state vectors

$$|n_1 \, n_2 \dots n_\infty\rangle, \tag{2.50}$$

along with the creation operators for bosons and fermions, $b_k^\dagger$ and $f_k^\dagger$ respectively and the corresponding annihilation operators b_k and f_k. The operators satisfy the following relations

$$[b_i, b_j^\dagger] = b_i b_j^\dagger - b_j^\dagger b_i = \delta_{ij},$$
$$[b_i, b_j] = [b_i^\dagger, b_j^\dagger] = 0. \tag{2.51}$$

$$\{f_i, f_j^\dagger\} = f_i f_j^\dagger + f_j^\dagger f_i = \delta_{ij},$$
$$\{f_i, f_j\} = \{f_i^\dagger, f_j^\dagger\} = 0. \tag{2.52}$$

With this formulation, a many-particle wavefunction can be written as a general state vector, with F denoting the set of expansion coefficients corresponding to the set of quantum numbers [120],

$$|\Psi(t)\rangle = \sum_{n_\infty} F(n_1 \, n_2 \dots n_\infty, t) \, |n_1 \, n_2 \dots n_\infty\rangle \, . \tag{2.53}$$

Schrödinger's equation is valid for $|\Psi(t)\rangle$,

$$i\hbar \frac{\partial}{\partial t} |\Psi(t)\rangle = \hat{H} |\Psi(t)\rangle, \tag{2.54}$$

where the hamiltonian $\hat{H}$ can be written in terms of the creation and annihilation operators. For bosons we have

$$\hat{H} = \sum_{ij} b_i^\dagger \langle i| \, K \, |j\rangle b_j + \frac{1}{2} \sum_{ijlm} b_i^\dagger b_j^\dagger \langle ij| \, V \, |lm\rangle b_l b_m \tag{2.55}$$

with K and V denoting the kinetic- and potential energy respectively. In a similar manner for fermions we have

$$\hat{H} = \sum_{ij} f_i^\dagger \langle i| K |j\rangle f_j + \frac{1}{2} \sum_{ijlm} f_i^\dagger f_j^\dagger \langle ij| V |lm\rangle f_m f_l \tag{2.56}$$

with the subtle difference of ordering of the last annihilation operators being specific to fermions, due to their non-commutativity. With linear combinations of the creation and annihilation operators, either bosonic or fermionic denoted $c^\dagger$ and c respectively, field operators $\hat{\psi}$ can be formed, where the single-particle states ψ_k become the coefficients of expansion,

$$\begin{aligned}
\hat{\psi}^\dagger(\mathbf{r}) &= \sum_k \psi_k^\dagger(\mathbf{r}) \, c_k^\dagger, \\
\hat{\psi}(\mathbf{r}) &= \sum_k \psi_k(\mathbf{r}) \, c_k \, .
\end{aligned} \tag{2.57}$$

Then both Hamiltonians, (2.55) and (2.56), can be written as [120]

$$\hat{H} = \int d\mathbf{r} \, \hat{\psi}^\dagger(\mathbf{r}) K(\mathbf{r}) \hat{\psi}(\mathbf{r}) + \frac{1}{2} \iint d\mathbf{r} \, d\mathbf{r}' \, \hat{\psi}^\dagger(\mathbf{r}) \hat{\psi}^\dagger(\mathbf{r}') V(\mathbf{r}, \mathbf{r}') \hat{\psi}(\mathbf{r}') \hat{\psi}(\mathbf{r}) \, . \tag{2.58}$$

2.8.2 BCS theory

Bardeen-Cooper-Schrieffer (BCS) put forth a microscopic theory of superconductivity based on Cooper pairs in the language of second quantization [130]. Later, Gorkov showed that GL-theory can be derived from the BCS theory [131]. Each Cooper pair has opposite spin and momentum and can be given in terms of the wavevector pair $(\mathbf{k}_\uparrow, -\mathbf{k}_\downarrow)$. The ground state of multiple Cooper pairs can be described by the product

$$|\psi_G\rangle = \prod_{\mathbf{k}_1, \dots, \mathbf{k}_m} (u_{\mathbf{k}} + v_{\mathbf{k}} \, c_{\mathbf{k}_\uparrow}^\dagger c_{-\mathbf{k}_\downarrow}^\dagger) |0\rangle \tag{2.59}$$

where $|0\rangle$ is the vacuum while $|u_k|^2$ and $|v_k|^2$ are the pair occupation probabilities. The coefficient $|v_k|^2$ is the occupational probability of the pair $(\mathbf{k}_\uparrow, -\mathbf{k}_\downarrow)$ and $|u_k|^2$ the probability that the state is unoccupied [105]. To have the same number of occupied and unoccupied states, the Hamiltonian is shifted so that the kinetic energy is zero at the chemical potential, $H_{BCS} = H_0 - \mu N$ where N is the average number of particles. The pairing Hamiltonian is then

$$H_{BCS} = \sum_{\mathbf{k}} \varepsilon_{\mathbf{k}} c_{\mathbf{k}\uparrow}^\dagger c_{\mathbf{k}\uparrow} + \varepsilon_{\mathbf{k}} c_{\mathbf{k}\downarrow}^\dagger c_{\mathbf{k}\downarrow} + \sum_{\mathbf{k}, \mathbf{k}'} V_{\mathbf{k}, \mathbf{k}'} c_{\mathbf{k}\uparrow}^\dagger c_{-\mathbf{k}\downarrow}^\dagger c_{-\mathbf{k}'\downarrow} c_{\mathbf{k}'\uparrow}, \tag{2.60}$$

where the single particle energy with respect to the Fermi energy is

$$\varepsilon_{\mathbf{k}} = \frac{\hbar^2 \mathbf{k}^2}{2m} - \mu. \tag{2.61}$$

One can find the coefficients u_k and v_k using the variational approach, minimizing

$$\delta \langle \psi_G | H_{BCS} | \psi_G \rangle = 0 \tag{2.62}$$

using the condition that $|u_k|^2 + |v_k|^2 = 1$. The energy gap or pairing potential is defined as

$$\Delta_{\mathbf{k}} = - \sum_{\mathbf{k},\mathbf{k}'} V_{\mathbf{k},\mathbf{k}'} u_{\mathbf{k}'} v_{\mathbf{k}'}, \tag{2.63}$$

where $V_{\mathbf{k},\mathbf{k}'}$ is the interaction potential of Cooper pairs. It is generally assumed to be independent of $\mathbf{k}$ and approximated with a constant value, $V_{\mathbf{k},\mathbf{k}'} \sim -V$. Then the dispersion relation for superconductors is given by

$$E_{\mathbf{k}} = \sqrt{\Delta_{\mathbf{k}}^2 + \varepsilon_{\mathbf{k}}^2}, \tag{2.64}$$

where $\Delta_{\mathbf{k}}$ is the minimum excitation energy.

2.9   Bogoliubov-de Gennes formalism

Instead of the variational approach in Eq. (2.62), a generalization of the Hartree-Fock method can be applied to superconductivity [106]. If the pairing potential is written as

$$\Delta_{\mathbf{k}} = - \sum_{\mathbf{k},\mathbf{k}'} V_{\mathbf{k},\mathbf{k}'} \langle c_{-\mathbf{k}'\downarrow} c_{\mathbf{k}'\uparrow} \rangle, \tag{2.65}$$

the Hamiltonian (2.60) can be written as

$$H = \sum_{\mathbf{k},\sigma} \varepsilon_{\mathbf{k}} c_{\mathbf{k}\sigma}^{\dagger} c_{\mathbf{k}\sigma} - \sum_{\mathbf{k}} (\Delta_{\mathbf{k}} c_{\mathbf{k}\uparrow}^{\dagger} c_{-\mathbf{k}\downarrow}^{\dagger} + \Delta_{\mathbf{k}}^{*} c_{-\mathbf{k}\downarrow} c_{\mathbf{k}\uparrow}), \tag{2.66}$$

and expressed in the matrix form

$$H = \sum_{\mathbf{k}} \begin{bmatrix} c_{\mathbf{k}\uparrow}^{\dagger} & c_{-\mathbf{k}\downarrow} \end{bmatrix} \begin{bmatrix} \varepsilon_{\mathbf{k}} & \Delta_{\mathbf{k}} \\ -\Delta_{\mathbf{k}}^{*} & -\varepsilon_{\mathbf{k}} \end{bmatrix} \begin{bmatrix} c_{\mathbf{k}\uparrow} \\ c_{-\mathbf{k}\downarrow}^{\dagger} \end{bmatrix}. \tag{2.67}$$

The diagonalization method of the Hamiltonian is based on the Bogoliubov-Valatin transformation [123]

$$\begin{pmatrix} \gamma_{\mathbf{k}\uparrow} \\ \gamma_{-\mathbf{k}\downarrow}^{\dagger} \end{pmatrix} = \begin{pmatrix} u_{\mathbf{k}}^{*} & v_{\mathbf{k}} \\ -v_{\mathbf{k}}^{*} & u_{\mathbf{k}} \end{pmatrix} \begin{pmatrix} c_{\mathbf{k}\uparrow} \\ c_{-\mathbf{k}\downarrow}^{\dagger} \end{pmatrix}, \tag{2.68}$$

allowing the substitution of the operators $c_{\mathbf{k}}$ by fermionic *quasiparticle* operators $\gamma_{\mathbf{k}}$ which gives the Hamiltonian the simplified form

$$H = E_g + \sum_{\mathbf{k}} E_{\mathbf{k}} (\gamma_{\mathbf{k}\uparrow}^{\dagger} \gamma_{\mathbf{k}\uparrow} + \gamma_{\mathbf{k}\downarrow}^{\dagger} \gamma_{\mathbf{k}\downarrow}), \tag{2.69}$$

where

$$|v_{\mathbf{k}}|^2 = 1 - |u_{\mathbf{k}}|^2 = \frac{1}{2}\left(1 - \frac{\varepsilon_{\mathbf{k}}}{E_{\mathbf{k}}}\right). \tag{2.70}$$

By calculating and comparing the commutation relations of the Hamiltonian with the operators $c_{\mathbf{k}}$ and $\gamma_{\mathbf{k}}$ one arrives at [106]

$$\begin{aligned} E_{\mathbf{k}} u_{\mathbf{k}} &= H u_{\mathbf{k}} + \Delta_{\mathbf{k}} v_{\mathbf{k}}\,, \\ E_{\mathbf{k}} v_{\mathbf{k}} &= -H^* v_{\mathbf{k}} + \Delta_{\mathbf{k}}^* u_{\mathbf{k}}\,, \end{aligned} \tag{2.71}$$

which can be written as

$$\begin{pmatrix} H & \Delta_{\mathbf{k}} \\ -\Delta_{\mathbf{k}}^* & -H^* \end{pmatrix}\begin{pmatrix} u_{\mathbf{k}} \\ v_{\mathbf{k}} \end{pmatrix} = E\begin{pmatrix} u_{\mathbf{k}} \\ v_{\mathbf{k}} \end{pmatrix}. \tag{2.72}$$

The Bogoliubov-de Gennes (BdG) Hamiltonian has the form

$$H_{BdG} = \begin{pmatrix} H & \Delta_{\mathbf{k}} \\ -\Delta_{\mathbf{k}}^* & -H^* \end{pmatrix}. \tag{2.73}$$

The corresponding BdG wave function is

$$\psi_{BdG}(\mathbf{r}) = \begin{pmatrix} u_{\mathbf{k}} \\ v_{\mathbf{k}} \end{pmatrix} e^{i\mathbf{k}\mathbf{r}} = \begin{bmatrix} u_{\mathbf{k}}(\mathbf{r}) \\ v_{\mathbf{k}}(\mathbf{r}) \end{bmatrix} \tag{2.74}$$

where the spatial dependence is expanded in terms of plane waves [131]. From Eq. (2.71) the energy-momentum relation can be found, using $\hbar^2\mathbf{\nabla}^2 = \hat{\mathbf{p}}^2 = \hbar^2\mathbf{k}^2$, one obtains

$$E_k^2 = \left[\frac{\hbar^2 k^2}{2m} - \mu\right]^2 + \Delta^2 = \varepsilon_k^2 + \Delta^2, \tag{2.75}$$

and thus

$$\frac{\hbar^2 k_{\pm}^2}{2m} = \mu \pm \sqrt{E^2 - \Delta^2}\,. \tag{2.76}$$

From Eq. (2.70) the energy relation for the BCS electron and hole probability coefficients respectively can be derived,

$$\begin{aligned} u_k^2 &= \frac{1}{2} + \frac{1}{2E}\left(\frac{\hbar^2 k^2}{2m} - \mu\right), \\ v_k^2 &= \frac{1}{2} - \frac{1}{2E}\left(\frac{\hbar^2 k^2}{2m} - \mu\right). \end{aligned} \tag{2.77}$$

For $|E| > \Delta$,

$$u_{k+}{}^2 = \frac{1}{2} + \frac{1}{2E}\left(\sqrt{E^2 - \Delta^2}\right) > \frac{1}{2}$$
$$\rightarrow \text{electron-dominant,} \qquad (2.78)$$
$$v_{k+}{}^2 = \frac{1}{2} - \frac{1}{2E}\left(\sqrt{E^2 - \Delta^2}\right) < \frac{1}{2}$$

whilst

$$u_{k-}{}^2 = \frac{1}{2} - \frac{1}{2E}\left(\sqrt{E^2 - \Delta^2}\right) < \frac{1}{2}$$
$$\rightarrow \text{hole-dominant.} \qquad (2.79)$$
$$v_{k-}{}^2 = \frac{1}{2} + \frac{1}{2E}\left(\sqrt{E^2 - \Delta^2}\right) > \frac{1}{2}$$

From the quasiparticle character of the excitations according to Eq. (2.68), one can deduce that the positive solution in (2.76) gives an electron dominant excitation whereas the negative one is hole dominant [132]. For clarity we will write k_e for k_+ and k_h for k_-. Since $\pm k$ is a solution for both k_e and k_h, the energy-momentum relation yields a fourfold degeneracy of states for each energy above Δ as depicted in Fig. 2.10. In the presence of an applied external magnetic field, an additional twofold spin degeneracy has to be considered.
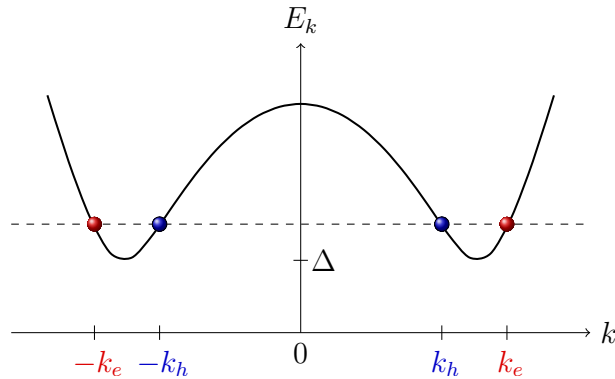
Figure 2.10: Degeneracy and type of the wave vector **k** for each energy value above Δ in a homogeneous superconductor.

2.10 Andreev reflection and the proximity effect

When a superconductor is brought in contact with a metal or semiconductor, superconductivity is induced in the latter one. This is the superconducting proximity effect, also known as the Holm-Meissner effect [133]. The effect has emerged as a key element in modern nanoscale technologies, in particular as a way to synthetically engineer topological superconductors capable of hosting Majora zero modes [9]. The mechanism of the effect is commonly understood in terms of Andreev-reflection [134], where Cooper pairs form in a superconductor when electrons incident from the normal conductor meet the boundary. Conversely, Cooper pairs are said to leak into the metal from the superconductor [105]. The latter process has been criticized as being only vaguely clarified [135] and despite having been known for close to a century now, there is no generalized model of the effect but multiple theoretical models exists for various special cases of the proximity effect [136].

2.10.1 The BTK model

Blonder-Tinkham & Klapwijk (BTK) [132] analyzed Andreev reflection by solving the Bogoliubov-de Gennes equations (2.71), for a normal metal-superconductor junction, Fig. 2.11. Assuming constant values of the chemical potential μ and the superconducting gap parameter Δ for an incident electron from the metal side, the solutions of the incoming and reflected waves are

$$\psi_{inc} = \begin{bmatrix} 1 \\ 0 \end{bmatrix} e^{ik_e x} \tag{2.80}$$

and

$$\psi_{refl} = a \begin{bmatrix} 0 \\ 1 \end{bmatrix} e^{ik_h x} + b \begin{bmatrix} 1 \\ 0 \end{bmatrix} e^{-ik_e x} , \tag{2.81}$$

for the composite wavefunctions

$$\psi_{\pm k_{e/h}} = \begin{bmatrix} u_0 \\ v_0 \end{bmatrix} e^{\pm ik_{e/h} x} , \tag{2.82}$$

where u_0 and v_0 are the probabilities for an electron and hole, respectively. The coefficients of reflection for the hole and electron, a and b, are obtained by applying the boundary conditions of continuity at the interface, $\psi_S(0) = \psi_N(0)$, along with the derivative boundary condition $(\hbar/2m)(\psi_S'(0) - \psi_N'(0)) = h\psi(0)$. This results in [132],

$$a = \frac{u_0 v_0}{u_0^2 + (u_0^2 - v_0^2)Z^2} \quad \text{and} \quad b = \frac{(u_0^2 - v_0^2)(Z^2 + iZ)}{(u_0^2 - v_0^2)Z^2} , \tag{2.83}$$

where $Z = h/\hbar v_F$ is a dimensionless parameter describing the magnitude of a delta potential $V(x) = h\delta(x)$ at the interface of the normal metal and superconductor. For the simplest case, let $Z = 0$. Then $a = v_0/u_0$ and $b = 0$, meaning that an incident electron (2.80) is purely reflected as a hole (2.81), in a process known as Andreev reflection [137]. An additional electron is absorbed by the superconductor, which causes the reflected hole. If an electron is incident on the boundary at an angle, the reflected hole path is parallel to the incident path, which is termed retro-reflection. Only in the case that the electron is incident orthogonal to the boundary, Fig. 2.11, do reflection and retro-reflection coincide.
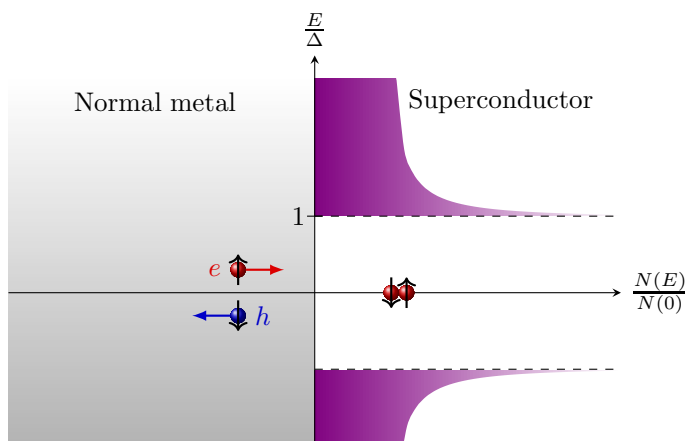
Figure 2.11: A normal metal-superconductor junction, showing the density of states in the superconductor. An electron incident at the boundary, with energy lower than Δ, will be reflected as a hole whilst forming a Cooper pair within the superconductor

2.10.2   The superconducting side

The starting point of the BTK model is to solve two time dependent Schrödinger equations coupled by the superconducting energy gap Δ for a normal metal-superconductor junction or interface,

$$
\begin{aligned}
i\hbar \frac{\partial f}{\partial t} &= \left[-\frac{\hbar^2 \nabla^2}{2m} - \mu(x) + V(x) \right] f(x,t) + \Delta(x)\, g(x,t)\,, \\
i\hbar \frac{\partial g}{\partial t} &= -\left[-\frac{\hbar^2 \nabla^2}{2m} - \mu(x) + V(x) \right] g(x,t) + \Delta(x)\, f(x,t)\,.
\end{aligned}
\tag{2.84}
$$

Plane wave solutions of the following form, where u_0 and v_0 are taken to be real and positive,

$$
\begin{aligned}
f(x,t) &= u_0 e^{ikx-iEt/\hbar} \,, \\
g(x,t) &= v_0 e^{ikx-iEt/\hbar} \,,
\end{aligned}
\tag{2.85}
$$

allow for the time dependence to be factored out, resulting in the Bogoliubov-de Gennes equations, Eq. (2.71). Thus all of the expressions derived in Sec. 2.9 apply to the superconducting part of the junction.

The solutions to Eq. (2.84) can thus be written as

$$
\psi_{\pm k_{e/h}} = \begin{bmatrix} u_0 \\ v_0 \end{bmatrix} e^{\pm ik_{e/h}x} \,.
\tag{2.86}
$$

In the normal metal the superconducting pairing potential is zero, $\Delta_N(x) = 0$. Then in Eq. (2.84) the wavefunction f describes an electron, whilst the wavefunction g is a solution to a time-reversed Schrödinger equation. A time-reversed electron can be considered a hole, so f and g can be interpreted as describing electrons and holes respectively. When $V(x)$ is constant, which is the usual approximation in the BCS model, f and g are proportional to the electron and hole occupation probabilities, u_0 and v_0 [130]. Hence Eq. (2.86) describes quasiparticle excitations in the superconductor.

The one-dimensional Hamiltonian incorporating the chemical potential μ of the condensate is

$$
H(x) = -\frac{\hbar^2 \nabla^2}{2m} - \mu(x) + V(x) \,,
\tag{2.87}
$$

where the potential

$$
V(x) = h\delta(x),
\tag{2.88}
$$

describes the contact resistance or an oxide layer between the metals at the interface $x = 0$, h is a real valued constant. For simplification it is assumed that $\mu(x)$, $V(x)$ and $\Delta(x)$ are all constants with the values $\mu(x) = \mu$, $V(x) = 0$ and

$$
\Delta(x) = \begin{cases} 0 \text{ for } x < 0 \text{ (normal metal)} \,, \\ \Delta \text{ for } x \geq 0 \text{ (superconductor)} \,. \end{cases}
\tag{2.89}
$$

2.10.3   The normal metal side

In the normal metal the two equations in (2.84) decouple due to vanishing Δ and the energy-momentum relations are

$$
E_{k_e} = \frac{\hbar^2 k_e^2}{2m} - \varepsilon_k
\tag{2.90}
$$

and

$$E_{k_h} = \varepsilon_k - \frac{\hbar^2 k_h^2}{2m} \, , \tag{2.91}$$

for electrons and holes, respectively. The Fermi energy is $\varepsilon_k = \mu$ at zero temperature and the corresponding Fermi wave vector takes two values

$$k_F = \pm \frac{\sqrt{2\mu m}}{\hbar} \, . \tag{2.92}$$

Keeping in mind the physics of the matter, below the Fermi energy only hole excitations are possible since all electrons are in the ground state. However above the Fermi energy, electron excitations can occur, Fig. 2.12.
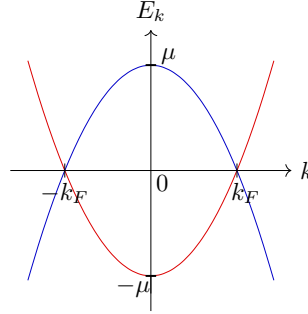
Figure 2.12: Degeneracy and character of the wave vector **k** in a normal metal.

2.10.4 The interface

Figure 2.13 shows the dispersion at the normal metal-superconductor interface along with the plane wave propagation modes for the BdG solutions in the normal metal

$$\psi_N(x) = \begin{bmatrix} 1 \\ 0 \end{bmatrix} e^{ik_e^N x} + a \begin{bmatrix} 0 \\ 1 \end{bmatrix} e^{ik_h^N x} + b \begin{bmatrix} 1 \\ 0 \end{bmatrix} e^{-ik_e^N x}, \tag{2.93}$$

and the superconductor

$$\psi_S(x) = c \begin{bmatrix} u_0 \\ v_0 \end{bmatrix} e^{ik_e^S x} + d \begin{bmatrix} v_0 \\ u_0 \end{bmatrix} e^{-ik_h^S x} \, . \tag{2.94}$$

Using the condition of continuity to match the wavefunctions and their first derivative at the junction $x = 0$, $\psi_N(0) = \psi_S(0)$ and $(\hbar/2m)(\psi_S'(0) - \psi_N'(0)) = h\psi(0)$, the coefficients a, b, c and d can be found. The main assumption of the BTK analysis is

the Andreev approximation, where all wavevectors, both in the superconductor and the normal metal, are assumed to be very close to k_F,

$$k_e^N \approx k_h^N \approx k_e^S \approx k_h^S \approx k_F \,, \tag{2.95}$$

which considerably simplifies the analysis and results in the aforementioned coefficients of reflection in Eq. (2.83) and the following coefficients of transmission

$$c = \frac{u_0(1 - iZ)}{u_0^2 + (u_0^2 - v_0^2)Z^2}, \; d = \frac{iv_0Z}{u_0^2 + (u_0^2 - v_0^2)Z^2} \,. \tag{2.96}$$
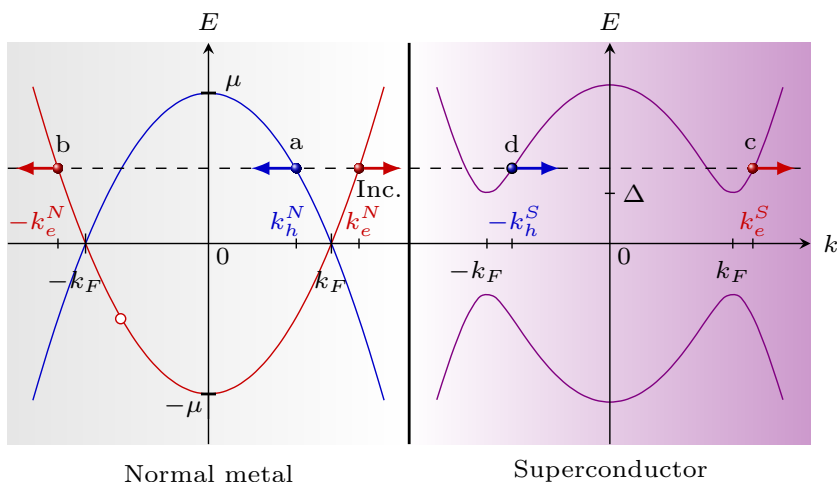
Figure 2.13: Dispersion relation at a normal metal-superconductor interface. An incident electron from the left with energy above Δ (Inc.) has probability of being reflected (b), retro-reflected as a hole (a), transmitted as a hole-like quasiparticle (d) or an electron-like quasiparticle (c) [132, 136].

Despite having clarified the concept of Andreev reflection at a normal metal-superconductor interface, we have not explained how Cooper pairs explicitly move from the superconductor to the normal metal. One of the authors of the BTK paper, Klapwijk, stated in 2004 that the following self-consistency equation, is a necessary part of the analysis even though it had been ignored due to the simplistic geometry [135],

$$\Delta(\mathbf{r}) = V_{\mathbf{k}}F(\mathbf{r}) = V \sum_{E>0} v^*(\mathbf{r}) \, u(\mathbf{r})[1 - 2f(E)] \,. \tag{2.97}$$

Here, $f(E)$ is the Fermi distribution function, $V_{\mathbf{k}}$ is the approximate mean field pairing interaction and $F(\mathbf{r})$ is the order parameter,

$$F(\mathbf{r}) = \langle \psi(\mathbf{r}_\uparrow)\psi(\mathbf{r}_\downarrow) \rangle \,, \tag{2.98}$$

which can be said to correspond to the Cooper pair density [123]. As noted in Refs. [135] and [138], even though the pairing interaction $V_{\mathbf{k}}$ vanishes at the interface, resulting in $\Delta = 0$, the order parameter $F(\mathbf{r})$ can be non-zero in the normal metal, due to coherence of electrons and holes, u and v, which underlies the proximity effect.

2.10.5 Optical retro-reflection

If the energy of an incident electron (2.80) is smaller than the superconducting gap, then the wave vector obtains an imaginary component. Waves of this type are evanescent waves which are well known in optics, formed when total internal reflection occurs at a boundary. Despite having been known for a long time, only recently their measurable effect in the electromagnetic setting was theorized [139] and shortly after detected [140].

Retro-reflection and phase conjugation are considered characteristic aspects of Andreev reflection. Both properties are manifested in non-linear optics of phase conjugate mirrors [141], Fig. 2.14. A remarkable property in the optical case is that a scattering barrier between a light source and a phase conjugate mirror becomes invisible in the sense that due to retro-reflection, the scattering is retraced back along the original ray trajectory [142]. This behavior was originally considered to be associated with time-reversal symmetry but rigorous derivation has shown that is not the case [143]. The analogy is not exact due to an additional phase factor obtained in the case of Andreev reflection and so a scattering barrier imposed between a normal metal and superconductor will not be invisible, despite retro-reflection [141].
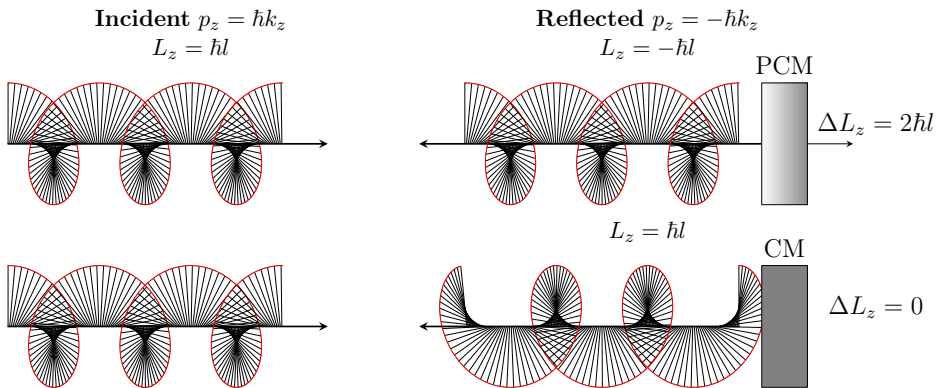
Figure 2.14: Comparison of reflection from a phase conjugate mirror (PCM), upper row, and conventional mirror (CM), lower row. In the case of the PCM, rotational recoil keeps the chirality of the reflected wave [144].

2.11 Superfluidity

Worthy of mention is the completely analogous effect to superconductivity in fluids, superfluidity. Both effects have in common the sustaining of constant currents without resistance or friction. With the same approach as in GL theory, Chap. 2.3, one can describe the superfluidic state by a wavefunction [119]

$$\psi_f(\mathbf{r}) = \psi_{f_0} e^{i\theta(\mathbf{r})}, \tag{2.99}$$

where $\theta(\mathbf{r})$ is a real valued phase function. Applying the momentum operator $\hat{\mathbf{p}} = -i\hbar\boldsymbol{\nabla}$ to the wavefunction leads to an expression for the superfluid velocity,

$$\mathbf{v}_f(\mathbf{r}) = \frac{\hbar}{m}\boldsymbol{\nabla}\theta(\mathbf{r})\,. \tag{2.100}$$

Therefore, the phase of the superfluid wavefunction takes on the role of a velocity potential Φ,

$$\theta = \frac{m}{\hbar}\,\Phi\,. \tag{2.101}$$

This leads to the observation that the gauge function (2.47) and the velocity potential are analogous, which implies that the superfluid velocity $\mathbf{v}_f$ and the magnetic vector potential share the same role. From Eq. (2.100) it is evident that the phase is uniform for a fluid at rest and that in the case of a constant superfluid velocity, the phase has uniform variation in the direction of the velocity. Comparable to the London equation (2.9), for superfluids [119]

$$\mathbf{J}_f = \rho_f \mathbf{v}_f\,. \tag{2.102}$$

A Navier-Stokes like equation can be formulated describing the acceleration of the superfluid using the total convective time derivative,

$$\frac{D}{Dt} = \frac{\partial}{\partial t} + \mathbf{v}\cdot\boldsymbol{\nabla}, \tag{2.103}$$

where $\mathbf{v}$ is the velocity of the fluid element itself. A similar treatment should then be possible in the case of superconductors.

Superfluids have the interesting property of having more than one mode of density waves or sound waves, termed second sound. There are essentially two more modes, the third sound having been both predicted and measured [145]. The second sound can be seen as an entropy wave, where the normal fluid part and the superfluid part of the liquid move with opposite phase resulting in zero net mass flow [119]. The phenomena was only known to occur at temperature up to a few Kelvin but second sound was recently observed for the first time at temperatures above 100 K in graphene [146].

Sinha et al. [147] recognized similarities of Dirac's theory of electrons [148, 149] with superfluidity and proposed that the vacuum is a superfluid state of particle and antiparticle pairs. Assuming that the pairs are in the ground orbital state with a zero value of the total spin in the second quantization momentum representation, the Hamiltonian describing a sea of particle-antiparticle pairs is

$$H = \sum_{\mathbf{k}} \varepsilon_{\mathbf{k}} c_{\mathbf{k}\downarrow}^{\dagger} c_{\mathbf{k}\downarrow} + \varepsilon_{\mathbf{k}} d_{\mathbf{k}\uparrow}^{\dagger} d_{\mathbf{k}\uparrow} - \sum_{\mathbf{k},\mathbf{k'}} V_{\mathbf{k},\mathbf{k'}} c_{\mathbf{k'}\downarrow}^{\dagger} d_{-\mathbf{k'}_{-\downarrow}}^{\dagger} d_{-\mathbf{k}_{-\downarrow}} c_{\mathbf{k}\downarrow} \, . \tag{2.104}$$

The operators $c^{\dagger}$ and $d^{\dagger}$ are the particle and antiparticle creation operators respectively, c and d are the corresponding annihilation operators. This model is very similar to the BCS Hamiltonian (2.60). As in BCS theory, $V_{\mathbf{k},\mathbf{k'}}$ is an effective short range pair interaction, but here of an unknown nature. Assuming it is constant, the ground state energy of the superfluid vacuum is lowered by a gap parameter Δ. Any object moving through the superfluid vacuum with energy below the gap parameter will not be able to exchange energy or momentum with it. The excitation energy of the vacuum will be

$$E_{\mathbf{k}} = \sqrt{\Delta^2 + \varepsilon_{\mathbf{k}}^2} \, , \tag{2.105}$$

By making the identification

$$\Delta = mc^2 \text{ and } \varepsilon_k = pc \, , \tag{2.106}$$

the relativistic energy-momentum relation is obtained,

$$E = \sqrt{(mc^2)^2 + (pc)^2} \, . \tag{2.107}$$

The speed of light is then seen as the critical velocity of the vacuum.
This idea has had a lively revival in recent years in relevance to dark matter [150–152] and observational implications have been proposed [152].

2.12   Gauge invariance in superconductivity

The question of gauge invariance becomes more pressing in superconductivity theory than in classical electrodynamics, since the observable supercurrent is directly proportional to the magnetic vector potential. Reconsidering the London equation (2.5), restated here for convenience

$$J_s = -\frac{1}{\Lambda}\mathbf{A} \, , \tag{2.108}$$

the transformation $\mathbf{A} \to \mathbf{A'} + \boldsymbol{\nabla}\chi$ is seen to change the supercurrent and so (2.108) is not gauge invariant. Taking the divergence of (2.108) gives

$$\boldsymbol{\nabla} \cdot \mathbf{J_s} = -\frac{1}{\Lambda}\boldsymbol{\nabla} \cdot \mathbf{A} \, . \tag{2.109}$$

For a solenoidal supercurrent or vortex,

$$\boldsymbol{\nabla} \cdot \mathbf{J_s} = 0$$

which necessitates the Coulomb gauge, also known as the London gauge,

$$\boldsymbol{\nabla} \cdot \mathbf{A} = 0.$$

From the canonical momentum for a multiply connected region, Eq. (2.46) can be rewritten using Eq. (2.47) as

$$\mathbf{v_s} = \frac{e}{m} \left(\boldsymbol{\nabla}\chi - \mathbf{A} \right) . \tag{2.110}$$

Together with Eq. (2.2) and Eq. (2.8),

$$\mathbf{J_s} = \frac{1}{\Lambda} \left(\boldsymbol{\nabla}\chi - \mathbf{A} \right) . \tag{2.111}$$

This is the expression for the current which conserves the probability density of a Schrödinger equation for a pair of particles interacting electromagnetically [121]. For a simply connected region, the phase is constant and London's equation (2.108) is recovered.

The problem of gauge invariance in BCS theory is found to be rooted in the assumptions that Cooper pairing consisted of zero-momentum pairs only, which corresponds to the order parameter $\langle \Psi_\uparrow \Psi_\downarrow \rangle$ being constant in space. A phonon like mode is needed to describe fluctuations in the order parameter [153]. This mode is in essence a *Goldstone* mode and turns out to be the gauge function χ (2.47). According to Goldstone's theorem, whenever a continuous symmetry is spontaneously broken, massless fields of Goldstone bosons emerge [154]. The Goldstone boson can be incorporated as a longitudinal mode of a gauge field, but in doing so the gauge field acquires mass. This process is the Higgs-mechanism [155], which has its roots in superconductivity theory with the works of Anderson [156] and Nambu [157]. The free energy Lagrangian in the Ginzburg-Landau model (2.26) can be used to illustrate the process in a simplified manner [158]. The third term in Eq. (2.26) describing the gauge covariant derivative of the wavefunction can be rewritten with $\psi = |\psi| e^{i\theta}$ along with Eq. (2.47), giving

$$\frac{\hbar^2}{2m^*} (\boldsymbol{\nabla}|\psi|)^2 + \frac{e^{*2}}{2m^*} (\boldsymbol{\nabla}\chi - \mathbf{A})^2 |\psi|^2 . \tag{2.112}$$

We can further rewrite this term by defining the field

$$\widetilde{\mathbf{A}} = \mathbf{A} - \boldsymbol{\nabla}\chi, \tag{2.113}$$

and obtain

$$\frac{\hbar^2}{2m^*} (\boldsymbol{\nabla}|\psi|)^2 + \frac{e^{*2}}{2m^*} \widetilde{\mathbf{A}}^2 |\psi|^2 . \tag{2.114}$$

The second term is a mass term, as quadratic terms are interpreted in field theory, analogous to classical kinetic energy

$$\frac{p^2}{2m} = \frac{1}{2}mv^2 \ .$$

(2.115)

By making the transformation in Eq. (2.113), the Goldstone mode χ has been incorporated into the potential $\widetilde{\mathbf{A}}$ and in the process, made the potential become the only mass term. Study of the Higgs mode in superconductors is currently underway [159] and like Majorana zero modes, it is part of an exciting synergy presently happening between condensed matter and particle physics.

Chapter 3

Majorana Zero Modes in Nanowires With Combined Triangular and Hexagonal Geometry

The effects of geometry on the hosting of Majorana zero modes are explored in core-shell nanowires with a hexagonal core and a triangular shell, and vice versa. The energy interval separating electronic states localized in the corners from states localized on the sides of the shell is shown to be larger for a triangular nanowire with a hexagonal core, than a triangular one. We build the topological phase diagram for both cases and compare them to earlier work on prismatic nanowires with the same core and shell geometry. We suggest that a dual core nanowire is needed to allow for a braiding operation of Majorana zero modes at the nanowire end plane.

3.1   Introduction

The most common model of a system with MZM is a semiconductor nanowire in contact with a metal superconductor [92, 93], which is a quasi-one-dimensional system. From the superconducting property, the Hamiltonian of a proximitized nanowire obtains an implicit particle-hole symmetry. With the application of an external magnetic field, time-reversal symmetry is broken and the system can support a $\mathbb{Z}_2$ topological invariant corresponding to the topological class D [160, 161]. The parameter space of such systems has been thoroughly explored with detailed calculations in order to predict the key conditions for experimental detection [160, 162].

Tubular nanowires of core-shell type provide an experimental platform to include all required aspects for hosting MZM [19]. Prismatic core-shell nanowires from various semiconductors have been fabricated and continue to be an active field of research [33, 163–168]. Recent numerical simulations have indicated that several

MZM's can be hosted in prismatic core-shell nanowires, where the electrons with low energies tend to localize around the prism edges [4,5]. This experimentally available system can be a host for previously discussed multichain ladder models [169–171].

In this chapter we present computational results for triangular nanowires with a hexagonal core (Tri-Hex), inspired by recently fabricated structures [33], and the inverse system, a hexagonal wire with a triangular core (Hex-Tri) which has also been obtained [172]. We show that the separation of energy levels of the Tri-Hex structure is significantly larger than in the case of a triangular core. With the Hex-Tri structure, the number of phase boundaries in the topological phase diagram is reduced, since the triangular core results in the ground states being localized at the three sides, rather than the six corners. The localization of MZMs is shown to correspond to the single particle localization of both configurations. The results suggest that these structures are worthy of further experimental investigation. To finalize, we discuss the possibility braiding MZM at the nanowire end planes.

3.2   Quantum mechanical model and methods

In the numerical calculations we use cylindrical coordinates, with the z axis along the nanowire. The geometry of the wire cross-section is defined by applying appropriate boundaries to a discretized disc in polar coordinates (ϕ, r) [173]. The Hamiltonian of the cross-section describes the transverse modes of the nanowire

$$H_t = \frac{(p_\phi - eA_\phi)^2}{2m_e} - \frac{\hbar^2}{2m_e r}\frac{\partial}{\partial r}\left(r\frac{\partial}{\partial r}\right), \tag{3.1}$$

where $p_\phi = -i\frac{\hbar}{r}\frac{\partial}{\partial \phi}$ is the momentum in the $\hat{\phi}$ direction, and $A_\phi = \frac{1}{2}Br$ the vector potential associated with the magnetic field of strength B oriented along the nanowire, in the symmetric gauge. The eigenstates of H_t can be written in terms of the lattice sites

$$|a\rangle = \sum_\kappa c_a |r_\kappa \phi_\kappa\rangle. \tag{3.2}$$

The nanowire length is incorporated with longitudinal modes which are given by

$$H_l = \frac{p_z^2}{2m_e}, \tag{3.3}$$

with the corresponding eigenstates

$$|k\rangle = L^{-1/2}\exp(ikz), \tag{3.4}$$

for an infinite nanowire, $L \to \infty$. In the case of a finite wire, with $z = 0$ set in the middle of the nanowire,

$$|n\rangle = L^{-1/2}\sqrt{2}\sin\left(n\pi\left(\frac{z}{L_z} + \frac{1}{2}\right)\right). \tag{3.5}$$

The Zeeman effect due to the applied external magnetic field is given in terms of the effective Landé g-factor, Bohr magneton μ_B, spin $|\sigma\rangle$ and magnetic field strength B,

$$H_Z = -g^* \mu_B \sigma B \,. \tag{3.6}$$

In order to satisfy the Majorana property, $\gamma = \gamma^\dagger$, the system needs to be effectively degenerated. Along with the Zeeman splitting, materials such as InAs or InSb are normally used in experiments due to the possibility of obtaining strong Rashba spin-obit coupling which lifts the spin degeneracy by coupling the spin to the momentum.

For a thin cylindrical shell the spin-orbit interaction can be modeled with the Hamiltonian

$$H_{SOI} = \frac{\alpha}{\hbar}(\sigma_\phi p_z - \sigma_z p_\phi) \,, \tag{3.7}$$

which corresponds to the regular planar model transformed in cylindrical coordinates [174], where α is the Rashba coupling constant. For a prismatic shell, a more elaborated model is in principle necessary, that should take into account the details of the nonuniform interface between the core and the shell. Recent calculations based on the $k \cdot p$ method indicate that the spin-orbit coupling inside the core can significantly increase due to the effective interface field, in the hexagonal geometry [175]. However, to our knowledge, no such study has been performed for the electrons situated in the shell. Since we shall deal mostly with electrons localized within narrow angular regions of the shell, on the corners or on the sides, we will assume they are experiencing a local effective electric field in the radial direction only, and we will use Eq. (3.7) as if that field did not depend on the angle ϕ. This model has been already used for describing Majorana states in core-shell nanowires with a simpler geometry [4, 5], and should be reasonable for a qualitative approach.

Our model of the core-shell nanowire is based on the composite Hamiltonian

$$H_w = H_t + H_l + H_Z + H_{SOI} \,. \tag{3.8}$$

The eigenstates and energy values for a finite wire are obtained by diagonalizing the matrix

$$\langle an\sigma|H_w|a'n'\sigma'\rangle \,. \tag{3.9}$$

The final ingredient needed to model MZM in the system is superconductivity. Due to the proximity effect, superconductivity is induced in the nanowire shell. The first hybrid superconductor-semiconductor nanowire systems consisted of nanowires lying on superconducting substrates [47]. The proximity effect was assumed induce superconductivity in the whole wire, given that the thickness of the nanowire is much smaller than the coherence length, ξ. More recently, nanowires covered with a superconductor have been fabricated with in-situ methods [48]. In such systems, the proximity effect can more rightly be assumed to be homogeneous in the system.

However, a complete superconductor shell will invoke the Little-Parks effect which has to be taken into account in the transport through the system [176].

The current analysis essentially describes a core-shell nanowire with an insulating or hollow core and a fully proximitized semiconductor shell, which is justified in the light of experimental results of Ref. [177]. Nonetheless, the authors are aware that the proximity effect deserves a more thorough treatment [178] as the temperature and sample geometry can both significantly influence the coherence length [179]. The superconducting property is incorporated by an order parameter Δ which couples two Schrödinger equations for electrons and holes with opposite spin in the Bogoliubv-DeGennes (BdG) Hamiltonian [180] which has been extensively used to describe quasiparticle excitations in superconductors [131].

The eigenstates of the BdG Hamiltonian have both electron and hole components and are written in the basis

$$|q\rangle = |\eta an\sigma\rangle = |\eta g\rangle \,, \tag{3.10}$$

where $|g\rangle$ denotes the basis for the finite wire Hamiltonian in Eq. (3.8) with the added electron-hole degree of freedom described with the isospin quantum number $\eta = \pm 1$. In the case of a finite wire, the longitudinal eigenstates are as in Eq. (3.4). The matrix elements are obtained for $\eta = \eta'$ with

$$\langle g\eta|H_{BdG}|g'\eta'\rangle = \eta[\text{Re}\langle g|H_w|g'\rangle \\ + i\eta\langle g|H_w|g'\rangle - \mu\delta_{gg'}], \tag{3.11}$$

and for $\eta \neq \eta'$,

$$\langle g\eta|H_{BdG}|g'\eta'\rangle = \eta\sigma\delta_{\sigma,-\sigma'}\delta_{aa'}\delta_{nn'}\Delta \,. \tag{3.12}$$

Note that the excitation energies are evaluated relative to the chemical potential μ, Eq. (3.11) which gives the BdG Hamiltonian an implicit particle-hole symmetry.

By calculating the spectra of both the finite and infinite cases for increasing magnetic field strength, a closing and reopening of the quasiparticle energy gap is observed with the emergence of topological edge states in the finite length spectrum [181, 182].

It has been shown that a pair of MZM will emerge for each corner in a prismatic core-shell nanowire but due to wavefunction overlap or tunneling caused by the finite width of the sides, some pairs will be shifted symmetrically above and below zero energy. In the case of three edges, one pair will be precisely at zero energy. The other two hybrid MZM's, slightly above and below zero energy, have been termed pseudo MZM's and will be referred to as such [4].

Throughout this work, our chosen parameters correspond to InSb with $\gamma = \frac{1}{2}g^*m_e = 0.393$, SOI parameter $\alpha = 1$ meV nm and a superconducting gap parameter $\Delta = 0.50$ meV. The number of sites used to describe the nanowire cross section is between 1700-2400.

3.3 Single-particle energies

Triangular nanowires with hexagonal cores have been fabricated with both side-matched (SM) cores [33], Figs. 3.1(c,d) and corner-matched (CM) cores [163], Figs. 3.1(e,f). To compare with earlier analysis [38] we explore the single-particle localization and the energy level separation of these nanowires, in conjunction with triangular cores, Figs. 3.1(a,b). The hexagonal core geometry enlarges the area of the corner localized peaks, whilst the side localization is suppressed, compared to the case of the triangular core. The side states of the triangular core are split by the hexagonal core geometry, resulting in two peaks per corner.
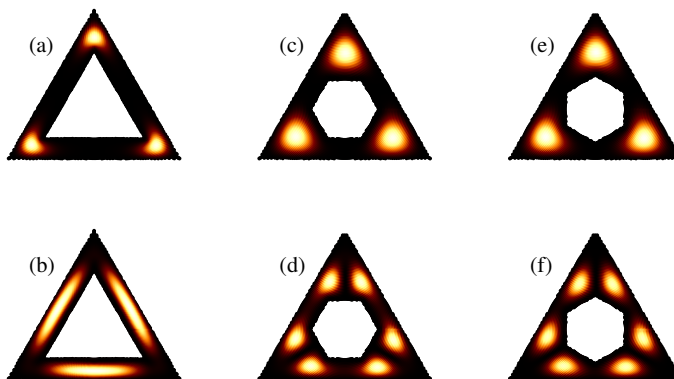
Figure 3.1: Single-particle cross-sectional localization of triangular nanowires with a triangular core (a,b), side-matched hexagonal core (c,d) and corner-matched hexagonal core (e,f). The upper row shows the corner localization of the first three quasi-degenerate energy states. The lower row shows the states of the adjacent energy level. The minimal shell thickness is 10 nm for the first two cases but slightly less in the corner matched case since the core is rotated with respect to the central case.

The hexagonal core geometry further results in a larger separation of the lowest (corner) states, Fig. 3.2, which is favourable for Majorana physics [4], as it provides more robust subspace of corner states. The energy separation decreases with increasing shell thickness - as the hexagonal core gets smaller, the wavefunction overlap at the sides becomes larger.
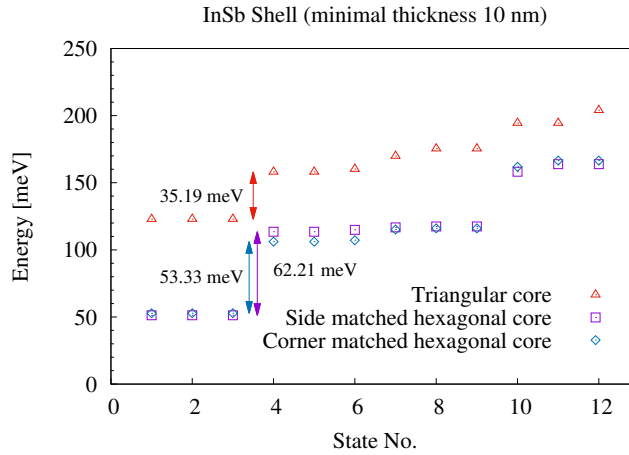
Figure 3.2: Single-particle energy states for the three triangular nanowire configurations. The three lowest-energy states are nearly degenerate and localized in the corners of the shell.

In the case of a hexagonal wire, Fig. 3.3, the triangular core outlines three sides with an enlarged area, compared to the hexagonal core. To the best of our knowledge, the corner-matched configuration (e,f) has not yet been fabricated, but is included in the analysis for the sake of completeness.

The separation of energy levels is larger for the case of a hexagonal wire with a triangular core compared to a hexagonal core, Fig. 3.4 but not as large as in the case of triangular wires. This is due to the overlap between localization peaks, which is clearly visible in Fig. 3.3(f). We say that the three states are quasi-degenerate as the degeneracy pattern is 1-2, 2-1 which becomes more evident for higher states in Figs. 3.2 and 3.4.
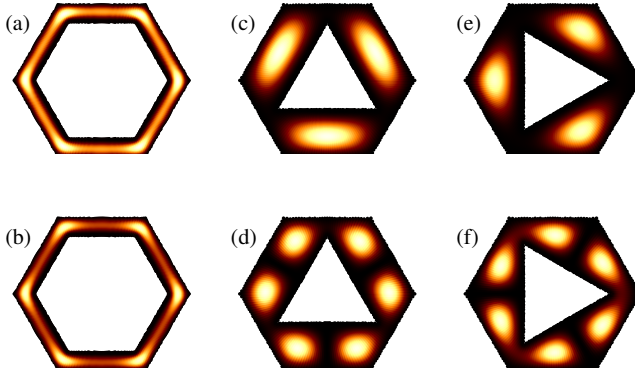
Figure 3.3: Single-particle cross-sectional localization of hexagonal nanowires with a hexagonal core (a,b), side-matched triangular core (c,d) and corner-matched triangular core (e,f). The upper row shows the first three quasi-degenerate energy states, which also describes the localization of the second energy level. The lower row shows the adjacent higher states. The minimal shell thickness is 10 nm for the first two cases but slightly more in the corner matched case since the core is rotated with respect to the central case.
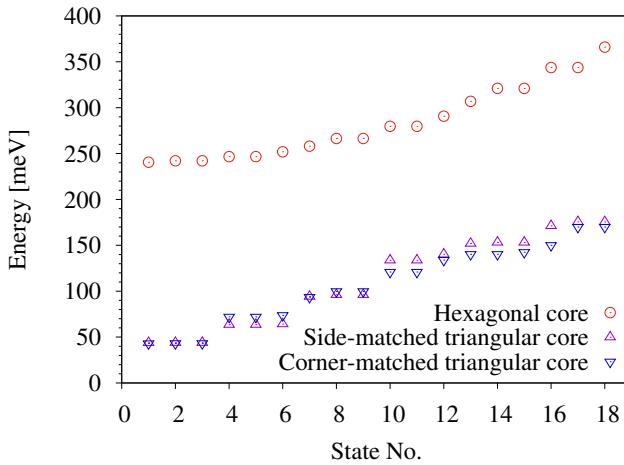
Figure 3.4: Single-particle energy states for the three hexagonal nanowire configurations.

3.4 Topological phase diagrams

First, the Tri-Hex nanowire is explored, with the cross section illustrated in Fig.
3.5(a). The radius of the nanowire i.e. the distance between the center and the exter-
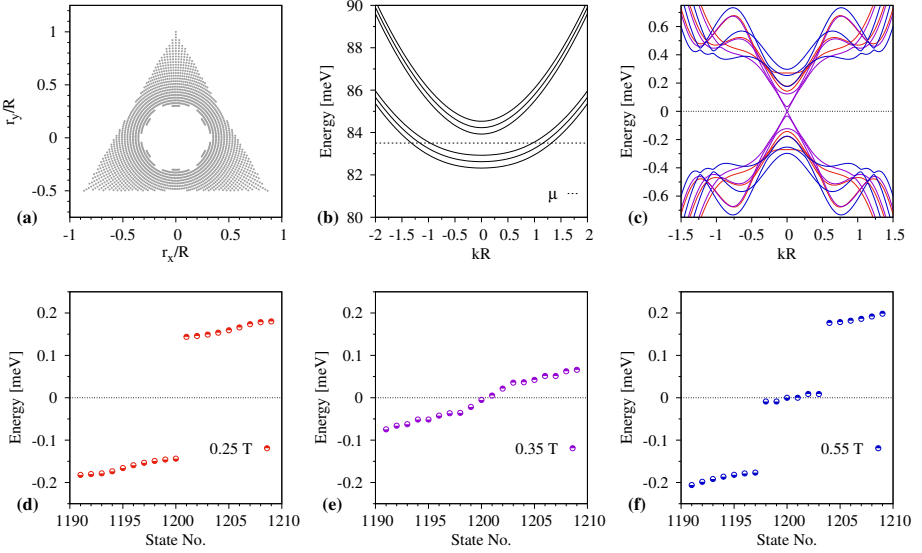
Figure 3.5: (a) Discretized nanowire cross section with Tri-Hex geometry, radius of
50 nm and 10 nm minimal shell thickness.
(b) Corresponding energy dispersion for an infinite wire in the presence of an exter-
nal magnetic field of magnitude 0.55 T.
(c) BdG quasiparticle spectra for an infinite wire showing the closing of the energy
gap as the longitudinal external magnetic field strength is increased. (d-f) Corre-
sponding energy spectra of a finite wire of length 200 R, showing the emergence of
Majorana Zero Modes. The line colors in figure (c) correspond to the magnetic field
values shown in panels (d-f).

nal corners, is $R = 50$ nm, the side thickness is 10 nm and the length 200R in the case
of the finite wire. Fig. 3.5(b) shows the energy dispersion for such a nanowire with in-
finite length, vs. the longitudinal wavevector times the nanowire radius, showing the
Zeeman splitting due to the external magnetic field applied parallel to the nanowire,
along with the value of the chemical potential, μ. Three values of magnetic field
strength are shown for the energy dispersion of the infinite wire BdG Hamiltonian
in Fig. 3.5(c), to indicate the onset of the MZM, with corresponding finite wire spec-
tra in in Figs. 3.5(d-f). Six states are formed around zero energy, one pair for each

corner of the nanowire section. In effect, a gap closing is required for each pair of zero modes forming in the spectrum.

By calculating the BdG spectra for a range of magnetic field strengths and values of the chemical potential, we can find for which set of parameters the BdG spectra closes. The closing of the BdG energy gap signifies a phase transition of the system from a topologically trivial state to a non-trivial one, with the emergence of a pair of edge states. The system can not be adiabatically deformed back to the original trivial state without closing the energy gap, just as a sphere can not be continuously deformed into a torus, therefore the states are considered topologically distinct [183, 184]. By plotting the ratio of the BdG energy and the superconducting gap parameter Δ at $k = 0$, as a function of the magnetic field strength and the chemical potential, a phase diagram is obtained [160, 185]. Since there are three states at the lowest energy, for both the Tri-Hex and Hex-Tri case, the system can host three pairs of edge states and there will be a closing of the BdG spectra for the emergence of each one. We will therefore have three curves on our phase diagrams which are boundaries between phases with different number of pairs of edge states [186, 187]. Topological phase diagrams of prismatic core-shell nanowires with uniform geometry have been recently studied [5]. Here we explore the effect of the core geometry on the phase diagrams. Since a realistic nanowire is not strictly symmetric, from now on we choose to slightly break the cross-sectional symmetry of our nanowires with a weak transverse electric field.

3.4.1 Tri-Hex nanowire geometry

For a minimal shell thickness of 10 nm, the phase diagram of the Tri-Hex systems consists of three lateral parabolas, which is the same phase diagram as for three isolated one dimensional nanowires [5]. In order to observe signs of wavefunction overlap between corners, the minimal shell thickness is increased to 12.5 nm, correspondingly the chemical potential is shifted to lower values compared to Fig. 3.5. Contrary to the phase diagram of three isolated wires, the tunneling removes the crossing of the phase boundaries, Fig. 3.6. The same phase diagram is observed for all three configurations of core geometry so only the side-matched case is presented.

We conclude that the effect of the hexagonal core is minimal for shell thickness up to 12.5 nm. Larger values will decrease the separation of energy levels, which is undesirable for hosting MZM [4] and are thus not further elaborated on here.
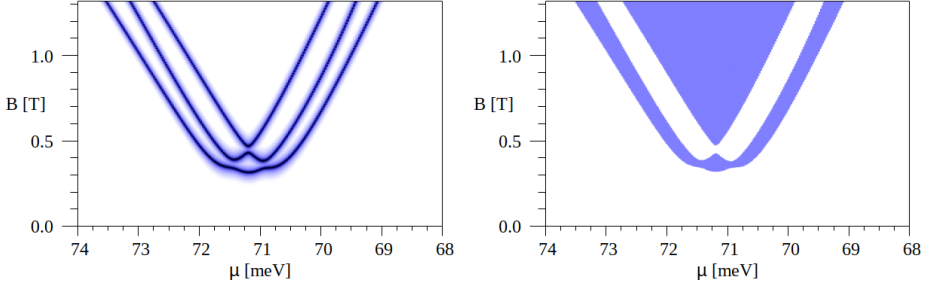
(a) Phase boundaries for $E_{BdG} = 0$ at $k = 0$.   (b) Shaded topological phase.

Figure 3.6: Phase diagram for a side-matched Tri-Hex structure with 12.5 nm shell thickness in a weak transverse electric field. For a specific value of the chemical potential, μ, the BdG energy gap alternately closes and reopens with an additional Majorana mode. For the first and third gap closing, the spectrum contains a proper zero mode at $E = 0$. For the second gap closing, the two Majorana modes are near zero energy, shifted slightly above and below zero due to finite size effects. In that case there is no exact zero mode such that the phase is topologically trivial.

3.4.2   Hex-Tri nanowire geometry

For a hexagonal wire with a triangular core, we can expect to see more signs of corner localization overlap between the sides of the wire, as the separation of energy levels is much smaller than in the case of the triangular wire, Fig. 3.4. As the differences between the side-matched and corner-matched cases is small, the phase diagram for the side-matched structure is presented only. In the topological phase diagram the presence of a threefold phase boundary signifies that the particles form three channels induced by the triangular core geometry, Fig. 3.7. The topological phase is entered at a lower value of both the chemical potential and magnetic field strength, compared to the Tri-Hex case, Fig. 3.6. Orbital Zeeman effects both skew the phase boundaries and lower the magnetic field strength threshold for the topological phase. Furthermore, combined with the spin Zeeman effect, they are responsible for the curious elliptic island [4], Fig. 3.7, around $\mu = 61.5$ meV and $B = 0.6$ T.

In Fig. 3.8, the lowest energy transverse states are shown with increasing strength of the external magnetic field. For the Tri-Hex geometry, flux periodic oscillations are suppressed. Due to the orbital Zeeman effect, slight oscillations are found for the Hex-Tri geometry, which is echoed in the corresponding phase diagram. The phase boundaries are three in number but a hexagonal core results in six phase boundaries [4]. The effect of the triangular core geometry is therefore quite significant in this case, mainly in that the number of phase boundaries is halved, compared to a hexagonal core.
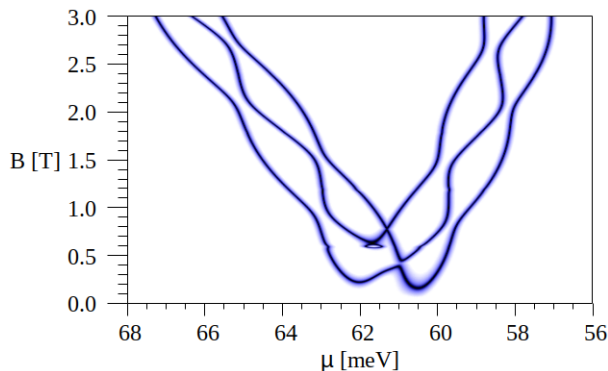
Figure 3.7: Phase diagram for a side-matched Hex-Tri structure with 10 nm shell thickness. Three topological phase boundaries, corresponding to the three sides of the triangular core are distinguished.
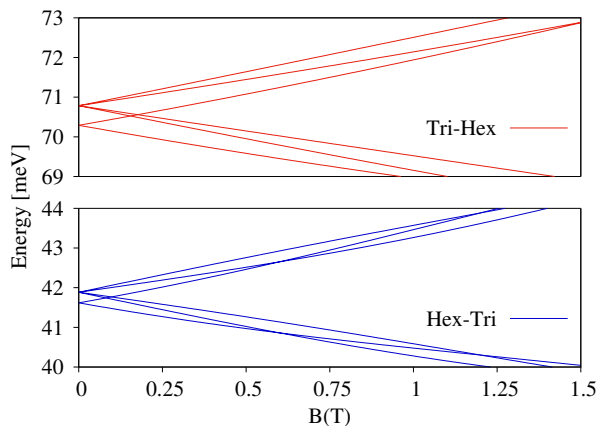
Figure 3.8: Lowest transverse energy states with increasing the magnetic field strength, compared for side-matched Tri-Hex and Hex-Tri wire geometries.

    The possibility of gap closing at non-zero values of the wave vector in the continuous spectrum was also considered. In all of the studied cases, the same phase diagram was obtained, meaning that these topological phases are stable [4].

3.5   Localization of Majorana Zero Modes

To explore the correspondence between the single-particle localization and MZM lo-
calization, the BdG probability density of the nanowire cross section at the end of
the wire is calculated. We find that for both the Tri-Hex and Hex-Tri structures, the
localization of MZM's, Fig. 3.9, coincides with the single-particle localization, Figs.
3.1 and 3.3, in that we have states localized at the largest area. The ideal MZM Fig.
3.9(c,d) at $E = 0$ differ from the pseudo MZM (a,b,e,f) by different weights of the
lowest (corner) states, controllable with the electric field. The degeneracy pattern
1-2, 2-1 is reflected in the localization. Only the side-matched cases are presented, as
the difference to the corner-matched cases is negligible.
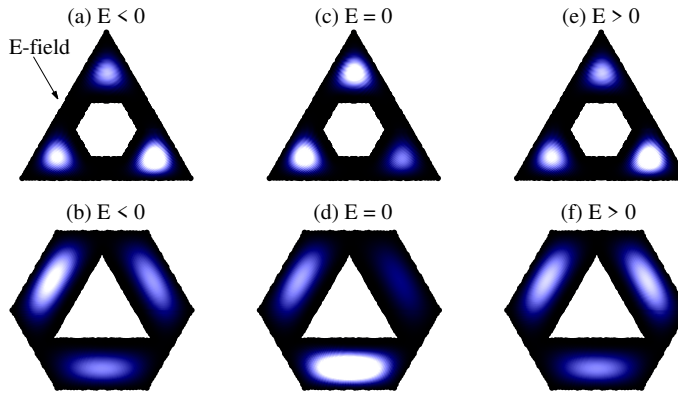
Figure 3.9: Localization of Majorana zero modes at the nanowire ends for side
matched Tri-Hex and Hex-Tri structures. The arrow shows the directionality of the
applied transverse electric field for all instances, breaking the localization symmetry.

To confirm that the MZM are localized at the ends of the nanowire, the BdG prob-
ability density of the corresponding state is calculated as a function of the nanowire
length, for a given point on the nanowire cross section. The longitudinal localization
for the corresponding top corner of the side-matched Tri-Hex, Fig. 3.9 can be seen in
Fig. 3.10. As expected, we observe strong edge localization which is characteristic of
the MZM and topological edge states in general [188, 189].
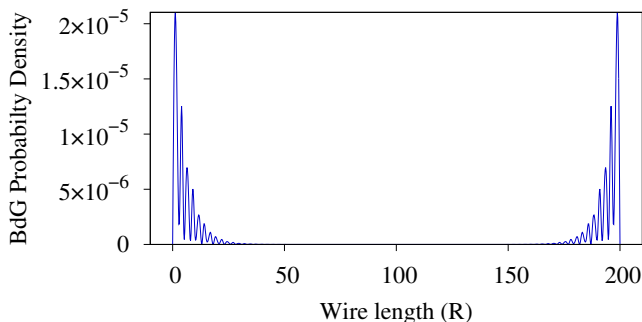
Figure 3.10: Single site lengthwise localization of an MZM. The probability density is greatest at the nanowire ends and falls off exponentially towards the nanowire center.

3.6 Discussion

In the light of the zero bias conductance peaks not being conclusive evidence [95], there is now a general consensus that braiding or fusing MZM is required as conclusive evidence to confirm experimentally their realization [1, 95]. Solely demonstrating topological phases as we have done here, is only the necessary foundation. Various schemes for braiding have been proposed [82]. In particular, braiding protocols for Y-junctions have been heavily studied [190, 191]. In such a system, one of the emerging problems is the misalignment of the longitudinal magnetic field, as the Y-junction does not lie on a single axis [192]. Braiding MZM's in the plane of the nanowire end will circumvent this problem. However, this can not be done in a single core nanowire as the MZM's would always meet up along the shell and fuse.

By fabricating a core-shell nanowire with two insulating cores or effectively so via doping, Fig. 3.11, this problem can be overcome. The next problem is then how the MZM's can be moved around in the nanowire end plane. Even though the MZM can be manipulated with an external electric field, that may not provide sufficient control to perform a braiding operation. Lastly, a readout is needed, based on a coupling of the fermion parity to an observable [82] in order to confirm that $\sigma_{AB}\sigma_{BC} \neq \sigma_{BC}\sigma_{AB}$. Formulation of an exact braiding scheme is beyond the our current scope. Here, we only intend to stimulate the discussion about braiding in the nanowire end planes, as the nanowire edges model three strands, needed to demonstrate the simplest non-commutative braiding operation.
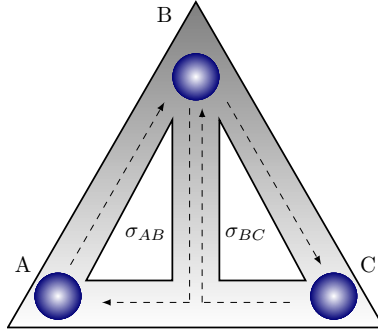
Figure 3.11: End plane of a hypothetical dual core-shell nanowire, providing suffi-
cient motional degrees of freedom for the braiding operations σ_{AB}, σ_{BC}.

3.7   Conclusions

By combining hexagonal and triangular geometry in nanowires of core-shell type,
both energy levels and topological phases can be influenced. With the polygonal
geometry, a well separated group of corner states is obtained. Here we show that the
separation of corner-localized energy levels is much larger for triangular nanowires
with hexagonal cores, compared to those with triangular cores of the same minimal
shell thickness, whilst the effect on the topological phase is minimal. On the contrary,
for the complimentary configuration of a hexagonal wire with a triangular core, the
effect on energy level separation is minimal whilst the effect on the topological phase
boundaries is significant. We find for both configurations that the localization of the
Majorana zero modes coincides with the single-particle localization. The problem of
braiding Majorana zero modes in a nanowire end plane is addressed and a split/dual
core structure is proposed as a system with the necessary motional degrees of freedom
for a three strand braiding operation.

Chapter 4

Electron-hole Coherence in Core-shell Nanowires With Partial Proximity-induced Superconductivity

The electron-hole coherence within a partially proximitized n-doped semiconductor shell of a core-shell nanowire heterostructure is investigated numerically and compared with the Andreev reflection interpretation of proximity induced superconductivity. Partial proximitization is considered to quantify the effects of a reduced coherence length. Three cases of partial proximitization of the shell are explored: radial, angular and longitudinal. For the radial case, it is found that the boundary conditions impose localization probability maxima in the center of the shell in spite of off-center radial proximitization. The induced superconductivity gap is calculated as a function of the ratio between the semiconducting and superconducting parts and the result is found to be independent of the shell thickness. In the angular case, the lowest energy state of a hexagonal wire with a single proximitized side is found to display the essence of Andreev reflection, only by lengthwise summation of the localization probability. In the longitudinal case, a clear correspondence with Andreev reflection is seen in the localization probability as a function of length along a half proximitized wire.

The proximity effect is generally hypothesized to stem from electron-hole coherence, brought on by Andreev reflection at the superconductor interface [134]. The superconducting proximity effect has resurfaced time after time in the past decades as a hot research topic due to relevance to research topics in each decade [135, 193–199]. Most recently due to the search for Majorana zero modes in nanostructures [13, 126, 200]. One of the earlier theoretical descriptions of the spatial dependence of the or-

der parameter in the superconducting proximity effect was done by MacMillan in 1968 [201], using a Green's function approach based on the Gor'kov equations [202] to describe a normal metal-superconductor (NS) junction. In this method, the BCS potential for a quasi 1D problem is written in terms of the pairing interaction $V(\boldsymbol{x})$ and the condensation amplitude $F(\boldsymbol{x})$,

$$\Delta(\mathbf{x}) = V(\mathbf{x})F(\mathbf{x}) \tag{4.1}$$

where F is given by an ensemble average [120]

$$F(\mathbf{x}) = \langle \hat{\psi}_\uparrow(\mathbf{x})\hat{\psi}_\downarrow(\mathbf{x}) \rangle. \tag{4.2}$$

MacMillan called the problem of the NS-junction possibly the simplest one in space-dependent superconductivity and proposed, in his own words, "a very nearly complete solution" of the problem for the case of infinite length of both metals, evaluating

$$F(\mathbf{x}) = \frac{1}{\pi} \int_0^{E_{c_0}} \mathrm{Im}[\mathcal{G}_{12}(E, \boldsymbol{x}, \boldsymbol{x}')] \, dE, \tag{4.3}$$

where E_{c_0} is the cut-off energy. $\mathcal{G}_{12}$ is the upper off-diagonal component of the 2×2 Green's function

$$\mathcal{G}(\mathbf{x}, t, \mathbf{x}', t') = -i\langle 0|T\{\Psi(\mathbf{x}, t)\Psi^\dagger(\mathbf{x}', t')\}|0\rangle, \tag{4.4}$$

written in the Nambu [203] spinor formalism,

$$\Psi(\mathbf{x}) = \begin{pmatrix} \hat{\psi}_\uparrow(\mathbf{x}) \\ \hat{\psi}_\downarrow^\dagger(\mathbf{x}) \end{pmatrix}, \tag{4.5}$$

where T denotes time ordering and $|0\rangle$ the Heisenberg ground state. $F(\boldsymbol{x})$ is also known as the anomalous Green function [123].

Another fundamental reference in the field is a book chapter written by Deutscher and de Gennes [204], published in 1969. There, the distinction between a clean and dirty junction is made and the following simplified results presented for the spatial dependence of the order parameter. For a clean metal, where the mean free path l_n therein is larger compared to the coherence length, $l_N > \xi_N$, the order parameter has the asymptotic form

$$F(\mathbf{x}) = \phi(\mathbf{x}) \exp\left(-\frac{2\pi k_B T}{\hbar v_F}|\boldsymbol{x}|\right), \tag{4.6}$$

where $\phi(\mathbf{x})$ is some slowly varying function, k_B is the Boltzmann constant, T denotes temperature and v_F is the Fermi velocity. For the limiting case of the temperature being close to zero a result by Falk from 1963 [205] is cited,

$$F(\mathbf{x}) \sim \frac{1}{|\boldsymbol{x}|}. \tag{4.7}$$

Falks paper [205] has a similar Green's function based approach of the Gor'kov equations as McMillan [201] and precedes McMillan's work by five years.

At present time, the effect of Andreev reflection is considered to be the mechanism behind the superconducting proximity effect [105, 136]. Described by Andreev in 1964 to explain the thermal resistance of the intermediate state in superconductor, Andreev reflection refers to the conjugate retro-reflection of electrons and holes at a metal-superconductor boundary [137], Fig. 4.1. Retro-reflection means that an incoming electron from the normal metal side is reflected such that it traces back the incident trajectory. In order for an incident electron at the normal metal side with energy below the gap parameter Δ, to be transferred across the boundary, the formation of a Cooper pair in the superconductor requires another electron with equal and opposite momentum which can be seen as a reflected hole.
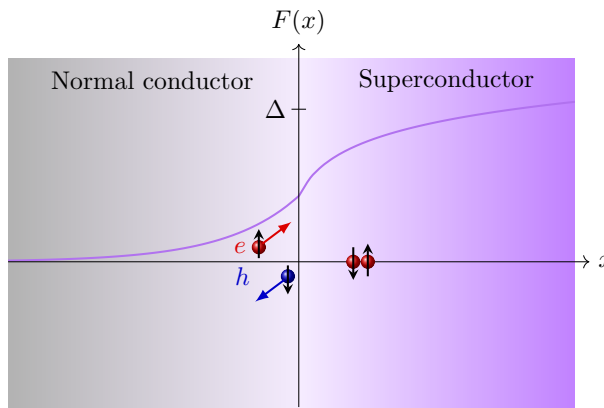
Figure 4.1: Simplified sketch of the proximity effect and Andreev reflection. An electron with energy $E < \Delta$ at an N-S boundary will be *retro-reflected* as a hole whilst forming a Cooper pair within the superconductor [132].

Blonder, Tinkham and Klapwijk (BTK) refined the scattering approach to the problem using the Bogoliubov equations and further computed I-V curves along with transmission and reflection coefficients for all cases of energy relative to the superconducting gap including a delta-barrier at the interface [132]. This work has since become seminal for Andreev reflection and is fundamental to most tunneling spectroscopy experiments on superconducting junctions [105]. The scattering formalism has the advantage of being readily interpreted and familiar from the standard educational problem in quantum mechanics of scattering from a potential barrier. Klapwijk [135] later noted that the following self-consistency equation was not included in the original BTK approach, and the superconducting gap implemented as a step

function at the interface. The self-consistency equation can be written as

$$\Delta(\mathbf{r}) = V(\mathbf{r})F(\mathbf{r}) = V(\mathbf{r})\sum_E u(\mathbf{r})v^\dagger(\mathbf{r})[1 - 2f(E)], \tag{4.8}$$

where $u(\mathbf{r})$ and $v(\mathbf{r})$ are the electron- and hole components of the quasiparticle wave-function respectively, and $f(E)$ is the Fermi-distribution function,

$$f(E) = [1 + \exp(E - \mu/(k_BT))]^{-1} . \tag{4.9}$$

Even if the pairing interaction $V(\mathbf{r})$ is zero in the normal metal, $F(\mathbf{r})$ can be non-zero, stemming from electron-hole coherence, which can be interpreted as the supercon-ductivity leakage in the normal metal [135]. The self-consistency equation deter-mines the variation of $\Delta(\mathbf{r})$ at the intersection but the general features of Andreev reflection are independent of it [206]. Self-consistency has been shown to be of great importance for interfaces of d-wave superconductivity [207]. Considerable work has been done in the past decade on the many subtleties of the superconducting gap pa-rameter in hybrid semiconductor-superconductor systems in relation to the quest for experimental realization of Majorana Zero Modes [208–211].

4.1 Model and methods

A three dimensional proximitized core-shell nanowire is modeled in the zero tem-perature limit using cylindrical coordinates, where the z-axis is defined along the wire growth direction. Using a divide and conquer algorithm coded in Fortran [212], energy spectra and states of the system are obtained by numerical diagonalization of the the Bogoliubov-de Gennes (BdG) Hamiltonian [131, 180]

$$H_{BdG} = \begin{pmatrix} [H_w - \mu] & \pm\Delta_{\uparrow\downarrow} \\ \mp\Delta^*_{\uparrow\downarrow} & -[H^*_w - \mu] \end{pmatrix}. \tag{4.10}$$

The matrix elements are written in the composite basis $|q\rangle$ consisting of the trans-verse modes $|a\rangle$, longitudinal modes $|n\rangle$, spin $|\sigma\rangle$ and particle-hole eigenstates $|\eta\rangle$ such that

$$|q\rangle = |\eta a n \sigma\rangle, \tag{4.11}$$

where $|an\sigma\rangle$ are the eigenstates of the Hamiltonian for the wire without proximty induced superconductivity,

$$H_{\mathrm{w}} = H_{\mathrm{t}} + H_{\mathrm{l}} + H_Z . \tag{4.12}$$

The transverse and longitudinal components of the Hamiltonian are written as

$$H_{\mathrm{t}} + H_{\mathrm{l}} = \frac{(p_\phi - eA_\phi)^2}{2m_e} - \frac{\hbar^2}{2m_e r}\frac{\partial}{\partial r}\left(r\frac{\partial}{\partial r}\right) + \frac{p_z^2}{2m_e}, \tag{4.13}$$

where $A_\phi = \frac{1}{2}Br$ is the vector potential in the symmetric gauge, incorporating an external magnetic field, **B**, directed along the wire axis. The transverse eigenstates are expanded in terms of the lattice sites

$$|a\rangle = \sum_\kappa c_a |r_\kappa \phi_\kappa\rangle , \qquad (4.14)$$

and matrix elements obtained by finite-difference discretization of derivatives [38, 39]. The cross-section geometry is added by infinite potential boundary conditions defining the hexagonal shape. For an infinite wire, the longitudinal modes are expressed in an exponential plane wave basis so that the Hamiltonian becomes a function of the longitudinal wave vector. For a finite wire, they are expanded in a sine basis,

$$|n\rangle = L_z^{-1/2}\sqrt{2}\sin\left(n\pi\left(\frac{z}{L_z}+\frac{1}{2}\right)\right) . \qquad (4.15)$$

The length of the wire is L_z, the origin is defined in the nanowire center so that the wire spans the interval $\left[\frac{-L_z}{2}, \frac{L_z}{2}\right]$ along the z axis. The external magnetic field B gives rise to the Zeeman term

$$H_Z = -g^*\mu_B \sigma B, \qquad (4.16)$$

where g^* is the effective Landé g-factor and μ_B the Bohr magneton. The particle-hole symmetry and coupling are contained in the quantum number $\eta = \pm 1$ and the matrix elements of the BdG Hamiltonian are then obtained by the following, for $\eta = \eta'$

$$\begin{aligned}\langle an\sigma\eta|H_{\text{BdG}}|a'n'\sigma'\eta'\rangle &= \eta[\text{Re}\langle an\sigma|H_{\text{w}}|a'n'\sigma'\rangle \\ &+ i\eta\langle an\sigma|H_{\text{w}}|a'n'\sigma'\rangle - \mu\delta_{(an\sigma)(a'n'\sigma')}],\end{aligned} \qquad (4.17)$$

and for $\eta \neq \eta'$,

$$\langle an\sigma\eta|H_{\text{BdG}}|a'n'\sigma'\eta'\rangle = \eta\sigma\delta_{\sigma,-\sigma'}\delta_{aa'}\delta_{nn'}\Delta_s . \qquad (4.18)$$

The chemical potential, μ, is situated to correspond to an n-doped semiconductor such that electrons are the main carriers of the system. Partial proximitization is implemented by a step function in the superconducting gap parameter, $\Delta_s(r,\phi,z)$, separately imposed in the radial, angular and longitudinal direction of the shell, so that ideal junctions with no interface barriers are formed in each case. In accordance with the original works of Andreev [137] and BTK [132], the induced gap is a fixed parameter and spin-orbit coupling is not considered. Model parameters are chosen to correspond to an InSb shell with $\gamma = g^*m_e/2 = 0.393$. The numerical simulations were performed for single shell nanowires with cross section diameter of 100 nm and shell thickness of $d = 10$ nm. For the finite wires, the length was set to 10 μm in sections 4.2 and 4.3 along with a shorter wire of 1 μm in section 4.4.

4.2   Partial radial proximitization

A core-shell nanowire fully coated with superconducting layer induces a radially symmetric proximitization of the shell. Full-shell nanowire systems allow for additional control of the superconducting energy gap due to the Little-Parks effect [48, 176, 213]. Partial radial proximitization of the shell would occur if the effective superconducting coherence length was suppressed in the sample [162]. A cylindrical shell is considered, to isolate the effect of a partial proximitization radially, Fig. 4.2(a). As the shell thickness d of the studied systems is much lower than the typical coherence length, this is arguably a rare instance for clean interfaces. Accordingly, the results are found to be independent of the shell thickness for the given diameter. Partial proximitization of a semiconductor wire with a superconductor having a $\Delta_s = 0.5$ meV gap results in an induced gap of $\Delta_i = 0.15$ meV of the whole system, Figs. 4.2(b,c). The wavefunction acquires the angular symmetry of the shell, the amplitude peak however is found to be centralized in the shell, irrespective of the radial asymmetry of proximitization. This follows from the boundary conditions of no hopping over the inner and outer boundary of the shell, which corresponds to vanishing of the wavefunction in the continuous lattice limit.

Note that according to Eq. (4.15), the probability amplitude oscillates along the wire length. The oscillation wavelength is determined by the chemical potential, Fig. 4.2(d), as the higher energy level increases the frequency. Figs. 4.2(e,f) show the longitudinal summation of probability amplitudes for the first five positive and negative energy states. In this case there is no straight forward correlation to retro-reflection of a hole component at the semiconducting-superconducting interface since the boundary conditions force the induced hole component to be equally localized over both the proximitized and non-proximitized parts of the wire shell.
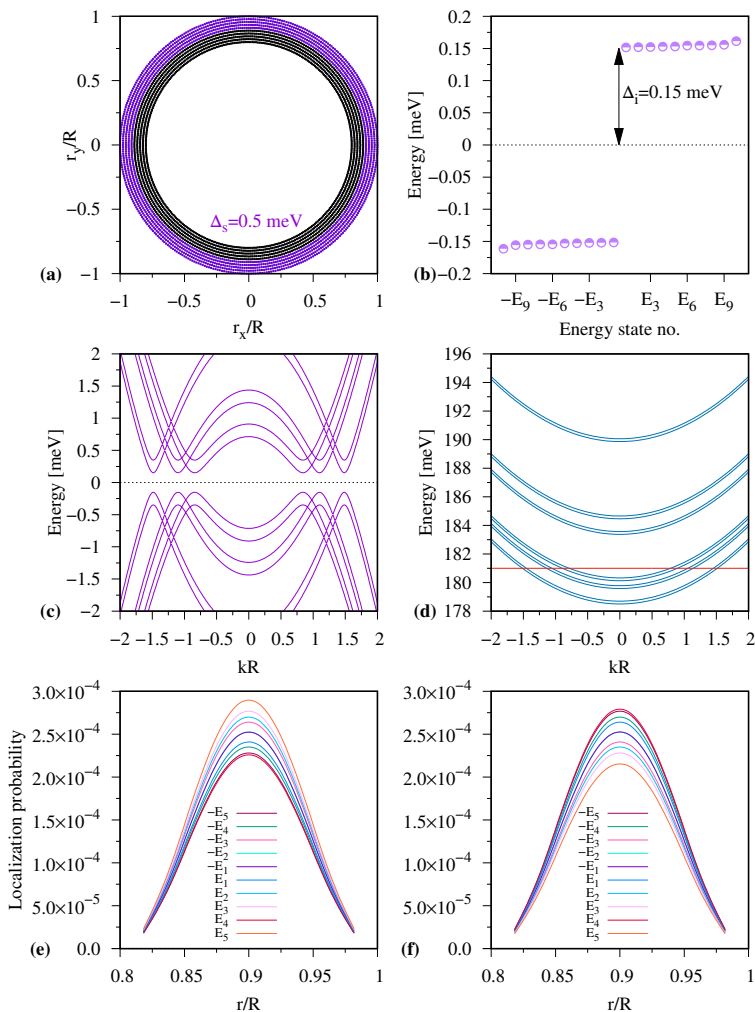
Figure 4.2: (a) Partial radial proximitization of the nanowire shell, half-proximitized shell with $\Delta_s = 0.5$ meV in the outer half (purple) of the shell. (b) Finite wire BdG spectrum of the nanowire system, showing the induced gap $\Delta_i = 0.15$ meV. (c) Infinite wire BdG energy spectra. (d) Energy dispersion and chemical potential (red) of the infinite wire. (e) Longitudinal summation of probability amplitudes on interior sites for the hole component $|v|^2$ of the lowest positive and negative energy states, for a single angular slice. (f) Longitudinal summation of probability amplitudes for the corresponding electronic component $|u|^2$.

In Fig. 4.3 the induced superconducting gap is shown as a function of the ratio between the non-proximitized and proximitized parts of the shell. The results are found to be independent of the shell thickness, for the given diameter of the wire. The superconducting gap parameter of the proximitized part is set to $\Delta_s = 0.5$ meV. The induced superconducting gap of the fully proximitized system is lowered by 10% due to the applied external magnetic field, $|\vec{B}| = 65.8$ mT, included in the simulation to lift spin degeneracy. The spin degeneracy is lifted to identify the chemical potential range that includes both spins in the presence of a magnetic field, the effects of which are further studied in Sect. 4.4.
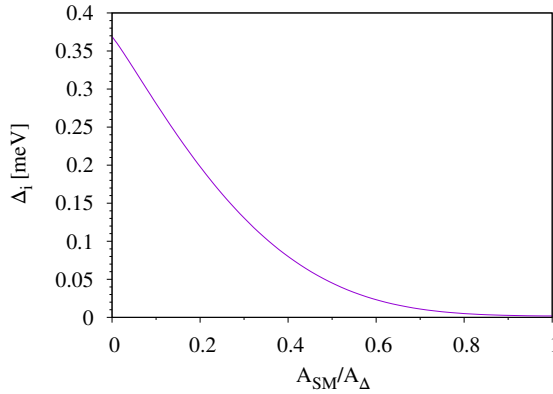
Figure 4.3: Induced superconducting energy gap of a partially proximitized nanowire as a function of the ratio of the non-proximitized area (A_{SM}) to the superconducting area (A_Δ).

4.3   Partial angular proximitization

Systems where nanowires are proximitized by fabrication of the wire on top of a superconducting slab are common experimental platforms for Majorana physics [95, 162, 214] . A hexagonal core-shell structure is considered to model such a system where the effective coherence length is smaller than the diameter of the nanowire, such that only a single side can be considered fully proximitized, Fig. 4.4(a).
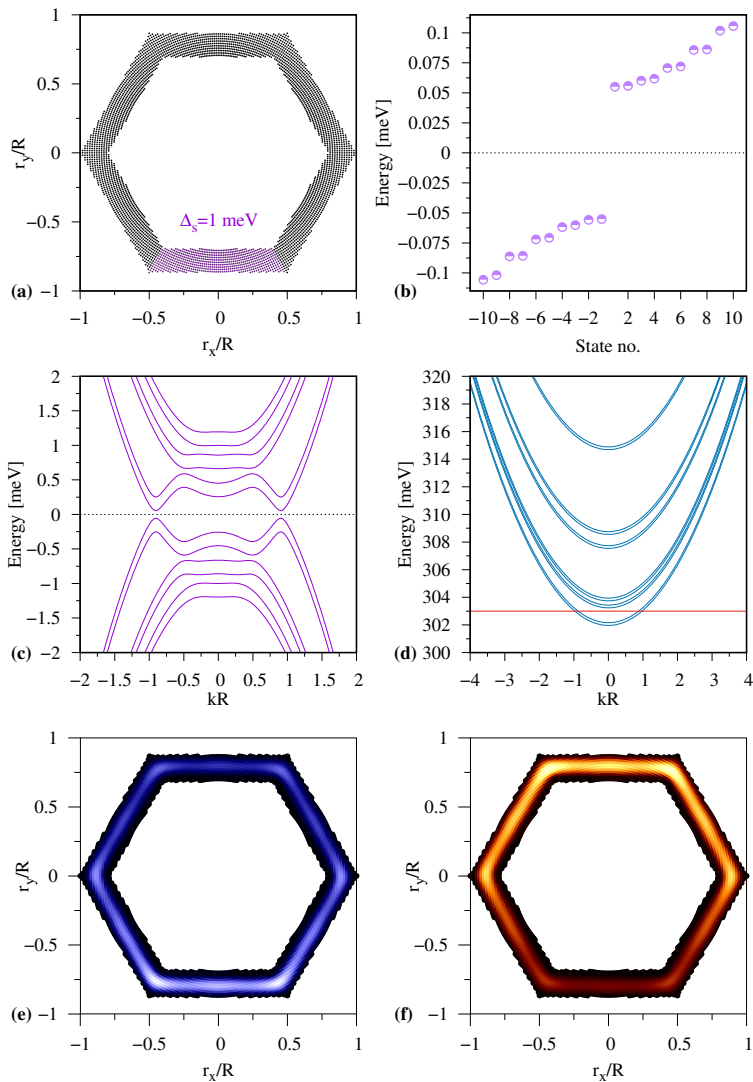
Figure 4.4: (a) Partial angular proximitization of a hexagonal nanowire shell, single side proximitization with $\Delta_s = 1$ meV. (b) Finite wire BdG spectrum of the whole system, showing the induced gap $\Delta_i = 0.05$ meV. (c) Infinite wire BdG spectra. (d) Dispersion and chemical potential (red) of the infinite wire Hamiltonian. (e) Longitudinal summation of probability amplitudes for the hole component $|v|^2$ of the lowest positive energy state, brightness denotes higher localization probability. (f) Corresponding electron component $|u|^2$.

In the fully proximitized part, the gap parameter is set at $\Delta_s = 1$ meV and the induced gap obtained is $\Delta_i = 0.05$ meV, Figs. 4.4(b,c). For the first excited positive energy quasiparticle state, in the case of the chemical potential including only the lowest energy band, Fig. 4.4(d), the Andreev picture of the proximity effect in uncovered. However, it is only for the lengthwise summation of localization probability such that the total localization probability is projected onto the wire cross-section, Figs. 4.4(e,f). The fully proximitized part of the semiconductor shell has a hole component localized within it, by definition of the BdG quasiparticle spectrum. Reminiscent of Andreev reflection, the hole components spreads out to the normal conducting part of the shell, Fig. 4.4(e). The electron amplitude is lowered within the superconducting shell, Fig. 4.4(f), in accordance with the view that the superconductor incorporates an electron to form a Cooper pair, and reflects a hole in the process [132]. The electron-hole coherence results in a near uniformly spread out BdG localization probability over the shell with amplitude peaks in the corners, due to corner localization [38]. The first negative energy state has the opposite electron-hole localization probability from Figs. 4.4(e,f), as expected from electron-hole symmetry of the system. Along the length of the wire, the wavefunction localization probability of each state oscillates, Sect. 4.4, and the symmetry of Figs. 4.4 (e,f) can be inverted at specific sites. This also happens for the adjacent higher energy states in which the particle-hole coherence is inverted since for a given energy value of the BdG spectra slightly above Δ, there are four states in each band, two electron dominant and the other two hole dominant.

4.4   Partial longitudinal proximitization

Another possibility of partial proximitization is partial covering of a nanowire longitudinally with a superconductor [95, 215]. A half proximitized wire is considered, such that the superconducting gap is uniform in the whole shell up to half the length of the wire, with $\Delta_S = 0.5$ meV. Fig. 4.5 shows the electron-hole coherence at a single corner site, for the case of no external magnetic field, of a long hexagonal nanowire with $L = 200$ R, where the diameter of the wire is 100 nm. An exponential decay of the composite BdG localization probability into the non-proximitized part is obtained, Fig. 4.5(a). This stems from coherence of electron and hole tunneling tails into the non-proximitized half of the wire, Fig. 4.5(b). Diminishing of the BdG localization probabilty in the proximitized half of the wire is caused by a phase difference between the electron and hole wavefunction components, the $-\pi/2$ phase difference is characteristic of Andreev reflection [206, 216]. If an external magnetic field is applied, Zeeman splitting gives rise to a difference between the k-vectors of the spin-split states. As the superconducting gap parameter couples opposite spin states, this results in an additional phase difference between the electron and hole components, Fig. 4.6(b). This phase difference leads to alternating constructive and deconstruc-

tive interference of the electron-hole coherence, resulting in a beating pattern of the BdG localization probability, Fig. 4.6(a).
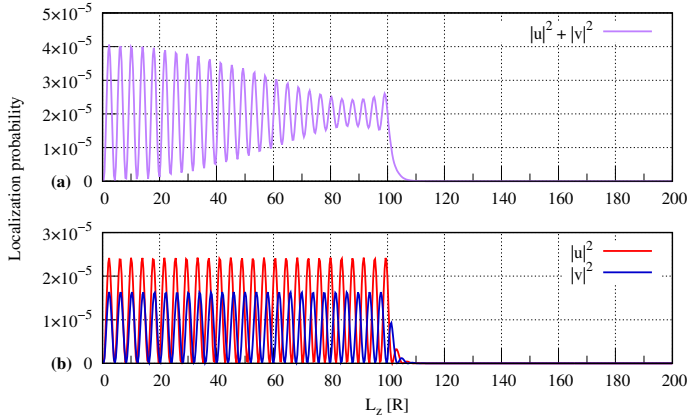
Figure 4.5: (a) Single corner site localization probability from the composite BdG wavefunction of the lowest energy state of a half proximitized hexagonal wire with no external magnetic field. (b) Corresponding electron and hole components, $|u|^2$ and $|v|^2$ respectively, showing a $-\pi/2$ phase difference at the interface.
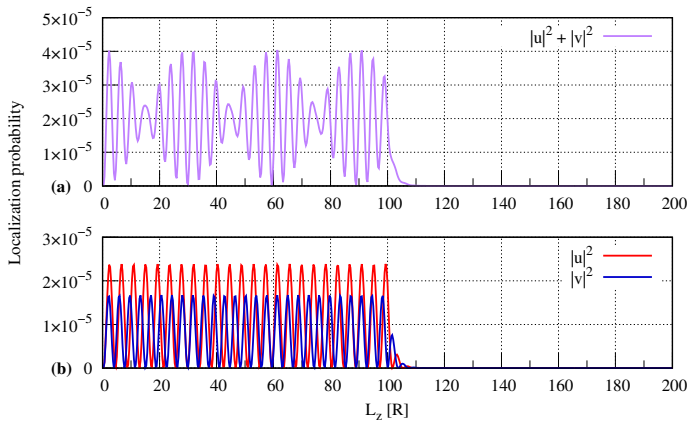
Figure 4.6: (a) Single corner site localization probability from the composite BdG wavefunction of the lowest energy state of a half proximitized hexagonal wire, for the case of an external magnetic field $|\vec{B}| = 65.8$ mT. (b) Corresponding electron and hole components, $|u|^2$ and $|v|^2$ respectively.

In the case of a weaker superconducting gap parameter $\Delta_S = 50\ \mu$eV, Fig. 4.7, the exponential decay into the semiconducting part is enlarged compared with Fig. 4.5. The gap parameter can thus be seen as an effective potential barrier for the electron-hole coherence.
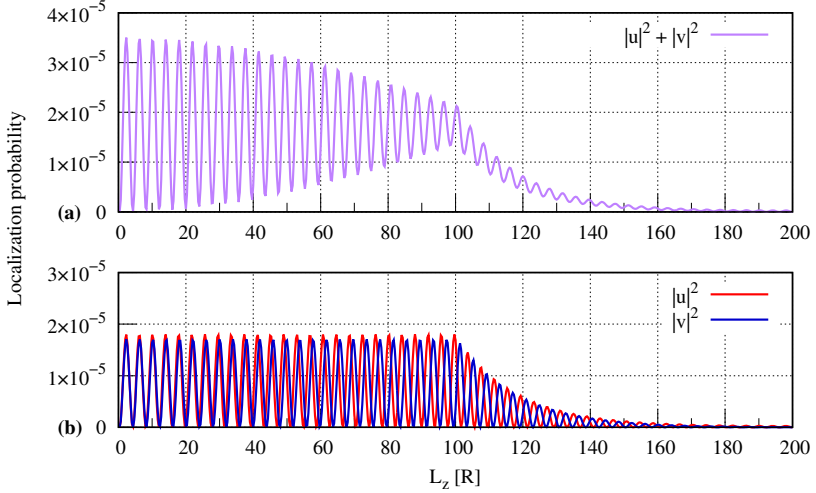
Figure 4.7: (a) Single corner site localization probability from the composite BdG wavefunction of the lowest energy state of a half proximitized hexagonal wire, $\Delta_S = 50\ \mu$eV, with no external magnetic field. (b) Corresponding electron and hole components, $|u|^2$ and $|v|^2$ respectively.

For a shorter wire with $L = 1\ \mu$m and $\Delta_S = 0.5$ meV, Fig. 4.8, the exponential decay is less pronounced, compared with Fig. 4.5. The coherence length is the same but the electron component at the interface is near minimum in phase, rather than at maximum as in the case of the longer wire. The wavelength of the wavefunction depends on the Fermi level, and so the length can influence the phase of the electron and hole components at the interface. In both cases correspondence with Andreev reflection is obtained, per site of the shell, where the leakage of the BdG wavefunction results from electron-hole coherence.
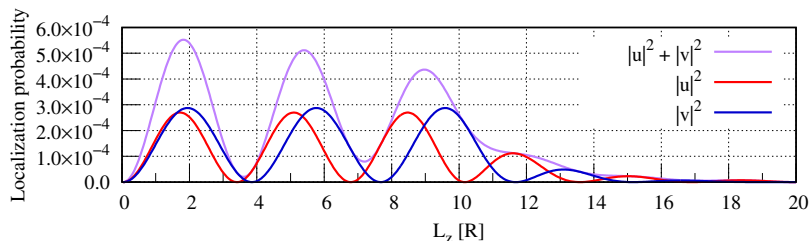
Figure 4.8: Single corner site localization probability of the composite BdG wavefunction and its corresponding electron $|u|^2$ and hole $|v|^2$ components of the lowest positive energy state.

4.5 Conclusions

Low energy physics of the radial, angular and longitudinal superconductor interfaces of proximitized core-shell nanowires has been explored using the Bogoliubov-de Gennes equations. Partial proximitization is considered to quantify the effects of a reduced coherence length and to investigate the Andreev reflection interpretation of proximitized superconductivity. For a thin shell, boundary conditions are found to impose symmetry of the localization probability in spite of partial radial proximitization. In the case of a hexagonal wire with a single proximitized side, it is only by lengthwise summation of localization probability that the essence of Andreev reflection can be seen. For a longitudinally half proximitized wire, electron-hole coherence is shown to cause the leakage of the BdG wavefunction into the non-proximitized part of the wire. Decreasing the superconducting gap strength is found to increase the spatial extent of electron-hole coherence. Correspondence with Andreev reflection is obtained per site of the shell, from considering the localization probability as a function of length in the core-shell nanowire system. The results show in what way Andreev reflection is compatible with electron-hole coherence at the various interfaces that can arise in proximitized core-shell nanowire systems.

72

Chapter 5

Flux-periodic Oscillations in Proximitized Full-shell Nanowires

In light of the recent in-situ advancements in fabrication of semiconductor nanowires fully covered with a superconducting material [217, 218], we explore flux periodic oscillations in the energy spectrum of proximitized core-shell nanowires modeled by the Bogoliubov-de Gennes (BdG) Hamiltonian [131]. Full-shell semiconductor-superconductor hybrids exhibit the Little-Parks effect when exposed to an external axial magnetic field, where oscillations of the superconducting transition temperature occur as a function in the unit of the superconducting flux quantum, $\Phi_0^{SC} = h/2e$, in which the factor of $2e$ is interpreted to be a signature of the charge pairing in Cooper pairs [219]. Along with solid core wires, hollow core cylinders with thin proximitized shells have been explored [176]. The Little-Park effect normally refers to oscillations in the transition temperature of thin superconducting cylinders and is attributed to supercurrents induced in the shell [220], Fig. 5.1.

The expression for the supercurrent in the semi-classical Ginzburg-Landau theory is the following [112]

$$\mathbf{J}_s = \frac{-i\hbar e^*}{2m^*}\left(\psi^\dagger \boldsymbol{\nabla}\psi - \psi\boldsymbol{\nabla}\psi^\dagger\right) - \frac{e^{*2}}{m^*}|\psi|^2\mathbf{A}\,. \tag{5.1}$$

Rewriting the supercurrent with $\psi = |\psi|e^{i\phi}$ and integrating around a closed contour gives [120]

$$\oint_C \mathbf{A}\cdot d\boldsymbol{\ell} + \frac{m^*}{e^{*2}}\oint_C |\psi|^{-2}\mathbf{J_S}\cdot d\boldsymbol{\ell} = \frac{\hbar}{e^*}\oint_C \boldsymbol{\nabla}\phi\cdot d\boldsymbol{\ell}\,, \tag{5.2}$$

where e^* and m^* are effective charge and mass. The right hand side integral must be an integer multiple $n \in \mathbb{N}$ of 2π if ψ is to be single valued, leading to the superconducting flux quantum

$$\Phi_0^{SC} = \frac{h}{2e}\,. \tag{5.3}$$

The left hand side of Eq. (5.2) can be rewritten in terms of the magnetic flux and supercurrent velocity [105], combining Eqs. (2.7), (2.9) and (2.22), one obtains

$$\oiint_S \mathbf{B} \cdot d\mathbf{S} + \frac{m^*}{2e} \oint \mathbf{v}_s \cdot d\boldsymbol{\ell} = n \cdot \Phi_0^{SC}, \tag{5.4}$$

which leads to

$$v_s = \frac{\hbar}{rm^*} \left(n - \frac{\Phi_B}{\Phi_0^{SC}} \right). \tag{5.5}$$

Since both the critical temperature and coherence length are proportional to the square of the supercurrent velocity [105], both become periodic functions of the magnetic flux with periodicity of Φ_0 [221].
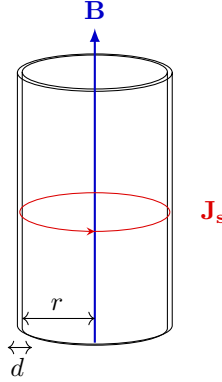
Figure 5.1: Experimental setup of Little and Parks [219].

In normal conducting rings and cylinders, flux periodicity of the energy spectra occurs as well with periodicity of $\Phi_0^N = h/e$. Consider a ring in the xy-plane in a uniform magnetic field $\mathbf{B} = B\,\mathbf{e}_z$ perpendicular to the plane of the ring. The total magnetic flux through the area enclosed by the radius of the ring, r, is

$$\Phi_B = \iint_S \mathbf{B} \cdot d\mathbf{S} = \pi r^2 B, \tag{5.6}$$

which can equally be expressed in terms of the magnetic vector potential using Green's curl theorem, working in cylindrical coordinates (r, θ, z),

$$\Phi_B = \oint_s \mathbf{A} \cdot d\ell = 2\pi r A_\theta. \tag{5.7}$$

The Hamiltonian of the system is given by

$$H_t = \frac{1}{2m_e}(\mathbf{p} - e\mathbf{A})^2 = \frac{1}{2m_e} \left(-\frac{i\hbar}{r} \frac{\partial}{\partial \theta} - \frac{e\Phi_B}{2\pi r} \right)^2. \tag{5.8}$$

The effective mass is $m_e = m_x \cdot m_0$ where m_0 is the electron rest mass and the parameter m_x is material dependent. Solving the time-independent Schrödinger equation $\hat{H}\psi = E\psi$ with the eigenfunctions $\psi = e^{il\theta}$ results in the energy spectrum

$$E_l = \frac{1}{2m_e}\left(\frac{\hbar}{r}l - \frac{e\Phi_B}{2\pi r}\right)^2 . \tag{5.9}$$

Rewriting in terms of the normal flux quantum, $\Phi_0^N = \frac{2\pi\hbar}{e} = \frac{h}{e}$,

$$E_l = \frac{\hbar^2}{2m_e r^2}\left(l - \frac{\Phi_B}{\Phi_0^N}\right)^2 . \tag{5.10}$$

Thus for a given energy level, periodic fluctuations occur with increasing magnetic field strength as states with increasing angular momentum are traversed, Fig.5.2.
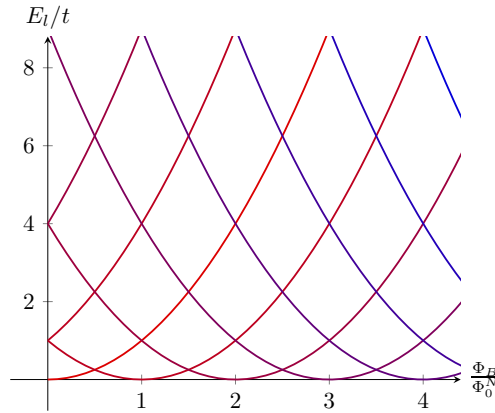
Figure 5.2: Flux-periodic oscillations of the energy spectrum E_l with $t = \hbar^2/2m_e r^2$. Colorscale denotes different quantum numbers l.

Spin can be implemented by doubling the internal degrees of freedom, leading to the Pauli equation with Zeeman interaction and spin-orbit coupling, which are also obtained by relativistic corrections to the Schrödinger equation in the non-relativistic limit of the Dirac equation [222]. In SI-units, the Pauli Hamiltonian with relativistic corrections becomes [223],

$$H_P = H_t - \frac{e\hbar}{2m}\boldsymbol{\sigma}\cdot\mathbf{B} - \frac{e\hbar}{4m^2c^2}\boldsymbol{\sigma}\cdot\mathbf{E}\times(\mathbf{p}-e\mathbf{A}) - \frac{e\hbar^2}{8m^2c^2}\left(i\boldsymbol{\sigma}\cdot\boldsymbol{\nabla}\times\mathbf{E}+\boldsymbol{\nabla}\cdot\mathbf{E}\right), \tag{5.11}$$

where the second term is the Zeeman interaction, the third and fourth terms account for spin-orbit coupling, the fifth term is the Darwin term, which can be seen as a kind of spin-orbit term for s-orbitals with zero angular momentum [224].

Due to the Zeeman interaction the energy bands are slightly shifted to higher and lower energies for spin up and down, Fig.5.3. The wavefunction becomes a composite entity for spin up and spin down. The Hamiltonian (5.8) with the Zeeman interaction is then

$$H_Z = H_t \sigma_0 - \boldsymbol{\mu} \cdot \mathbf{B}, \tag{5.12}$$

where the magnetic moment of a spin-1/2 particle has magnitude $|\boldsymbol{\mu}| = ge\hbar/4m$. The energy spectrum becomes spin dependent

$$E_{\uparrow\downarrow} = E_l \pm \frac{1}{2}g_e\mu_B|\boldsymbol{B}|, \tag{5.13}$$

where g_e is the effective g-factor and $\mu_B = -e\hbar/2m_0$ is the Bohr magneton. Defining the energy parameter $t = \hbar^2/2m_e r^2$ and factor $\gamma = m_x g_e/2$, Eq.(5.13) can be written as

$$t^{-1}E_{\uparrow\downarrow}\left(\frac{\Phi_B}{\Phi_0}\right) = \left(l - \frac{\Phi_B}{\Phi_0}\right)^2 \pm 2\gamma\frac{\Phi_B}{\Phi_0}. \tag{5.14}$$
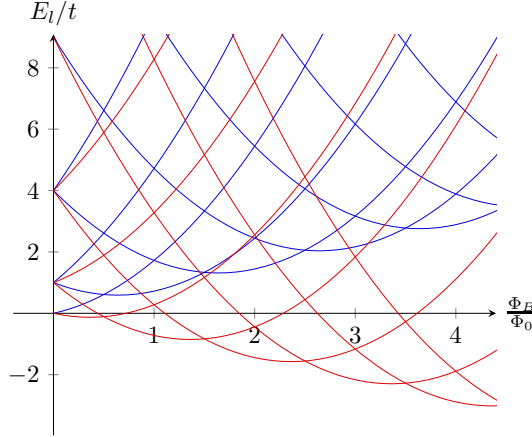
Figure 5.3: Flux-periodic oscillations of the energy spectrum E_l with $t = \hbar^2/2m_e r^2$ for spin up (red) and spin down (blue) for $\gamma = -0.361$ corresponding to InSb.

In materials, spin-orbit coupling falls into two categories, Rashba [225] and Dresselhaus [226], corresponding to surface and bulk inversion symmetry breaking respectively. In two dimensional systems, the spin-orbit Hamiltonian takes the form

$$H_{SOI}^{2D} = \hbar^{-1}[\alpha(\sigma_y p_x - \sigma_x p_y) + \beta(\sigma_x p_x - \sigma_y p_y)] = H_{SOI}^R + H_{SOI}^D, \tag{5.15}$$

where α and β are the Rashba and Dreselhaus coupling coefficients respectively. Surface inversion symmetry breaking at a planar interface of two materials results in an

uneven charge density, inducing an electric field perpendicular to the interface. The induced field is given by $\mathbf{E} = |\mathbf{E}|\hat{\mathbf{z}}$ if the interface lies in the xy-plane. Then

$$\frac{\alpha}{\hbar}(\sigma_y p_x - \sigma_x p_y) = \frac{\alpha}{\hbar}(\boldsymbol{\sigma} \times \mathbf{p}) \cdot \hat{\mathbf{z}} = -\frac{\alpha}{\hbar E_0}\boldsymbol{\sigma} \cdot (\mathbf{E} \times \mathbf{p}), \tag{5.16}$$

which shows the similarity to the spin-orbit term in Eq. (5.11). Determining material specific spin-orbit coupling constants requires a model on its own, such as the extended Kane model of $\mathbf{k} \cdot \mathbf{p}$ theory [227].

A core-shell wire with differing core and shell materials can be considered to host two-dimensional electron gas confined to the shell, which is embedded in the radial interface electric field [174]. Rashba spin-orbit coupling in such a model becomes an angular form of (5.16), with longitudinal and transverse components for momentum

$$H_{SOI} = \hbar^{-1}\alpha\left[\sigma_\phi p_z - \sigma_z p_\phi\right] = \hbar^{-1}[H_{SOI}^L + H_{SOI}^T]. \tag{5.17}$$

5.1 Model and methods

The model is essentially the same as in Sect. 3.2, but is restated here for the sake of completeness and to highlight relevant terms for the flux-periodic oscillations. The system in Fig. 5.4 is modelled by the Bogoliubov-de Gennes (BdG) Hamiltonian [131, 180],

$$H_{BdG} = \begin{pmatrix} [H_w - \mu] & \Delta \\ -\Delta^* & -[H_w^* - \mu] \end{pmatrix}, \tag{5.18}$$

which is solved by numerical diagonalization in Fortran. The superconducting gap parameter Δ, couples electrons and holes, effectively describing electron-hole coherence in the system. The gap parameter is assumed to be brought on by the proximity
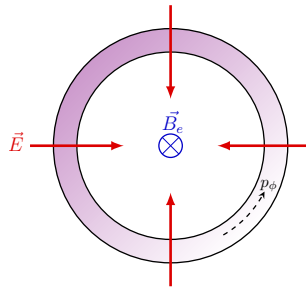
Figure 5.4: Nanowire cross-section showing the radial interface electric field $\vec{E}$ and applied external magnetic field $\vec{B}$ in the z-direction, p_ϕ is the angular momentum of electron carriers within the shell.

effect of a parent (surrounding) superconductor in the weak coupling limit [178].
Note that the gap parameter is constant, and no phase dependency is imposed on it.
At first sight, this may seem as ignoring the Little-Parks oscillations [219]. However,
the phase dependency is attributed to a supercurrent in the surrounding supercon-
ductor, described by an effective wavefunction for the whole condensate, Eq. 5.1, and
neither are included in the model. Nevertheless, as the shell is very thin and smaller
then the average coherence length, the external magnetic field should penetrate the
shell, depending on the thickness of the surrounding superconductor. From a phe-
nomenological viewpoint, this ought to induce supercurrents in the the shell which
would modulate the order parameter. Rather than imposing this phase dependency
from phenomenological considerations, it is set a constant on purpose to explore if
the BdG spectrum will exhibit h/e or $h/2e$ flux periodicity in this case.

The Hamiltonian for the wire in cylidrical coordinates is given by

$$H_w = H_t + H_l + H_Z + H_{SOI} \tag{5.19}$$

$$= \frac{(p_\phi - eA_\phi)^2}{2m_e} - \frac{\hbar^2}{2m_e r}\frac{\partial}{\partial r}\left(r\frac{\partial}{\partial r}\right) \tag{5.20}$$

$$+ \frac{p_z^2}{2m_e} - g^*\mu_B\sigma B \tag{5.21}$$

$$+ \frac{\alpha}{\hbar}\left[\sigma_\phi p_z - \sigma_z(p_\phi - eA_\phi)\right]. \tag{5.22}$$

The symmetric gauge vector potential $A_\phi = \frac{1}{2}Br$ incorporates the axial external mag-
netic field $\mathbf{B}$, giving rise to the Zeeman term H_Z where g^* is the effective Landé g-
factor and μ_B the Bohr magneton. The spin-orbit term describes the angular Rashba
interaction, arising from a radial electric field induced by crystal asymmetry at the
core-shell interface [174]. The magnetic vector potential couples linearly to the an-
gular momentum. The eigenstates of the wire Hamiltonian (5.19) are written in the
basis

$$|g\rangle = |an\sigma\rangle, \tag{5.23}$$

where a, n and σ denote transverse modes, longitudinal modes and spin, respectively.
Finite and infinite wires are modeled by considering longitudinal modes in both a
sine and exponential basis. The eigenstates (5.23) along with the particle-hole space
$|\eta\rangle$ form a basis $|q\rangle = |\eta g\rangle = |\eta an\sigma\rangle$ for the BdG Hamiltonian (5.18) with the fol-
lowing matrix elements. For $\eta = \eta'$

$$\langle q|H_{\text{BdG}}|q'\rangle = \eta[\text{Re}\langle an\sigma|H_w|a'n'\sigma'\rangle \\ + i\eta\langle an\sigma|H_w|a'n'\sigma'\rangle - \mu\delta_{(an\sigma)(a'n'\sigma')}], \tag{5.24}$$

and for $\eta \neq \eta'$,

$$\langle q|H_{\text{BdG}}|q'\rangle = \eta\sigma\delta_{\sigma,-\sigma'}\delta_{aa'}\delta_{nn'}\Delta_s. \tag{5.25}$$

Model parameters are chosen to correspond to a proximitized n-doped InSb semi-conducting shell with $\gamma = g^* m_e/2 = 0.393$, SOI parameter $\alpha = 1$ meV nm and $\Delta = 0.50$ meV. The chemical potential μ is set within the conduction band. The nanowire radius is $R = 50$ nm, shell thickness $d = 10$ nm and $L_z = 10$ μm. To explore flux-periodic oscillations, the state of the system is calculated for a range of magnetic field strength corresponding to a few flux quanta.

5.2 Cylindrical nanowire shell

The system is initialized at zero magnetic field strength and calculated step-wise up to a field strength of $|\mathbf{B}| = 1.30$ T with an interval of 0.013 T. Basis modes for the wire Hamiltonian are 9 transverse and 200 longitudinal. The chemical potential is situated above three spin-degenerate states in the absence of Zeeman and spin-orbit interaction. Four cases of vanishing/non-vanishing Zeeman and spin-orbit interaction are compared. Fig. 5.5 shows the state of the system at the maximum magnetic field strength. The Zeeman interaction lifts the spin-degeneracy. As a results the aligned spin becomes the lowest energy state in the spectrum of the infinite wire, Fig. 5.5(b) whilst the spin-orbit interaction leads to a slight mismatch in the two lowest and opposite spin states. Combining the Zeeman and Rashba spin-orbit interaction, the Zeeman interaction dominates. Note however that as the induced magnetic field by the spin-orbit interaction is parallel to the external magnetic field, Eq. (5.22), additional spin-splitting occurs for each flux quantum. The closing of the BdG gap in the infinite wire dispersion varies considerably between the cases, Fig. 5.5(c). In the case of a vanishing Zeeman and spin-orbit interaction, the gap never closes over the magnetic field cycle. In all other cases the gap closes, but at different momentum values. The finite wire BdG energy spectrum including the Zeeman or spin-orbit interaction separately is nearly aligned, Fig. 5.5(d), whilst combining the two increases the separation between non-degenerate eigenvalues, due to the combined spin-splitting.

Fig. 5.6 shows the flux-periodic oscillations of the lowest energy state of the finite and infinite normal- and superconducting wire at $k = 0$. The oscillations of the normal conducting wire, Fig. 5.6(a), are the same for the finite and infinite wire and display flux-periodicity of $2\Phi_0^{SC} = h/e$, in accordance with Eq. 5.10. The Rashba spin-orbit coupling has a phase shift effect on the oscillations whilst the Zeeman interaction introduces a linear dependence of the flux quantum in addition to the quadratic dependence, without altering the periodicity. Combing the two interactions merges these effects in an expected manner. The lowest energy state of the infinite wire BdG Hamiltonian at $k = 0$, Fig. 5.6(b), displays clear $h/2e$-periodic oscillations in the absence of both Zeeman and spin-orbit interaction. Adding the Zeeman interaction lifts the spin degeneracy and mixes spin-split quasiparticle bands. The strong g-factor overcomes the superconducting gap separation between electron- and hole dominant states, resulting in sub-oscillations with alternating inverted curvature profile, be-
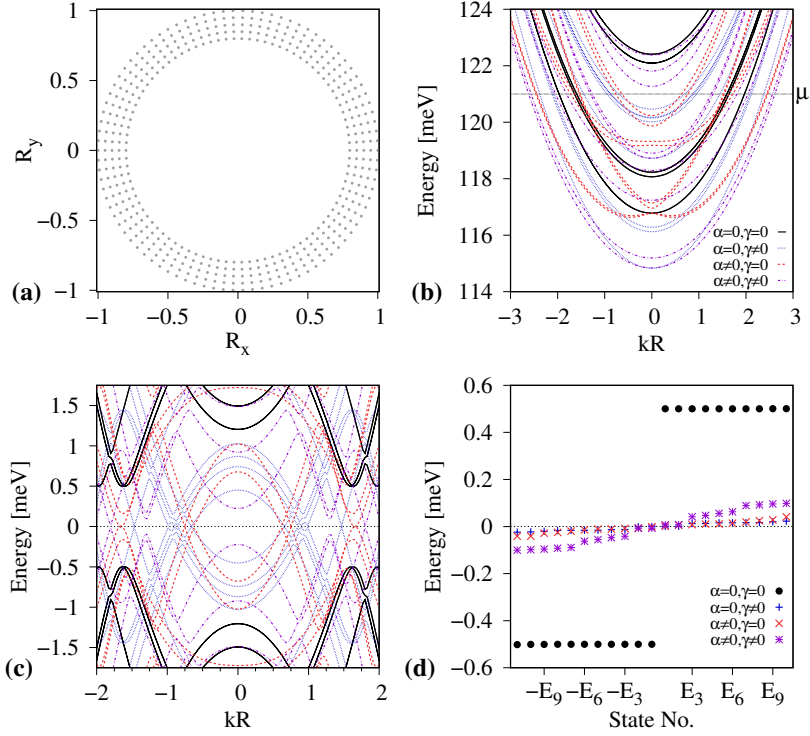
Figure 5.5: State of the nanowire system at magnetic field strength $|\mathbf{B}| = 1.30$ T. **(a)** Circular nanowire cross section with units $R = 50$ nm. Shell thickness of 10 nm. **(b)** Energy dispersion of the infinite wire nearby the chemical potential (μ), for the four cases of vanishing/non-vanishing Zeeman interaction (γ) and spin-orbit interaction (α). The dimensionless unit kR denotes the wavevector k times radius R. **(c)** Corresponding BdG quasiparticle energy dispersion for the infinite wire. **(d)** Finite wire BdG quasiparticle energy states.

yond a magnetic field strength corresponding to one superconducting flux quantum. The spin-orbit interaction causes a lateral spin-splitting of the dispersion, Fig. 5.5(b), which unevenly doubles the periodicity and sharpens the oscillations of all periods as opposite spin states are traversed. The combination of the Zeeman and spin-orbit interaction results in approximately alternating constructive and destructive coherence of the separate oscillations, breaking the periodicity. The detailed shape of the oscillations depends on the position of the chemical potential, which governs the transition between states of varying angular momentum. Fig. 5.6(c) shows the minimum energy for all values of the wavevector k. In the absence of both Zeeman and spin-
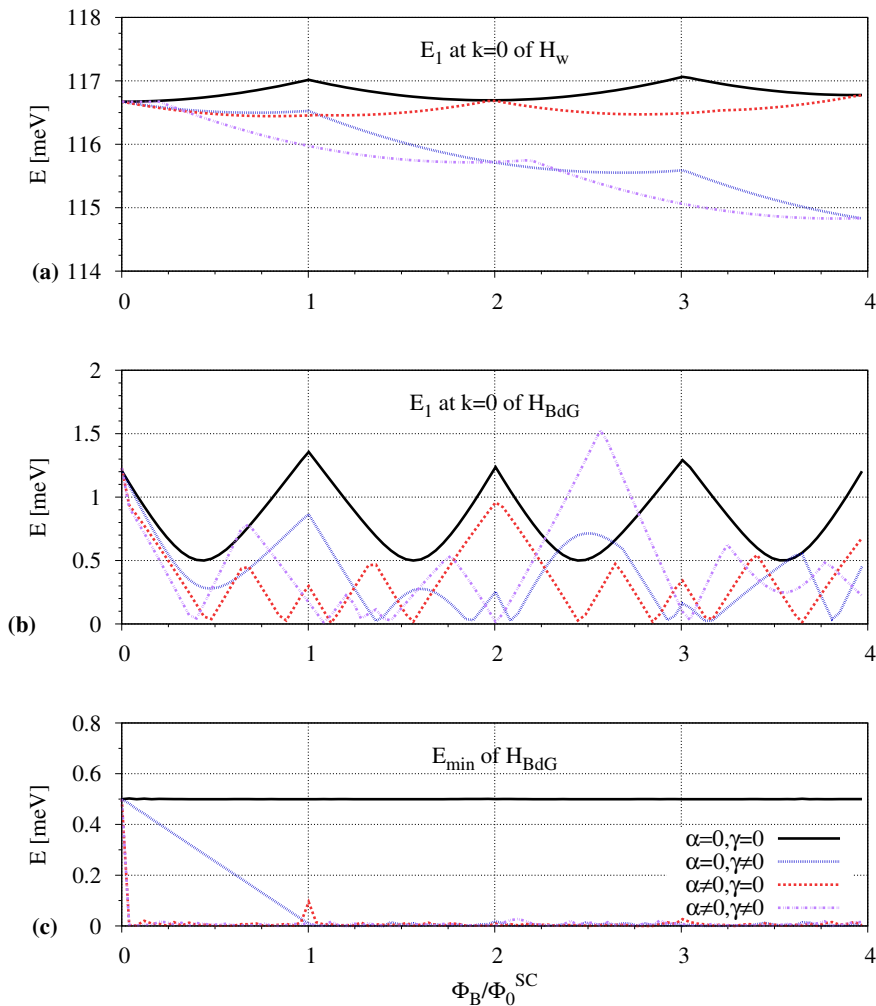
Figure 5.6: Flux-periodic oscillations of the lowest energy state, in terms of the magnetic flux Φ_B/Φ_0^{SC}, for the four cases of vanishing/non-vanishing Zeeman γ, and spin-orbit interaction α. **(a)** The normal conducting wire, both finite and infinite at $k = 0$. **(b)** Superconducting infinite wire at $k = 0$. **(c)** Superconducting infinite wire for all k, direct correspondence with the lowest energy state of the finite wire.

orbit interaction, the minimum gap is independent of the magnetic field strength, but rapidly closes if the spin-dependent interactions are included and the magnetic spin coupling overcomes the superconducting gap. The closing is linear in the case of the Zeeman interaction and happens at $k \neq 0$, which is also the case for the spin-orbit interaction but then the closing is abrupt. Incidentally, a small gap reopening and closing occurs around one and three flux quanta, in relation to the smallest amplitudes of the flux-periodic oscillations in Fig. 5.6(b). Irregularities of the minimum energy in Fig. 5.6(c) are due to small variations of the gap for differing values of the wavevector k.

5.3   Effects of polygonal cross-section geometry

We proceed by comparing with a hexagonal shell, and for a fair comparison, the minimal shell thickness is set equal to the cylindrical shell. In this way, the sides are of similar thickness to the cylindrical case, whilst the corner radius is slightly larger Fig. 5.7(a). The cylindrical coordinate system of the grid results in irregularities of the shell surface, which is practical with respect to the irregularities of fabricated samples. By introducing corners into the grid domain of the transverse Hamiltonian, Fig. 5.7(a), separation of the lowest energy levels is induced, Fig. 5.7(b) due to the corner localization [38, 46], which increases the difference in wave vectors $\vec{k} = \hbar^{-1}\vec{p}$, for adjacent energy levels at the given chemical potential. This results in an increased difference in momentum between the quasiparticle bands, Fig. 5.7(c), compared with the cylindrical case. In Fig. 5.7(d), a minor decrease of variance between the cases of vanishing/nonvanishing Zeeman and spin-orbit interaction can be seen. However, the systems in Fig. 5.5 and Fig. 5.7 are at slightly different values of magnetic field strength $|\vec{B}|$, as higher magnetic fields are needed for the same number of flux quanta due to the smaller area, A, of the hexagon, as seen from the definition of magnetic flux $\Phi_B = |\vec{B}|A$.

Compared with the cylindrical case, the flux-periodic oscillations of the normal conducting wire are nearly identical, Fig. 5.8(a). This is expected as the effective quantum wells formed by the corners, overlap in the sides [36, 228], so that the hexagon is not too different from the cylinder. More specifically, the angular momentum from the external magnetic field is not overpowered by the corner localization. Therefore the theory for cylindrical nanowires may often be in qualitative agreement with experimental results from hexagonal wires [220]. The oscillations of the BdG spectrum of the infinite wire at $k = 0$, Fig. 5.8(b,c), share the same features as the cylindrical case. A period of $h/2e$ is clearly obtained for vanishing Zeeman and spin-orbit interaction but the peak amplitudes are alternately equal.
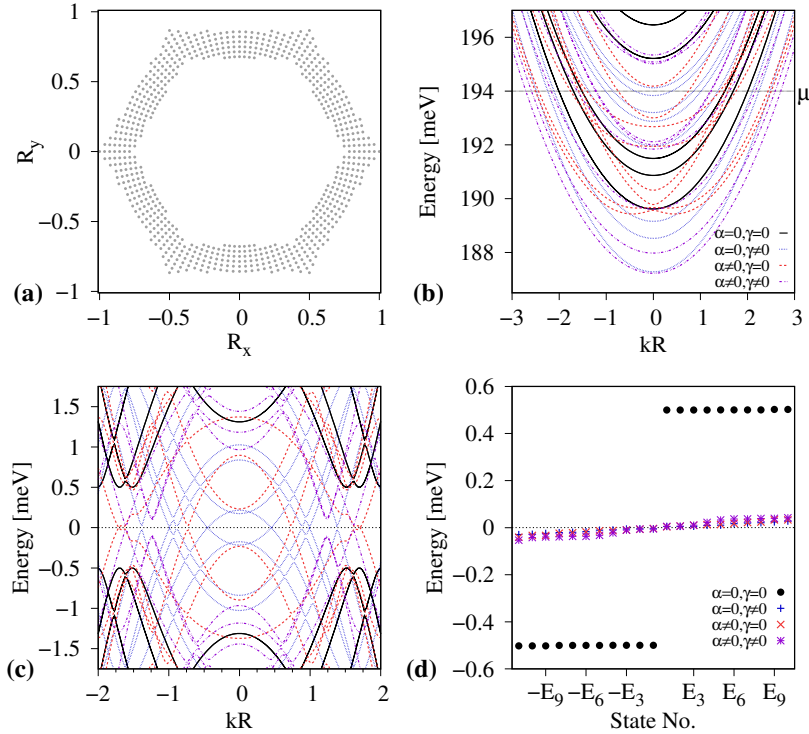
Figure 5.7: State of the nanowire system at magnetic field strength $|\mathbf{B}| = 1.56$ T. **(a)** Hexagonal nanowire cross section with units $R = 50$ nm. Minimal shell thickness of 10 nm. **(b)** Energy dispersion of the infinite wire nearby the chemical potential (μ), for the four cases of vanishing/non-vanishing Zeeman interaction (γ) and spin-orbit interaction (α). The dimensionless unit kR denotes the wavevector times radius. **(c)** Corresponding BdG quasiparticle energy dispersion for the infinite wire. **(d)** Finite wire BdG quasiparticle energy states.
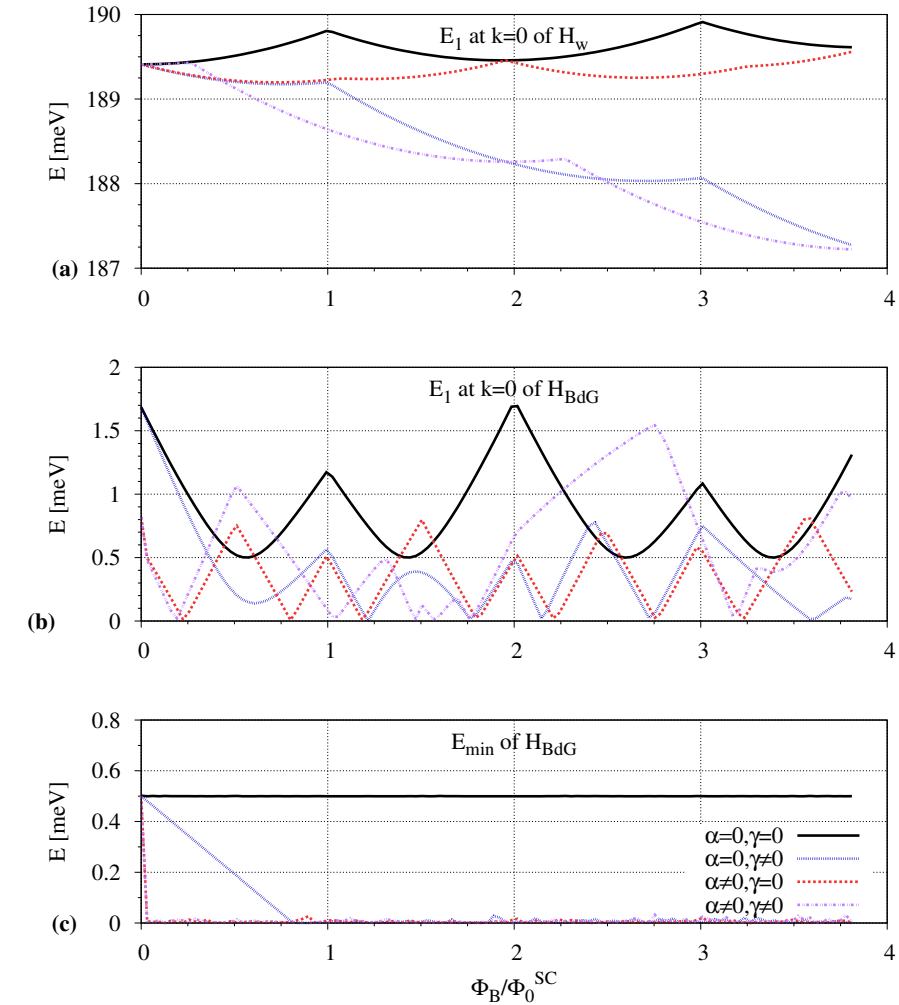
Figure 5.8: Flux-periodic oscillations of the lowest energy state for a hexagonal wire cross-section, in terms of the magnetic flux Φ_B/Φ_0^{SC}, for the four cases of vanishing/non-vanishing Zeeman γ, and spin-orbit interaction α. **(a)** The normal conducting wire, both finite and infinite at $k = 0$. **(b)** Superconducting infinite wire at $k = 0$. **(c)** Superconducting infinite wire for all k, direct correspondence with the lowest energy state of the finite wire.

The $h/2e$ periodicity is found to be highly dependent on the chemical potential. This applies as well to the cylindrical case, but explored here in more detail for the hexagonal cross-section, as it is a more realistic and common configuration of nanowire geometry. In Fig. 5.9, the periodicity in the case of vanishing Zeeman and spin-orbit interaction is shown for nine values of the chemical potential in integer steps. With increasing energy, the periodicity approximately alternates between periodicity of a normal and superconducting flux quantum.
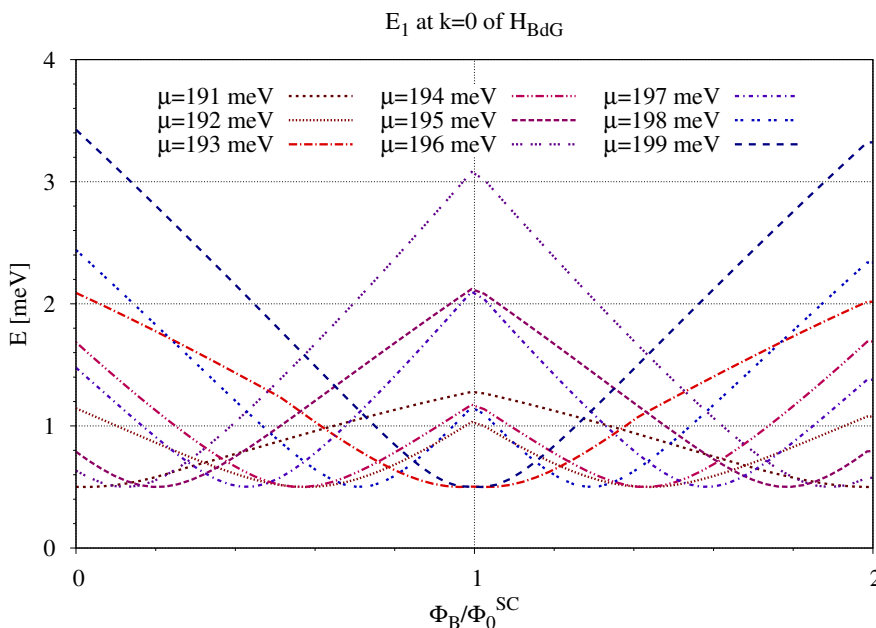
Figure 5.9: Varying period of flux-periodic oscillations of the lowest energy state of the infinite wire BdG spectra at $k = 0$ of the hexagonal nanowire, in the case of no spin-dependent interactions $\gamma = 0 = \alpha$.

Comparing with the flux-periodic oscillation of the normal conducting energy bands, Fig. 5.10, there is a correspondence with values of chemical potentials at crossings and h/e periodicity seen in Fig. 5.9. This is clearly seen at $\mu = 199$ meV for example, where the period minima corresponds to the crossing at one flux quantum in Fig. 5.10. Conversely, for $\mu = 191$ meV, the crossing is at zero and three flux quanta, leading to a period maxima at one flux quantum. As the chemical potential is shifted away from crossings, the sub-periods appear. At values exactly midway between crossings, where $\mu = 192$ meV comes close, the $h/2e$ periodicity is displayed.
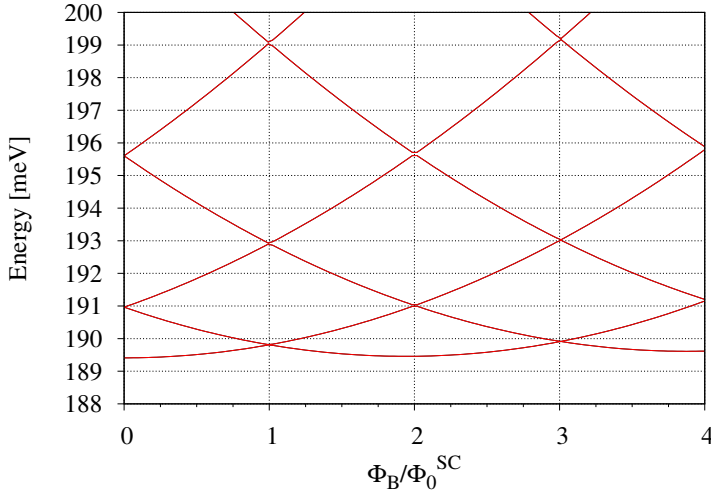
Figure 5.10: Oscillations of the infinite normal conducting hexagonal wire.

To specify the underlying interaction in the BdG spectra, we chose two chemical potential values and compare the corresponding flux-periodicity, Fig. 5.11(a). The BdG Hamiltonian essentially doubles the degrees of freedom, coupling electrons and holes of opposite spin by the gap parameter. The value of the chemical potential in the normal wire, Fig. 5.11(b) determines around which values of k the induced gap is situated. The key difference between the two cases is that in the case of the higher chemical potential, there is a crossing of the adjacent upper energy level in the BdG spectra, Fig. 5.11(c), such that the curvature of the second band at $k = 0$ is inverted with respect to the first one. As the magnetic field strength is increased to the value of half a flux quantum, this energy level meets the lowest one at the energy value 1.25 meV, Fig. 5.11(d). Further increasing the magnetic field strength, the two bands join and the lowest energy is overtaken in a sense so that the energy keeps lowering up to the value of one flux quantum, Fig. 5.11(e).
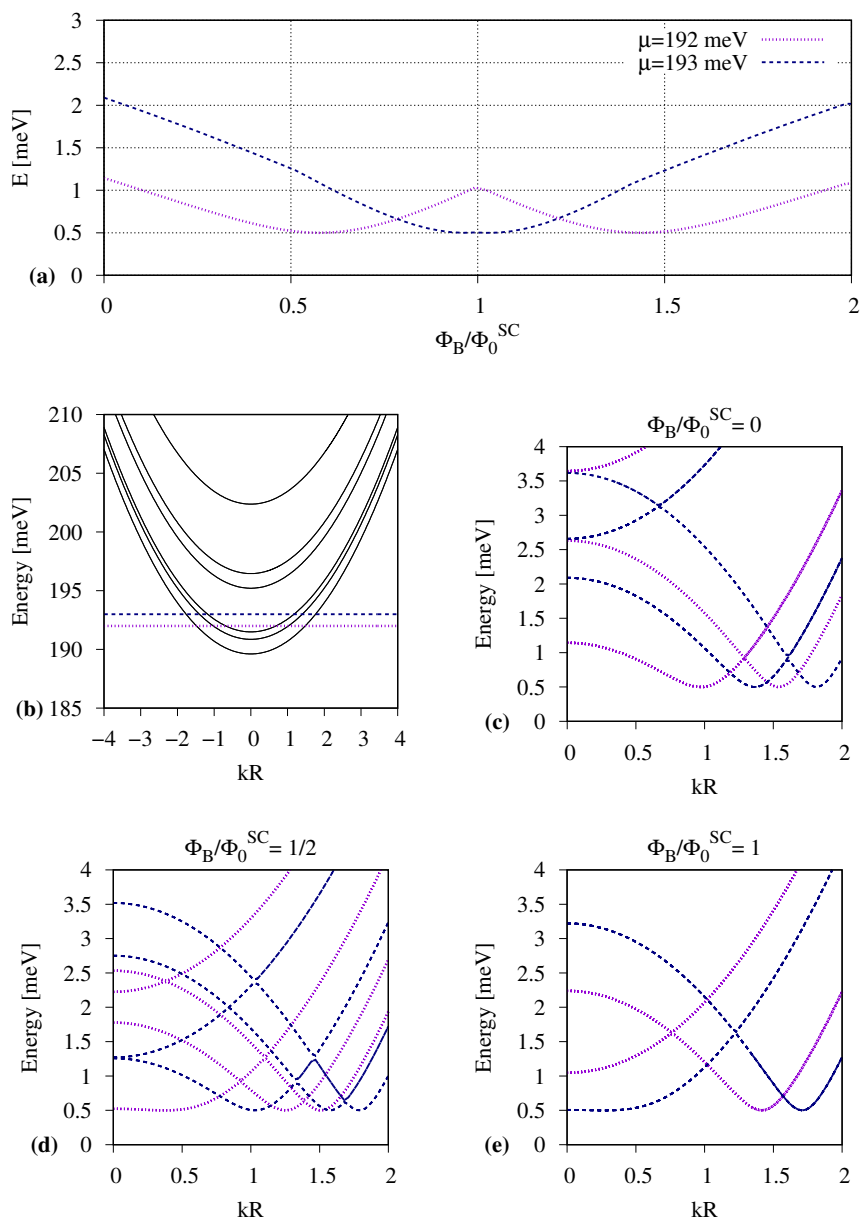
Figure 5.11: (a) BdG gap at $k = 0$ of the infinite wire for two values of the chemical potential. (b) Infinite wire dispersion. (c) BdG dispersion for magnetic fields strengths corresponding to zero superconducting flux quanta, (d) half a flux quantum, (e) one flux quantum.

To investigate effects of increased corner localization, a square cross-section is calculated, Fig. 5.12(a). The corner states form a near degenerate group that is still influenced by the orbital magnetic term, which manifests in splitting of the lowest energy states in the absence of both γ, α, Fig. 5.12(b). The corner geometry has the non-trivial effect [174] of enhancing the longitudinal component of the spin-orbit coupling, Eq. (5.17). As before, higher magnetic field strength is needed for an equal amount of flux quanta, due to the decreased area of the square cross-section. Most notably in the case of solely nonvanishing spin-orbit coupling, there is no gap closing at the given magnetic field strength, Fig. 5.12(c,d). The flux-periodic oscillations of
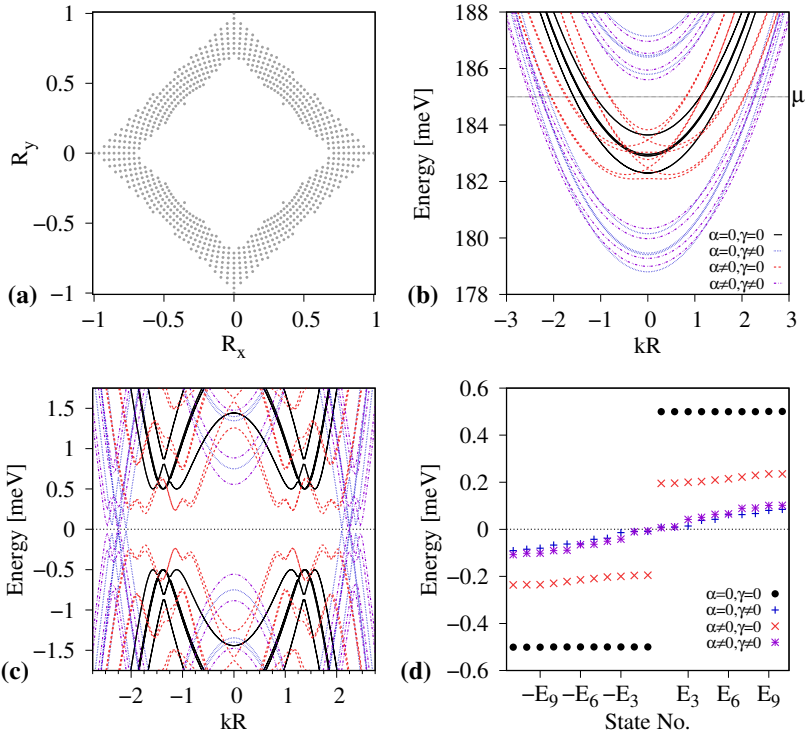
Figure 5.12: State of the nanowire system at magnetic field strength $|\mathbf{B}| = 2.32$ T. **(a)** Square nanowire cross section with units $R = 50$ nm. Minimal shell thickness of 10 nm. **(b)** Energy dispersion of the infinite wire nearby the chemical potential (μ), for the four cases of vanishing/non-vanishing Zeeman interaction (γ) and spin-orbit interaction (α). The dimensionless unit kR denotes the wavevector $k \, [\text{m}]^{-1}$ times radius $R[\text{m}]$. **(c)** Corresponding BdG quasiparticle energy dispersion for the infinite wire. **(d)** Finite wire BdG quasiparticle energy states.

the normal conducting wire on the other hand are nearly flattened out due to corner localization Fig. 5.13(a). Furthermore, there is very little indication of the superconducting flux quantum in Fig. 5.13(b). This is attributed to the large separation between the first groups of corner- and side-localized states, as this is the main variable between the cases. The oscillations of the minimum energy for all k in the infinite wire BdG spectra, Fig. 5.13(c) show alternating gap opening and closing with periodicity of the superconducting flux quantum. The induced magnetic field from the spin-orbit coupling opposes the external magnetic field, allowing for the gap opening.
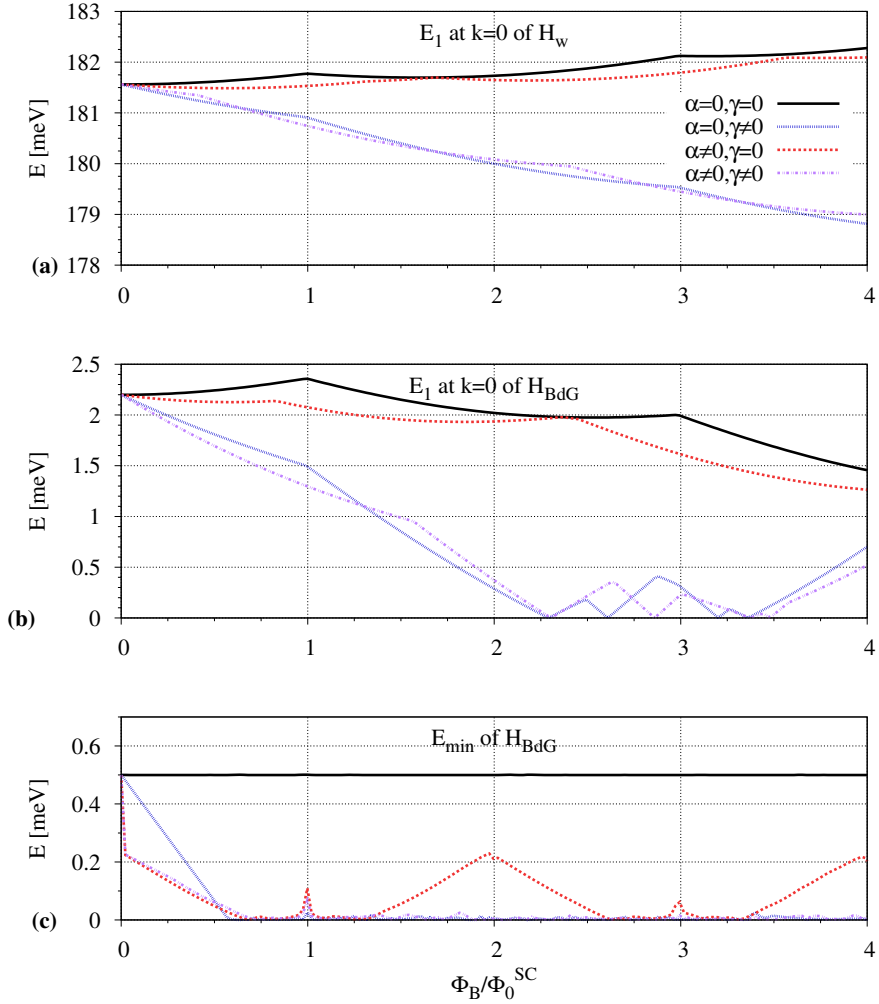
Figure 5.13: Flux-periodic oscillations of the lowest energy state for a square wire cross-section, in terms of the magnetic flux Φ_B/Φ_0^{SC}, for the four cases of vanishing/non-vanishing Zeeman γ, and spin-orbit interaction α. **(a)** The normal conducting wire, both finite and infinite at $k = 0$. **(b)** Superconducting infinite wire at $k = 0$. **(c)** Superconducting infinite wire for all k, direct correspondence with the lowest energy state of the finite wire.

5.4 Summary and conclusions

Flux-periodic oscillations in a core-shell nanowire system with varying geometry, are explored numerically. Magneto-oscillations of the lowest energy states of the Bogoliubov-de Gennes Hamiltonian (BdG) and its components are calculated for cylindrical, hexagonal and square cross-section geometries. For the former two cases, $h/2e$ periodicity is found for specific values of the chemical potential whilst the periodicity for the square wire is found to be strictly h/e. The superconducting parameter is constant throughout the calculation, with no phase dependency imposed. Zeeman and spin-orbit interaction are found to influence the flux periodicity considerably so that a periodicity of a fractional superconducting flux quantum is obtained at zero wavevector in the infinite wire BdG dispersion. The flux-periodicity arises from minimal coupling in the diagonal Hamiltonians of the BdG. The transition between the h/e and $h/2e$ periodicity is found to be dependent on the adjacent higher energy level with respect to the chemical potential.

92

Chapter 6

Stokes' Theorem for Bivector-valued Fields in Geometric Algebra

The algebra of Majorana operators, Eq. (1.31), can be considered as a part of a larger algebraic framework known as Clifford algebra [84], which underlies the anyonic statistics of Majorana zero modes [229]. In the past century, Clifford algebras have steadily gained popularity and found many applications across diverse fields of science in recent years [230, 231]. An attractive feature of Clifford algebras is that they unify and generalize various branches of mathematics commonly applied in physics [232, 233]. Importantly, Clifford algebras lie at the heart of the recently formulated periodic table of topological invariants [84, 161, 234], see Appendix A, applicable to topological insulators and topological superconductors [181, 183, 235]. Furthermore, within Clifford algebras, general operations of quantum computing and logic can be worked with [236–239]. A real valued formulation of Clifford algebras, known as geometric algebra, has proven to be a straight-forward and intuitive generalization of vector algebra with definite geometric interpretations [240] and clear relations to linear algebra [241, 242]. Geometric algebra can be further formulated to geometric calculus, in which the *boundary theorem* can be proven and from it, an n-dimensional generalization of the residue theorem obtained [243, 244]. The boundary theorem generalizes the fundamental theorems of scalar and vector calculus to infinite integer dimensions. It encompasses the generalized Stokes theorem written with differential forms along with its dual cases [245] and enables coordinate free integration [246]. Many properties of the algebra have been derived within other formalisms [243]. The main advantage of geometric algebra is accessibility and ease of visualization.

In this chapter, the boundary theorem for bivector fields is visualized using geometric calculus in order to gain physical insight into the monopole structure of the first Chern number topological invariant, Eq. (1.16). Interrelations to standard theorems of scalar and vector calculus, and their generalizations, are clarified.

6.1 The boundary theorem

The fundamental theorem of calculus relates the derivative of a function to its integral and is the crux of calculus,

$$\int_a^b f'(x)\,dx = f(b) - f(a), \tag{6.1}$$

where $f(x)$ is continuously differentiable real-valued function on the open interval (a,b). The theorem allows for ease of calculation of the integral of a function by simply evaluating its antiderivative at the end points. In vector calculus, the theorem has generalizations in two- and three-dimensional spaces using fields along with the vector differential operator ∇.

A vector field is said to be conservative if it can be written as the gradient of a function, $\mathbf{E} = \nabla\phi$, where ϕ is termed the scalar potential for $\mathbf{E}$. The gradient theorem states that an integral of a conservative field along a path equals the difference in the value of the potential field at the end points,

$$\int_a^b \nabla\phi \cdot d\boldsymbol{\ell} = \phi(b) - \phi(a). \tag{6.2}$$

Integration along a closed path C in this case equals zero,

$$\oint_C \nabla\phi = 0. \tag{6.3}$$

Furthermore, every conservative field is irrotational, as the curl vanishes according to

$$\nabla \times \mathbf{E} = \nabla \times (\nabla\phi) = 0. \tag{6.4}$$

The converse is only true if there are no holes in the space, a theorem known as Poincaré's lemma [79, 247], showing the link to topology. By considering subsets of space with parts removed, non-conservative irrotational fields can be formulated. This study further leads to the mathematics of de Rham cohomology [79].

A vector field is said to be solenoidal if it can be written as the curl of another vector field, $\mathbf{B} = \nabla \times \mathbf{A}$, where $\mathbf{A}$ is termed the vector potential for $\mathbf{B}$. In the same way that the integral of the differentiated potential in Eq. (6.2) was given by its value at the boundary, Green's curl theorem states that integration along a closed path forming the boundary of a surface, $C = \partial S$, is non-zero and given by the total curl (circulation density) on the surface,

$$\iint_S \nabla \times \mathbf{A} \cdot d\mathbf{S} = \oint_{\partial S} \mathbf{A} \cdot d\boldsymbol{\ell}. \tag{6.5}$$

Furthermore, every solenoidal field is incompressible, without sources/sinks, as the divergence vanishes according to

$$\nabla \cdot \mathbf{B} = \nabla \cdot (\nabla \times \mathbf{A}) = 0. \tag{6.6}$$

Any smooth vector field $\mathbf{F}$ (vanishing at infinity) in $\mathbb{R}^3$ can be written as the sum of an irrotational and a solenoidal field via Helmholtz decomposition [248–250]

$$\mathbf{F} = \mathbf{E} + \mathbf{B} = \nabla\phi + \nabla \times \mathbf{A}. \tag{6.7}$$

Although the divergence of the solenoidal component vanishes, the divergence of the irrotational component does not, and is given by the Laplacian of the scalar potential,

$$\nabla \cdot \mathbf{E} = \nabla \cdot (\nabla\phi) = \nabla^2\phi. \tag{6.8}$$

The divergence theorem equates the volume integration of this expression to the flux of the field $\mathbf{E}$ through a surface $S = \partial V$, containing the sources/sinks of $\mathbf{E}$,

$$\iiint_V \nabla \cdot \mathbf{E} \, dV = \oiint_{\partial V} \mathbf{E} \cdot d\mathbf{S}. \tag{6.9}$$

Utilization of the above theorems is foundational to electromagnetism and therefore notation has been chosen such that results from electro- and magnetostatics can be recognized. The theorems from Eqs. (6.2),(6.5),(6.9) can be combined and generalized to n-dimensions, $n \in \mathbb{N}$, using differential forms along with the exterior derivative [232, 245, 251].

Let ω be a differential k-form defined on the smooth oriented manifold M of dimension $k + 1$ with $d\omega$ denoting the $(k + 1)$-form valued exterior derivative. The generalized Stokes theorem is the integral relation

$$\int_M d\omega = \oint_{\partial M} \omega. \tag{6.10}$$

This Stokes theorem of forms is central to cohomology and multiple other aspects of algebraic topology [252]. The theorem holds not only for smooth manifolds, but also for $k-$chains (triangulations of M) and even non-smooth chains (fractals) [253]. From the perspective of geometric algebra however, Stokes's theorem of forms only contains half of the information content of the boundary theorem in geometric calculus [232]. The other half is the duality, which is unified by the geometric product from which the multivector gradient can be defined.

Multiplication of vectors in geometric algebra is defined by the geometric product

$$\mathbf{ab} = \mathbf{a} \cdot \mathbf{b} + \mathbf{a} \wedge \mathbf{b}. \tag{6.11}$$

The center dot denotes the same symmetric inner product as in standard vector algebra whilst the operator $\wedge$, termed *wedge*, denotes the anti-symmetric outer product also known as the wedge product. The outer product is a generalization of the cross product to n-dimensions yet still not equal to the cross product in three dimensions, but dual to it. For two orthogonal vectors $\vec{a}$ and $\vec{b}$, the cross product $\vec{a} \times \vec{b} = \vec{c}$ is a third vector, with magnitude and direction, orthogonal to both $\vec{a}$ and $\vec{b}$. The wedge product $\vec{a} \wedge \vec{b} = \check{\mathbf{c}}$ is however a two-dimensional bivector lying in the plane spanned by $\vec{a}$ and $\vec{b}$, having magnitude and area, Fig. 6.1.
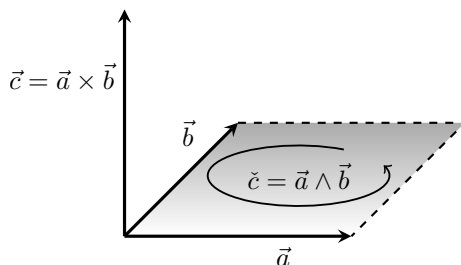
Figure 6.1: The vectors $\vec{a}$ and $\vec{b}$ span the plane of the bivector $\check{\mathbf{c}}$. The vector $\vec{c}$ is orthogonal to the plane and in three-dimensional space only, dual to the bivector.

Using the outer product, higher-dimensional vectors can be defined such as three-dimensional trivectors $\tilde{d} = \vec{a} \wedge \vec{b} \wedge \vec{c}$, four-dimensional quadvectors and in general n-vectors (termed blades in Clifford algebra) which form the building blocks of geometric algebra. Blades of different dimensions can be added resulting in linear combinations termed multivectors, which can fairly be said to generalize the concept of number to higher dimensions [234]. Whilst the outer product is dimension-raising, the inner product is dimension-reducing as in general the inner product between an n-vector and m-vector is an l-vector of dimension $l = n - m$ for $n \geq m$.

Any n-vector $\mathbf{v}$ determines an n-dimensional vector space $\mathcal{V}_n$ of all vectors $\mathbf{x}$ satisfying $\mathbf{x} \wedge \mathbf{v} = 0$. Addition and multiplication of vectors in $\mathcal{V}_n$ results in a 2^n-dimensional linear space closed under the geometric product, the geometric algebra $\mathbb{G}_n$. Since an n-vector in n-dimensional space does not have degrees of freedom for orientation, other that up to a sign, such an element becomes a pseudoscalar [243]. As an example, the complex number i is a unit bivector which becomes a pseudoscalar in the 2D plane. Complex numbers can be understood as the even part of $\mathbb{G}_2$ geometric algebra [254]. The binomial expansion of geometric algebra $\mathbb{G}_n$ with unit vectors $e_n^2 = 1$ for $n = 0, 1, 2, 3, 4$ is shown in Fig. 6.2 along with the relations of its even components to the division algebras of complex numbers, quaternions and octonions $\mathbb{C}, \mathbb{H}$ and $\mathbb{O}$ respectively. The division algebras have been shown to form a basis for all compact symmetric spaces [255]. $\mathbb{G}_0$ is the algebra of the real numbers $\mathbb{R}$,

the only other division algebra. In $\mathbb{G}_1$, vectors are pseudoscalars and so the geometric algebra is essentially the algebra of the real number line, $\mathbb{R}^1$. For the plane, $\mathbb{G}_2$ consists of scalars, two orthogonal vectors and a pseudoscalar bivector. $\mathbb{G}_3$ consists of scalars, three orthogonal vectors, three orthogonal bivectors and a pseudoscalar trivector. $\mathbb{G}_4$ consists of scalars, four orthogonal vectors, six orthogonal bivectors, four trivectors and a pseudoscalar quadvector.

$$
\begin{array}{cccccccccc}
\mathbb{G}_0: & & & & & 1 & & & & \\
\mathbb{G}_1: & & & & 1 & & 1 & & & \\
\mathbb{C} \in \mathbb{G}_2: & & & ① & & 2 & & ① & & \\
\mathbb{H} \in \mathbb{G}_3: & & ① & & 3 & & ③ & & 1 & \\
\mathbb{O} \in \mathbb{G}_4: & ① & & 4 & & ⑥ & & 4 & & ① \\
\end{array}
$$

Figure 6.2: Binomial expansion of geometric algebra, showing the hypercomplex division algebras as the even components (circled) in each dimension.

The multivector gradient operator $\boldsymbol{\nabla}$ for a differentiable multivector field F with an orthonormal basis $\mathbf{e}_i$ on a set M in $\mathbb{R}^n$ can be defined by the following expression, using the shorthand notation $\partial_i = \frac{\partial}{\partial_i}$,

$$
\boldsymbol{\nabla}F = \mathbf{e}_i \partial_i F = \mathbf{e}_1 \partial_1 F + \mathbf{e}_2 \partial_2 F + ... + \mathbf{e}_n \partial_n F. \tag{6.12}
$$

Considering that the operator $\boldsymbol{\nabla} = \mathbf{e}_i \partial_i$ functions as a vector algebraically, the multivector gradient can be factored into two components using the geometric product from Eq. (6.11), which applies equally for the product of a vector and multivector [244]. Therefore

$$
\boldsymbol{\nabla}F = \boldsymbol{\nabla} \cdot F + \boldsymbol{\nabla} \wedge F, \tag{6.13}
$$

where $\boldsymbol{\nabla} \cdot F$ is the divergence and $\boldsymbol{\nabla} \wedge F$ is the generalized curl. Let M be a smooth n-dimensional oriented manifold with a piece-wise smooth boundary ∂M of integer dimension $n-1$ where $n \geq 1$. By defining a directed element of the manifold M as a differential n-vector $d\mathbf{x}^n$, and similarly $d\mathbf{x}^{n-1}$ for ∂M, the boundary theorem of geometric calculus [243, 256] can be written as

$$
\int_M d\mathbf{x}^n \, \boldsymbol{\nabla}F = \oint_{\partial M} d\mathbf{x}^{n-1} \, F \, . \tag{6.14}
$$

Intuitively, this means that the total change in field F within a space M, equals the state of F at the boundary of the space, which can be seen as an expression of the conservation of information. Using the gradient decomposition from Eq. (6.13) along

with the geometric product, the boundary theorem can be split [232] into generalized curl and divergence components respectively,

$$\int_M d\mathbf{x}^n \cdot (\boldsymbol{\nabla} \wedge F) = \oint_{\partial M} d\mathbf{x}^{n-1} \cdot F \qquad (6.15)$$

and

$$\int_M d\mathbf{x}^n \wedge (\boldsymbol{\nabla} \cdot F) = \oint_{\partial M} d\mathbf{x}^{n-1} \wedge F. \qquad (6.16)$$

The former component, Eq. (6.15), can be considered analogous to the generalized Stokes theorem for differential forms with $\omega = d\mathbf{x}^{n-1} \cdot F$ and $d\omega = d\mathbf{x}^n \cdot (\boldsymbol{\nabla} \wedge F)$, and will from here on out be referred to as the outer part, due to the outer product of the gradient operator with the field F. The second component, Eq. (6.16), is the orthogonal duality counterpart which completes the theorem and will be referred to as the inner part [232].

6.2   Visualizing the Boundary theorem

In order to cover every case of interest, the instances for $n = 1, 2, 3$ will be explored where the multivector field F is of single grade and $\dim(F) = \dim(M) - 1 = dim(\partial M)$. The graphical representation is defined in a standard manner, denoting scalars with dots, vectors with oriented lines, bivectors with oriented planes, trivectors with oriented volumes and so forth. In Fig. 6.3, a graphical representation of the outer part of the boundary theorem on a one-dimensional manifold is presented, which is essentially the fundamental theorem of calculus, Eq. (6.1) or the gradient theorem for simple path, Eq. (6.2). The fundamental theorem intuitively tells us that a difference in scalar values at the boundary of a line will result in a unidirectional flow between them, and vice versa. The scalar gradient is denoted with points of unequal magnitude at the boundary. The more classical graphical representation is denoting the scalar magnitude difference by a slope, but this simplified representation carries nicely on to higher-dimensional cases.
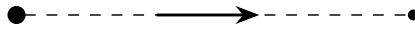
Figure 6.3: Graphical representation of the outer part of the boundary theorem for the case of $dim(F) = dim(\partial M) = 0$.

For the case of a one-dimensional manifold the inner part is zero since if the field F is scalar valued then $\boldsymbol{\nabla} \cdot F = 0$. Adhering to the dimension reducing property of the inner product results in $dim(\nabla \cdot F) = -1$, negative-dimensional fields are undefined but may have little explored relations to fractal dimensions [257, 258].

For a two-dimensional manifold, the outer part takes on the familiar form of Green's curl theorem, Eq. (6.5), using that the curl is dual to the outer product

$$\boldsymbol{\nabla} \wedge F = I \, \boldsymbol{\nabla} \times F, \tag{6.17}$$

where $I = \mathbf{e}_1 \wedge \mathbf{e}_2 \wedge \mathbf{e}_3$ is the $\mathbb{G}_3$ pseudoscalar, along with $d\mathbf{x}^2 = i|dS| = I\mathbf{e}_3|dS| = I\hat{\mathbf{n}}|dS|$. In essence, a bivector induces rotation along a closed boundary containing it, Fig. 6.4.
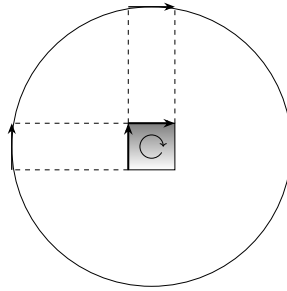
Figure 6.4: Outer part of the boundary theorem for $dim(M) = 2$. A non-zero rotation along the one-dimensional boundary ∂M results from the bivector $\boldsymbol{\nabla} \wedge \boldsymbol{F}$ within M, and vice versa. Orientation is determined by the sign.

Pleasingly, the inner part of the boundary theorem for $dim(M) = 2$ and $dim(F) = 1$, describes a two-dimensional divergence theorem, Fig. 6.5. Normally, the divergence is highlighted with more radial rays graphically, but takes on the suggested form here, by adhering to the lowest number of elements needed to span M.
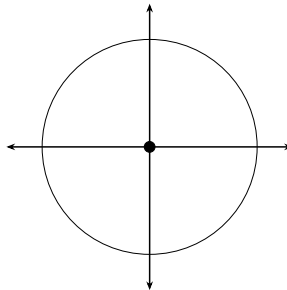
Figure 6.5: The divergence theorem in two dimensions, the inner part of the boundary theorem for $dim(M) = 2$. A non-zero flux, outward (inward), perpendicular to the one-dimensional boundary ∂M stems from the scalar divergence (convergence).

For the three-dimensional cases, $dim(M) = 3$, the divergence theorem, Eq. (6.9) is not recovered, but rather its dual, Fig. 6.6. In general, the dual of an n-vector is an m-vector such that $n + m = dim(M)$. The trivector $\nabla \wedge F$ within M is dual to a divergence scalar in $\mathbb{G}_3$. The tangent bivector field on the two-dimensional boundary is dual to a radially divergent vector field, normally considered in the three-dimensional divergence theorem. This suggests an interpretation of the effect of a trivector on a two-dimensional surface containing it. A trivector induces vorticity at every point on a closed boundary of a volume containing it, Fig. 6.6. The bivectors of $\mathbb{G}_3$ are dual to the Pauli vectors [256] and span the SU(2) Lie group, $SU(2) = \text{span}\{I\sigma_1, I\sigma_2, I\sigma_3\}$.
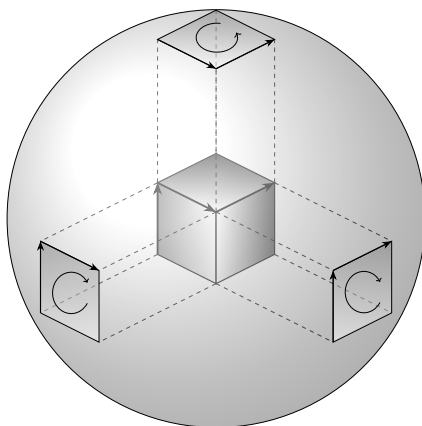
Figure 6.6: Outer part of the boundary theorem for $dim(M) = 3$. The pseudoscalar number of trivector valued $\nabla \wedge F$ equals the sum of the tangent bivector field on the boundary.

Reiterating, it is a special case in three dimensions that bivectors are dual to a vectors. In four dimensions, bivectors are self-dual. Since orthogonal bivectors are linearly dependent in three dimensions, the inner part of the boundary theorem for bivector valued fields is zero in three dimensions. The inner part becomes non-zero in a minimum of four dimensions. The structure is three-dimensional but requires the manifold M to be embedded in a higher-dimensional one, Fig. 6.7. This property along with the geometrical shape and genus is shared with the Clifford torus [259–261]. Rigorously proving the equivalence of this bivector field solution of the boundary theorem to the Clifford torus is beyond the present scope.

It is possible to visualize the cases continuing upward in dimensions. The trivector of the outer part in three dimensions becomes a quadvector in four dimensions, which can be visualized by a tesseract. The tesseract has eight trivectors as its boundary. According to the boundary theorem, a quadvector induces a trivector parallel to
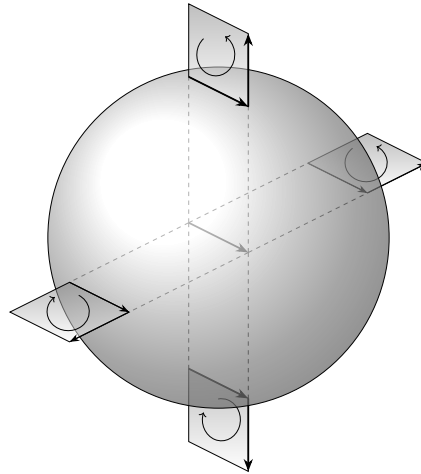
Figure 6.7: A bivector field F in $\mathbb{R}^4$, orthogonal to the two-dimensional boundary, induced by the divergence scalar $\boldsymbol{\nabla} \cdot F$.

every point of a volume, which is the boundary of a hypervolume containing the quadvector. The inner part becomes simpler for $dim(F) = 3$, the bivector $\boldsymbol{\nabla} \cdot F$ induces trivectors perpendicular to every point on a three-dimensional boundary of a hypervolume containing it. As human eyes see three-dimensional space, in which trivectors are pseudoscalars, directionality of trivectors is foreign to us but can be understood in analogy to the lower-dimensional cases.

6.3 Dualities

As noted in the previous section, the dual of an *n*-vector is an *m*-vector such that $n + m = dim(M)$. With this in mind the dualities of the considered cases of the boundary theorem can be explored. In one dimension, scalars and vectors are dual so the dual of Fig. 6.3 is a divergence of sorts, where a scalar within the manifold equals vectors orthogonal to the zero-dimensional boundary. In two dimensions the outer part in Fig. 6.4 and inner part in Fig. 6.5 are dual, highlighting the duality of rotation and divergence of vector fields in two dimensions.

In three dimensions, the outer part shown in Fig. 6.6 is dual to the three-dimensional divergence theorem, Eq. (6.9). From the viewpoint of geometric algebra, it is the generalization of the curl theorem, Eq. (6.5) rather than the divergence theorem. The dual of the inner part in three dimensions is a known curl theorem variant,

$$\iiint_V \boldsymbol{\nabla} \times \mathbf{F}\, dV = -\oiint_S \mathbf{F} \times \hat{\mathbf{N}}\, d\boldsymbol{S}\,.$$

However, as the 3D inner part is zero unless the manifold M is embedded within a higher-dimensional one, it is more suitable to consider its dual within 4D space. In four dimensions, bivectors are self dual and vectors are dual to trivectors. In that case, the duality is the outer part in three dimensions, Fig. 6.6. Note, that if embedded in four dimensions, trivectors will be dual to vectors. Therefore, phenomena described by scalars in space and vectors in spacetime, may be better understood as trivectors.

6.4 Projections

The boundary theorem cases in dimension N, are orthogonal projections of cases in the adjacent lower dimension, $N-1$. Therefore, the fundamental theorem of calculus in Fig. 6.3 can be seen as an orthogonal projection of Green's curl theorem, Fig. 6.4. Continuing upwards in dimensions, Green's curl theorem can be seen as a single side projection of the trivector in Fig. 6.6. Surprisingly, the two dimensional divergence theorem in Fig. 6.5 can be seen as a "front view" of the torus in Fig. 6.7. This projection relation, by definition of the boundary theorem, holds true in all dimensions even though pictorial representations on two-dimensional paper break down.

In general, elements of $\mathbb{G}_n$ can be decomposed into components within and orthogonal to the vector space, so that orthogonal projections and rejections can be written in terms of the geometric product using the pseudoscalar [243].

6.5 Discussion

Having uncovered two unfamiliar cases of Stokes' boundary theorem, Figs. 6.6 and 6.7, it is natural to consider whether a physical example of these structures exists in nature. Fig. 6.8(a) shows the dynamics of a toroidal vortex ring, as sketched by Tait and published in 1876, in the context of atomic theory [262].
Comparison with Fig. 6.7 shows graphical equivalence. To uncover mathematical equivalence, the vorticity field in fluid dynamics has to be considered in its dual form, as a bivector field [263]. The same dynamic structure can be found if the magnetic vector potential of a current carrying element is considered, from the well-known ring magnetic field induced by it, Fig. 6.8(b). In both cases, a closed link in the axial field (magnetic/vorticity) of $U(1)$ symmetry is dual to a spin-formation of non-trivial topology in the surrounding medium, hinting at richer internal degrees of freedom [264].

Interestingly, the only natural phenomena that seems to fit directly to Fig. 6.6 also comes from electromagnetism, though indirectly. Considering that $I\mathbf{B} = \nabla \wedge \mathbf{A}$, one can see that the magnetic vector potential of a magnetic monopole, is essentially the bivector field configuration of Fig. 6.6. Since $\nabla \wedge \nabla \wedge \mathbf{A} = 0$, this indicates that a magnetic monopole should be represented by a trivector, with a bivector potential. It also becomes evident that a magnetic monopole necessitates a radially divergent
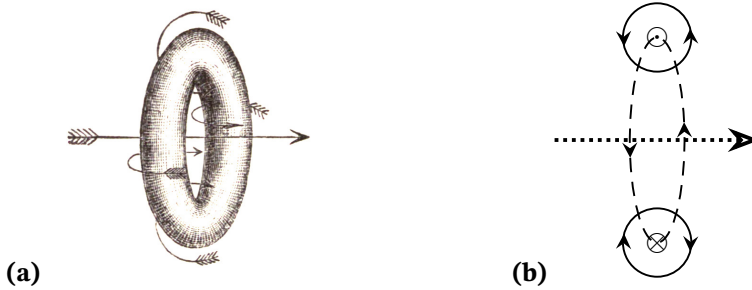
Figure 6.8: (a) Sketch of a toroidal vortex of a smoke ring [262]. (b) Magnetic field (dashed) and magnetic vector potential (solid) around a line current element (dotted). The curl of the magnetic vector potential has the same ring symmetry as the magnetic field, but is shown in a cross-section.

spin structure. Although we arrive at this conclusion from purely geometric conditions, this can be shown mathematically as well [265–267]. This applies equally to the monopole configuration of the Berry curvature, Eq. (1.16), emerging near degeneracies in parameter space of Hamiltonians [68, 70] and implies that the first Chern number [76] is a pseudoscalar trivector in that case. Considering the first Chern number in Eq. (1.17) as a trivector gives a clear picture of why the Berry phase, Eq. (1.11), is non-zero for all closed loop paths on a boundary of a surface containing the monopole. It furthermore shows how the $SU(2)$ gauge structure is necessitated in this case, Eq. (1.21), as the three bivector planes spanning the trivector are generators of SU(2).

Wide applicability of the Figs. 6.6 and 6.7 can be expected. The Pauli matrices form an algebra isomorphic to $\mathbb{G}_3$ and the Dirac matrices are a matrix representation of the Dirac algebra $Cl_{1,3}(\mathbb{C})$, both have geometric interpretations within space-time algebra [256] ($Cl_{1,3}(\mathbb{R})$), which in embedded in $\mathbb{G}_4$. Bott periodicity, key to the periodic table of topological insulators and superconductors [84], has been shown to have roots in the Octonion division algebra [268] which has multiple representations in geometric algebra [269]. Every Lie algebra has been shown to have a representation as a bivector algebra [270]. This opens up the possibility for visualizing interactions with Lie spin group symmetries such as spin dynamics, electroweak interactions and Berry connections. Problems in cohomotopy arise naturally from such considerations and in the same manner that differential forms have be used in algebraic topology to describe cohomology [252], geometric calculus can be expected to be equally applicable. For example, Fig. 6.7, can be considered as a projection of $SU(2)$ onto S^2, and since $SU(2)$ is diffeomorphic to S^3, there is a direct link to the Hopf map [79].

In closing, seeing that the boundary theorem within geometric calculus can be applied to bivector valued fields, which are anti-commutative (non-Abelian), the ques-

tion arises how it is related to the non-Abelian Stokes theorem in the standard literature [271–277]. In particular, how directed integration theory [243] relates to ordered integrals.

6.6   Conclusions

Using geometric algebra, main cases of interest of the generalized Stokes' theorem have been visualized and the relations to the standard theorems of vector calculus clarified. From considering bivector valued fields in three and four dimensions, little explored instances of the theorem emerge which are found to have natural manifestations of non-trivial topology. Their dualities and projection relations have been examined. The diagrams presented may serve in aiding visualization of interactions with spin group symmetry and provide insight into the structure of topological invariants.

Chapter 7

Summary and Conclusions

Majorana zero modes are quasiparticle excitations theorized to be suitable for fault-tolerant quantum computation and memory. Their key advantageous property is topological protection, resulting in tolerance for environmental perturbations, which is one of the main obstacles towards scaling up of quantum computers due to phase decoherence of non-topological qubits. Implementing numerical and analytical methods, the low-energy physics of Majorana zero modes and dependent interactions are explored in core-shell nanowires with polygonal geometry, which can effectively host multiple one-dimensional wires, one for each corner. By diagonalization of the composite Bogoliubov-de Gennes Hamiltonian for a three-dimensional tubular lattice, suitability for hosting and manipulating Majorana zero modes in proximitized core-shell nanowires is investigated. In structures combining a triangular wire with a hexagonal core, the energy gap separating the lowest energy corner-localized states and the adjacent energy levels, is found to be significantly increased. This is favorable for the stability of Majorana Modes in such a system, as they are formed from the lowest energy states, and their localization corresponds with the corner localization, which also holds for polarization of the wavefunction by a transverse electric field.

Propagation of proximity-induced superconductivity via electron-hole coherence is studied by separately implementing radial, angular and longitudinal step-functions in the gap parameter of the shell. Varying compatibility with Andreev reflection, a mechanism commonly applied to explain the proximity effect, is found and described for each of the cases. A weaker superconducting gap parameter in a half lengthwise proximitized nanowire is shown to increase the coherence length, although the total gap of the system is decreased. Flux-periodic oscillations of the lowest energy states of a fully proximitized shell are analyzed, for both the composite Hamiltonian and its elements. For a fixed superconducting gap parameter, flux periodicity of both normal and superconducting flux quanta is found for the infinite wire spectrum at zero wave vector, and shown to be dependent on interactions with adjacent energy levels and

therefore corner localization in the case of polygonal cross-section geometry.

To gain insight into the structure of topological invariants in physical systems, in particular the monopole configuration of the Berry curvature for degenerate energy levels, Stokes' theorem for bivector fields is visualized using geometric calculus, a real-valued formulation of Clifford analysis. The topological scalar invariant is shown to be dual to a trivector, satisfying a generalized divergence theorem.

In conclusion, although prismatic core-shell nanowires are feasible for hosting and manipulating multiple Majorana wires, it is found that each of the physical properties necessary for their emergence, spin-orbit and Zeeman interaction along with proximity-induced superconductivity, involves non-trivial interactions that ideally require specific modeling on their own. Furthermore, these properties are found to be interdependent. For instance, whilst the cross-sectional geometry influences localization, it also influences the spin-orbit coupling, arising from the charge imbalance over the core and shell interface. Both the electron-hole coherence and flux-periodicity are notably varied in the presence of strong Zeeman splitting, which is not included in effective models derived to describe these phenomena separately.

With recent experiments, it has become clear that material-dependent properties such as sample disorder and interface roughness can significantly alter the conditions for which Majorana zero modes can be realized and definite signatures of their existence probed. In light of the importance of fabrication specifics, future work in the field will need to involve close cooperation between experiments and modeling, where significant elements of each considered experimental setup are modeled in detail, both separately and in conjunction. The methodology in this work can be improved by modeling transport through the nanowire system, incorporating leads and their material properties, to ease comparison with measurements.

Majorana zero modes in nanowires are part of a larger ongoing endeavor, where analogues of complex phenomena in particle physics are engineered using condensed matter systems. The common theme in most interactions considered herein is the coupling, interaction and long-range coherence of the spin degree of freedom. Just as the last century was the age of charge, bringing about many beneficial technologies in the form of electronics, the current information age is that of spin. Arguably, more pressing problems currently exist in the energy sector rather than the information sector. However, since the pursuit of topological quantum computation involves multiple components of physics being implemented at the forefront of material science, given the progression of earlier scientific discoveries, unforeseeable benefits to other fields can be expected in the long run.

References

[1] R. M. Lutchyn, E. P. A. M. Bakkers, L. P. Kouwenhoven, P. Krogstrup, C. M. Marcus, and Y. Oreg, "Majorana zero modes in superconductor-semiconductor heterostructures," *Nature Reviews Materials*, vol. 3, p. 52–68, May 2018.

[2] C. Schrade and L. Fu, "Majorana superconducting qubit," *Phys. Rev. Lett.*, vol. 121, p. 267002, Dec 2018.

[3] B. Field and T. Simula, "Introduction to topological quantum computation with non-Abelian anyons," *Quantum Science and Technology*, vol. 3, no. 4, p. 045004, Oct 2018.

[4] A. Manolescu, A. Sitek, J. Osca, L. Serra, V. Gudmundsson, and T. D. Stanescu, "Majorana states in prismatic core-shell nanowires," *Phys. Rev. B*, vol. 96, p. 125435, Sep 2017.

[5] T. D. Stanescu, A. Sitek, and A. Manolescu, "Robust topological phase in proximitized core–shell nanowires coupled to multiple superconductors," *Beilstein Journal of Nanotechnology*, vol. 9, p. 1512–1526, 2018.

[6] E. Majorana, "Teoria simmetrica dell'elettrone e del positrone." *Il Nuovo Cimento*, vol. 12, no. 1924-1942, p. 171, 1937.

[7] F. T. Avignone, S. R. Elliott, and J. Engel, "Double beta decay, Majorana neutrinos, and neutrino mass," *Rev. Mod. Phys.*, vol. 80, p. 481–516, Apr 2008.

[8] T. D. Stanescu, *Introduction to Topological Quantum Matter & Quantum Computation*. CRC Press: London., 2017.

[9] J. Alicea, "New directions in the pursuit of Majorana fermions in solid state systems," *Reports on Progress in Physics*, vol. 75, no. 7, p. 076501, jun 2012.

[10] S. Das Sarma, M. Freedman, and C. Nayak, "Majorana zero modes and topological quantum computation," *npj Quantum Information*, vol. 1, 01 2015.

[11]   P. Bonderson and C. Nayak, "Quasi-topological phases of matter and topological protection," *Phys. Rev. B*, vol. 87, p. 195451, May 2013.

[12]   P. Schüffelgen, T. Schmitt, M. Schleenvoigt, D. Rosenbach, P. Perla, A. R. Jalil, G. Mussler, M. Lepsa, T. Schäpers, and D. Grützmacher, "Exploiting topological matter for Majorana physics and devices," *Solid-State Electronics*, vol. 155, pp. 99–104, 2019, selected Papers from the Future Trends in Microelectronics (FTM-2018) Workshop. [Online]. Available: http://www.sciencedirect.com/science/article/pii/S0038110118305896

[13]   R. Aguado, "Majorana quasiparticles in condensed matter," *La Rivista del Nuovo Cimento*, p. 523–593, 2017.

[14]   C. Beenakker, "Search for Majorana fermions in superconductors," *Annual Review of Condensed Matter Physics*, vol. 4, 2013.

[15]   A. Kitaev, "Fault-tolerant quantum computation by anyons," *Annals of Physics*, vol. 303, no. 1, pp. 2–30, jan 2003. [Online]. Available: https://doi.org/10.1016%2Fs0003-4916%2802%2900018-0

[16]   M. Hays, V. Fatemi, D. Bouman, J. Cerrillo, S. Diamond, K. Serniak, T. Connolly, P. Krogstrup, J. Nygård, A. L. Yeyati, A. Geresdi, and M. H. Devoret, "Coherent manipulation of an Andreev spin qubit," *Science*, vol. 373, no. 6553, pp. 430–433, 2021. [Online]. Available: https://www.science.org/doi/abs/10.1126/science.abf0345

[17]   R. Aguado, "A perspective on semiconductor-based superconducting qubits," *Applied Physics Letters*, vol. 117, no. 24, p. 240501, 2020. [Online]. Available: https://doi.org/10.1063/5.0024124

[18]   M. Benito and G. Burkard, "Hybrid superconductor-semiconductor systems for quantum technology," *Applied Physics Letters*, vol. 116, no. 19, p. 190502, 2020. [Online]. Available: https://doi.org/10.1063/5.0004777

[19]   A. E. G. Mikkelsen, P. Kotetes, P. Krogstrup, and K. Flensberg, "Hybridization at superconductor-semiconductor interfaces," *Phys. Rev. X*, vol. 8, p. 031040, Aug 2018.

[20]   C. Blömers, T. Rieger, P. Zellekens, F. Haas, M. I. Lepsa, H. Hardtdegen, Ö. Gül, N. Demarina, D. Grützmacher, H. Lüth, and T. Schäpers, "Realization of nanoscaled tubular conductors by means of GaAs/InAs core/shell nanowires," *Nanotechnology*, vol. 24, no. 3, p. 035203, 2013.

[21]   T. Rieger, M. Luysberg, T. Schäpers, D. Grützmacher, and M. I. Lepsa, "Molecular beam epitaxy growth of GaAs/InAs core-shell nanowires and

fabrication of InAs nanotubes," *Nano Letters*, vol. 12, no. 11, pp. 5559–5564, Nov 2012. [Online]. Available: https://doi.org/10.1021/nl302502b

[22] F. Haas, K. Sladek, A. Winden, M. von der Ahe, T. E. Weirich, T. Rieger, H. Lüth, D. Grützmacher, T. Schäpers, and H. Hardtdegen, "Nanoimprint and selective-area MOVPE for growth of GaAs/InAs core/shell nanowires," *Nanotechnology*, vol. 24, no. 8, p. 085603, 2013.

[23] S. Funk, M. Royo, I. Zardo, D. Rudolph, S. Morkötter, B. Mayer, J. Becker, A. Bechtold, S. Matich, M. Döblinger, M. Bichler, G. Koblmüller, J. J. Finley, A. Bertoni, G. Goldoni, and G. Abstreiter, "High mobility one- and two-dimensional electron systems in nanowire-based quantum heterostructures," *Nano Letters*, vol. 13, no. 12, pp. 6189–6196, 2013.

[24] N. Erhard, S. Zenger, S. Morkötter, D. Rudolph, M. Weiss, H. J. Krenner, H. Karl, G. Abstreiter, J. J. Finley, G. Koblmüller, and A. W. Holleitner, "Ultrafast photodetection in the quantum wells of single AlGaAs/GaAs-based nanowires," *Nano Letters*, vol. 15, no. 10, pp. 6869–6874, 2015.

[25] M. Weiß, J. B. Kinzel, F. J. R. Schülein, M. Heigl, D. Rudolph, S. Morkötter, M. Döblinger, M. Bichler, G. Abstreiter, J. J. Finley, G. Koblmüller, A. Wixforth, and H. J. Krenner, "Dynamic acoustic control of individual optically active quantum dot-like emission centers in heterostructure nanowires," *Nano Letters*, vol. 14, no. 5, pp. 2256–2264, 2014.

[26] J. Jadczak, P. Plochocka, A. Mitioglu, I. Breslavetz, M. Royo, A. Bertoni, G. Goldoni, T. Smolenski, P. Kossacki, A. Kretinin, H. Shtrikman, and D. K. Maude, "Unintentional high-density p-type modulation doping of a GaAs/AlAs core–multishell nanowire," *Nano Letters*, vol. 14, no. 5, pp. 2807–2814, 2014.

[27] F. Qian, Y. Li, S. Gradečak, D. Wang, C. J. Barrelet, and C. M. Lieber, "Gallium Nitride-based nanowire radial heterostructures for nanophotonics," *Nano Letters*, vol. 4, no. 10, pp. 1975–1979, 2004.

[28] F. Qian, S. Gradečak, Y. Li, C.-Y. Wen, and C. M. Lieber, "Core/multi-shell nanowire heterostructures as multicolor, high-efficiency light-emitting diodes," *Nano Letters*, vol. 5, no. 11, pp. 2287–2291, 2005.

[29] L. Baird, G. Ang, C. Low, N. Haegel, A. Talin, Q. Li, and G. Wang, "Imaging minority carrier diffusion in GaN nanowires using near field optical microscopy," *Physica B: Condensed Matter*, vol. 404, no. 23–24, pp. 4933 – 4936, 2009.

[30] M. Heurlin, T. Stankevič, S. Mickevičius, S. Yngman, D. Lindgren, A. Mikkelsen, R. Feidenhans'l, M. T. Borgström, and L. Samuelson, "Structural properties of wurtzite InP–InGaAs nanowire core–shell heterostructures," *Nano Letters*, vol. 15, no. 4, pp. 2462–2467, 2015.

[31] Y. Dong, B. Tian, T. J. Kempa, and C. M. Lieber, "Coaxial group III-Nitride nanowire photovoltaics," *Nano Letters*, vol. 9, no. 5, pp. 2183–2187, 2009.

[32] X. Yuan, P. Caroff, F. Wang, Y. Guo, Y. Wang, H. E. Jackson, L. M. Smith, H. H. Tan, and C. Jagadish, "Antimony induced 112a faceted triangular $GaAs_{1-x}Sb_x$/InP core/shell nanowires and their enhanced optical quality," *Adv. Funct. Mater.*, vol. 25, pp. 5300–5308, 2015.

[33] D. J. O. Göransson, M. Heurlin, B. Dalelkhan, S. Abay, M. E. Messing, V. F. Maisi, M. T. Borgström, and H. Q. Xu, "Coulomb blockade from the shell of an InP-InAs core-shell nanowire with a triangular cross section," *Applied Physics Letters*, vol. 114, no. 5, p. 053108, Feb 2019.

[34] T. Rieger, D. Grutzmacher, and M. I. Lepsa, "Misfit dislocation free InAs/GaSb core-shell nanowires grown by molecular beam epitaxy," *Nanoscale*, vol. 7, pp. 356–364, 2015.

[35] K.-H. Kim and Y.-S. No, "Subwavelength core/shell cylindrical nanostructures for novel plasmonic and metamaterial devices," *Nano Convergence*, vol. 4, no. 1, p. 32, Dec 2017. [Online]. Available: https://doi.org/10.1186/s40580-017-0128-8

[36] G. Ferrari, G. Goldoni, A. Bertoni, G. Cuoghi, and E. Molinari, "Magnetic states in prismatic core multishell nanowires," *Nano Letters*, vol. 9, no. 4, pp. 1631–1635, 2009.

[37] B. M. Wong, F. Léonard, Q. Li, and G. T. Wang, "Nanoscale effects on heterojunction electron gases in GaN/AlGaN core/shell nanowires," *Nano Letters*, vol. 11, no. 8, pp. 3074–3079, 2011.

[38] A. Sitek, L. Serra, V. Gudmundsson, and A. Manolescu, "Electron localization and optical absorption of polygonal quantum rings," *Phys. Rev. B*, vol. 91, p. 235429, Jun 2015.

[39] A. Sitek, G. Thorgilsson, V. Gudmundsson, and A. Manolescu, "Multi-domain electromagnetic absorption of triangular quantum rings," *Nanotechnology*, vol. 27, no. 22, p. 225202, 2016.

[40] M. Royo, M. D. Luca, R. Rurali, and I. Zardo, "A review on III–V core–multishell nanowires: growth, properties, and applications," *Journal of*

Physics D: Applied Physics, vol. 50, no. 14, p. 143001, mar 2017. [Online]. Available: https://doi.org/10.1088/1361-6463/aa5d8e

[41] G. Shen and D. Chen, "One-dimensional nanostructures and devices of II–V group semiconductors," *Nanoscale Research Letters*, vol. 4, no. 8, p. 779, May 2009. [Online]. Available: https://doi.org/10.1007/s11671-009-9338-2

[42] G. Koblmüller, B. Mayer, T. Stettner, G. Abstreiter, and J. J. Finley, "GaAs–AlGaAs core–shell nanowire lasers on silicon: Invited review," *Semiconductor Science and Technology*, vol. 32, no. 5, p. 053001, apr 2017. [Online]. Available: https://doi.org/10.1088/1361-6641/aa5e45

[43] C. Florica, A. Costas, N. Preda, M. Beregoi, A. Kuncser, N. Apostol, C. Popa, G. Socol, V. Diculescu, and I. Enculescu, "Core-shell nanowire arrays based on ZnO and CuxO for water stable photocatalysts," *Scientific Reports*, vol. 9, no. 1, p. 17268, Nov 2019. [Online]. Available: https://doi.org/10.1038/s41598-019-53873-0

[44] M. A. Hassan, M. A. Johar, A. Waseem, I. V. Bagal, J.-S. Ha, and S.-W. Ryu, "Type-II ZnO/ZnS core-shell nanowires: Earth-abundant photoanode for solar-driven photoelectrochemical water splitting," *Opt. Express*, vol. 27, no. 4, pp. A184–A196, Feb 2019. [Online]. Available: http://opg.optica.org/oe/abstract.cfm?URI=oe-27-4-A184

[45] S. Z. Oener, S. A. Mann, B. Sciacca, C. Sfiligoj, J. Hoang, and E. C. Garnett, "Au-Cu2O core-shell nanowire photovoltaics," *Applied Physics Letters*, vol. 106, no. 2, p. 023501, 2015. [Online]. Available: https://doi.org/10.1063/1.4905652

[46] K. O. Klausen, A. Sitek, S. I. Erlingsson, and A. Manolescu, "Majorana zero modes in nanowires with combined triangular and hexagonal geometry," *Nanotechnology*, vol. 31, no. 35, p. 354001, jun 2020. [Online]. Available: https://doi.org/10.1088/1361-6528/ab932e

[47] V. Mourik, K. Zuo, S. M. Frolov, S. R. Plissard, E. P. A. M. Bakkers, and L. P. Kouwenhoven, "Signatures of Majorana fermions in hybrid superconductor-semiconductor nanowire devices," *Science*, vol. 336, no. 6084, p. 1003–1007, 2012.

[48] S. Vaitiekenas, G. W. Winkler, B. van Heck, T. Karzig, M.-T. Deng, K. Flensberg, L. I. Glazman, C. Nayak, P. Krogstrup, R. M. Lutchyn, and C. M. Marcus, "Flux-induced topological superconductivity in full-shell nanowires," *Science*, vol. 367, no. 6485, 2020.

[49] H. Zhang, C.-X. Liu, S. Gazibegovic, D. Xu, J. A. Logan, G. Wang, N. van Loo, J. D. S. Bommer, M. W. A. de Moor, D. Car, R. L. M. Op het Veld, P. J.

van Veldhoven, S. Koelling, M. A. Verheijen, M. Pendharkar, D. J. Pennachio, B. Shojaei, J. S. Lee, C. J. Palmstrøm, E. P. A. M. Bakkers, S. D. Sarma, and L. P. Kouwenhoven, "Editorial expression of concern: Quantized Majorana conductance," *Nature*, vol. 581, no. 7807, pp. E4–E4, May 2020. [Online]. Available: https://doi.org/10.1038/s41586-020-2252-6

[50] K. Ó. Klausen, *Theory of superconductivity*. Cham: Springer International Publishing, 2020, pp. 57–90. [Online]. Available: https://doi.org/10.1007/978-3-030-52222-3_5

[51] K. O. Klausen, A. Sitek, S. I. Erlingsson, and A. Manolescu, "Electron-hole coherence in core-shell nanowires with partial proximity induced superconductivity," *arXiv preprint arXiv:2206.04830*, 2022.

[52] M. A. Nielsen and I. L. Chuang, *Quantum Computation and Quantum Information: 10th Anniversary Edition*. Cambridge University Press, 2010.

[53] A. R. Calderbank, E. M. Rains, P. W. Shor, and N. J. A. Sloane, "Quantum error correction and orthogonal geometry," *Physical Review Letters*, vol. 78, no. 3, pp. 405–408, jan 1997. [Online]. Available: https://doi.org/10.1103%2Fphysrevlett.78.405

[54] S. Bravyi and A. Kitaev, "Universal quantum computation with ideal Clifford gates and noisy ancillas," *Physical Review A*, vol. 71, no. 2, feb 2005. [Online]. Available: https://doi.org/10.1103%2Fphysreva.71.022316

[55] L. K. Grover, "A fast quantum mechanical algorithm for database search," in *Proceedings of the Twenty-Eighth Annual ACM Symposium on Theory of Computing*, ser. STOC '96. New York, NY, USA: Association for Computing Machinery, 1996, p. 212–219. [Online]. Available: https://doi.org/10.1145/237814.237866

[56] P. Shor, "Algorithms for quantum computation: Discrete logarithms and factoring," in *Proceedings 35th Annual Symposium on Foundations of Computer Science*, 1994, pp. 124–134.

[57] T. J. W. I. R. Center and D. Coppersmith, "An approximate Fourier transform useful in quantum factoring," 1994.

[58] D. Bernstein, J. Buchmann, and E. Dahmen, *Post-Quantum Cryptography*. Springer Berlin Heidelberg, 2009.

[59] R. P. Feynman, "Simulating physics with computers," *International Journal of Theoretical Physics*, vol. 21, no. 6, pp. 467–488, Jun 1982. [Online]. Available: https://doi.org/10.1007/BF02650179

[60] J. A. Schreier, A. A. Houck, J. Koch, D. I. Schuster, B. R. Johnson, J. M. Chow, J. M. Gambetta, J. Majer, L. Frunzio, M. H. Devoret, S. M. Girvin, and R. J. Schoelkopf, "Suppressing charge noise decoherence in superconducting charge qubits," *Phys. Rev. B*, vol. 77, p. 180502, May 2008. [Online]. Available: https://link.aps.org/doi/10.1103/PhysRevB.77.180502

[61] I. research. Credit: Carl De Torres of StoryTK for IBM, "IBM quantum eagle chip," 2021. [Online]. Available: https://www.flickr.com/photos/ibm_research_zurich/51683017865/in/photostream/

[62] M. Troyer, "A quantum computing future for condensed matter physics." CMD 29 Manchester, Aug 2022.

[63] IBM, "IBM Quantum system one in Ehningen, Germany." 2020. [Online]. Available: https://www.flickr.com/photos/ibm_research_zurich/51248690716/in/photostream/

[64] ——, "IBM Quantum system one (CES 2020): Interior of an IBM Quantum computing system," 2020. [Online]. Available: https://www.flickr.com/photos/ibm_research_zurich/50252942522/in/photostream/

[65] J. Preskill, *Fault-tolerant quantum computation.* World Scientific, 1998, pp. 213–269. [Online]. Available: https://www.worldscientific.com/doi/abs/10.1142/9789812385253_0008

[66] A. R. Calderbank and P. W. Shor, "Good quantum error-correcting codes exist," *Phys. Rev. A*, vol. 54, pp. 1098–1105, Aug 1996. [Online]. Available: https://link.aps.org/doi/10.1103/PhysRevA.54.1098

[67] C. Nayak, S. H. Simon, A. Stern, M. Freedman, and S. D. Sarma, "Non-Abelian anyons and topological quantum computation," *Reviews of Modern Physics*, vol. 80, no. 3, pp. 1083–1159, sep 2008. [Online]. Available: https://doi.org/10.1103%2Frevmodphys.80.1083

[68] M. V. Berry, "Quantal phase factors accompanying adiabatic changes," *Proceedings of the Royal Society of London. A. Mathematical and Physical Sciences*, vol. 392, no. 1802, p. 45–57, 1984. [Online]. Available: https://royalsocietypublishing.org/doi/abs/10.1098/rspa.1984.0023

[69] E. Cohen, H. Larocque, F. Bouchard, F. Nejadsattari, Y. Gefen, and E. Karimi, "Geometric phase from Aharonov-Bohm to Pancharatnam-Berry and beyond," *Nature Reviews Physics*, vol. 1, no. 7, p. 437–449, 2019. [Online]. Available: https://doi.org/10.1038/s42254-019-0071-1

[70] M. Gradhand, D. V. Fedorov, F. Pientka, P. Zahn, I. Mertig, and B. L. Györffy, "First-principle calculations of the Berry curvature of Bloch states for charge and spin transport of electrons," *Journal of Physics: Condensed Matter*, vol. 24, no. 21, p. 213202, may 2012. [Online]. Available: https://doi.org/10.1088/0953-8984/24/21/213202

[71] B. Simon, "Holonomy, the quantum adiabatic theorem, and Berry's phase," *Phys. Rev. Lett.*, vol. 51, p. 2167–2170, Dec 1983. [Online]. Available: https://link.aps.org/doi/10.1103/PhysRevLett.51.2167

[72] J. B. Parker, "Topological phase in plasma physics," *Journal of Plasma Physics*, vol. 87, no. 2, apr 2021. [Online]. Available: https://doi.org/10.1017%2Fs0022377821000301

[73] S. Chaudhary, M. Endres, and G. Refael, "Berry electrodynamics: Anomalous drift and pumping from a time-dependent Berry connection," *Phys. Rev. B*, vol. 98, p. 064310, Aug 2018. [Online]. Available: https://link.aps.org/doi/10.1103/PhysRevB.98.064310

[74] D. Xiao, M.-C. Chang, and Q. Niu, "Berry phase effects on electronic properties," *Rev. Mod. Phys.*, vol. 82, pp. 1959–2007, Jul 2010. [Online]. Available: https://link.aps.org/doi/10.1103/RevModPhys.82.1959

[75] A. Stern, "Berry's phase, motive forces, and mesoscopic conductivity," *Phys. Rev. Lett.*, vol. 68, pp. 1022–1025, Feb 1992. [Online]. Available: https://link.aps.org/doi/10.1103/PhysRevLett.68.1022

[76] D. J. Thouless, "Quantization of particle transport," *Phys. Rev. B*, vol. 27, pp. 6083–6087, May 1983. [Online]. Available: https://link.aps.org/doi/10.1103/PhysRevB.27.6083

[77] F. Wilczek and A. Zee, "Appearance of gauge structure in simple dynamical systems," *Phys. Rev. Lett.*, vol. 52, pp. 2111–2114, Jun 1984. [Online]. Available: https://link.aps.org/doi/10.1103/PhysRevLett.52.2111

[78] R. R. Aldinger, A. Böhm, and M. Loewe, "Non-Abelian Berry phase in a quantum mechanical environment," *Foundations of Physics Letters*, vol. 4, no. 3, pp. 217–234, Jun. 1991.

[79] M. Nakahara, *Geometry, Topology and Physics*. Taylor & Francis Group, 2003.

[80] I. Aitchison and A. J. G. Hey, *Gauge Theories in Particle Physics Volume 1: From Relativistic Quantum Mechanics to QED*. Oxford: Taylor & Francis Group, 2003.

[81] J. Pachos, P. Zanardi, and M. Rasetti, "Non-Abelian Berry connections for quantum computation," *Physical Review A*, vol. 61, no. 1, dec 1999. [Online]. Available: https://doi.org/10.1103%2Fphysreva.61.010305

[82] C. W. J. Beenakker, "Search for non-Abelian Majorana braiding statistics in superconductors," *arXiv e-prints*, p. arXiv:1907.06497, Jul 2019.

[83] J. M. Leinaas and J. Myrheim, "On the theory of identical particles," *Il Nuovo Cimento B (1971-1996)*, vol. 37, no. 1, pp. 1–23, Jan 1977. [Online]. Available: https://doi.org/10.1007/BF02727953

[84] A. Kitaev, "Periodic table for topological insulators and superconductors," *AIP Conference Proceedings*, vol. 1134, no. 1, p. 22–30, 2009. [Online]. Available: https://aip.scitation.org/doi/abs/10.1063/1.3149495

[85] V. Gudmundsson, "Topological phases beyond the Hofstadter butterfly," *Physics Online Journal*, vol. 13, p. 187, Dec. 2020.

[86] X.-G. Wen, "Topological order: From long-range entangled quantum matter to a unified origin of light and electrons," *ISRN Condensed Matter Physics*, vol. 2013, pp. 1–20, mar 2013. [Online]. Available: https://doi.org/10.1155%2F2013%2F198710

[87] A. Y. Kitaev, "Unpaired Majorana fermions in quantum wires," *Physics-Uspekhi*, vol. 44, no. 10S, pp. 131–136, oct 2001. [Online]. Available: https://doi.org/10.1070%2F1063-7869%2F44%2F10s%2Fs29

[88] D. A. Ivanov, "Non-Abelian statistics of half-quantum vortices in p-wave superconductors," *Phys. Rev. Lett.*, vol. 86, pp. 268–271, Jan 2001. [Online]. Available: https://link.aps.org/doi/10.1103/PhysRevLett.86.268

[89] J. F. Annett, "Unconventional superconductivity," *Contemporary Physics*, vol. 36, no. 6, pp. 423–437, 1995. [Online]. Available: https://doi.org/10.1080/00107519508232300

[90] J.-P. Brison, "p-wave superconductivity and d-vector representation," in *Magnetism and Accelerator-Based Light Sources*, H. Bulou, L. Joly, J.-M. Mariot, and F. Scheurer, Eds. Cham: Springer International Publishing, 2021, pp. 165–204.

[91] J. Alicea, "Majorana fermions in a tunable semiconductor device," *Phys. Rev. B*, vol. 81, p. 125318, Mar 2010. [Online]. Available: https://link.aps.org/doi/10.1103/PhysRevB.81.125318

[92] R. M. Lutchyn, J. D. Sau, and S. Das Sarma, "Majorana fermions and a topological phase transition in semiconductor-superconductor heterostructures," *Phys. Rev. Lett.*, vol. 105, p. 077001, Aug 2010. [Online]. Available: https://link.aps.org/doi/10.1103/PhysRevLett.105.077001

[93] Y. Oreg, G. Refael, and F. von Oppen, "Helical liquids and Majorana bound states in quantum wires," *Phys. Rev. Lett.*, vol. 105, p. 177002, Oct 2010. [Online]. Available: https://link.aps.org/doi/10.1103/PhysRevLett.105.177002

[94] K. Flensberg, F. von Oppen, and A. Stern, "Engineered platforms for topological superconductivity and Majorana zero modes," *Nature Reviews Materials*, vol. 6, no. 10, pp. 944–958, Oct 2021. [Online]. Available: https://doi.org/10.1038/s41578-021-00336-6

[95] H. Zhang, D. E. Liu, M. Wimmer, and L. P. Kouwenhoven, "Next steps of quantum transport in Majorana nanowire devices," *Nature Communications*, vol. 10, no. 1, p. 5128, 2019. [Online]. Available: https://doi.org/10.1038/s41467-019-13133-1

[96] P. Zellekens, N. Demarina, J. Janßen, T. Rieger, M. I. Lepsa, P. Perla, G. Panaitov, H. Lüth, D. Grützmacher, and T. Schäpers, "Phase coherent transport and spin-orbit interaction in GaAs/InSb core/shell nanowires," *Semiconductor Science and Technology*, vol. 35, no. 8, p. 085003, jun 2020. [Online]. Available: https://doi.org/10.1088%2F1361-6641%2Fab8396

[97] S. Trebst, M. Troyer, Z. Wang, and A. W. W. Ludwig, "A short introduction to Fibonacci anyon models," *Progress of Theoretical Physics Supplement*, vol. 176, pp. 384–407, 2008. [Online]. Available: https://doi.org/10.1143%2Fptps.176.384

[98] E. Génetay Johansen and T. Simula, "Fibonacci anyons versus Majorana fermions: A Monte Carlo approach to the compilation of braid circuits in $SU(2)_k$ anyon models," *PRX Quantum*, vol. 2, p. 010334, Mar 2021. [Online]. Available: https://link.aps.org/doi/10.1103/PRXQuantum.2.010334

[99] Y.-M. Zhan, Y.-G. Chen, B. Chen, Z. Wang, Y. Yu, and X. Luo, "Universal topological quantum computation with strongly correlated Majorana edge modes," *New Journal of Physics*, vol. 24, no. 4, p. 043009, apr 2022. [Online]. Available: https://doi.org/10.1088%2F1367-2630%2Fac5f87

[100] Microsoft Quantum, "InAs-Al hybrid devices passing the topological gap protocol," 2022. [Online]. Available: https://arxiv.org/abs/2207.02472

[101] H. Pan and S. Das Sarma, "On-demand large conductance in trivial zero-bias tunneling peaks in Majorana nanowires," *Phys. Rev. B*, vol. 105, p. 115432, Mar 2022. [Online]. Available: https://link.aps.org/doi/10.1103/PhysRevB.105.115432

[102] H. Zhang, C.-X. Liu, S. Gazibegovic, D. Xu, J. A. Logan, G. Wang, N. van Loo, J. D. S. Bommer, M. W. A. de Moor, D. Car, R. L. M. Op het Veld, P. J. van Veldhoven, S. Koelling, M. A. Verheijen, M. Pendharkar, D. J. Pennachio, B. Shojaei, J. S. Lee, C. J. Palmstrøm, E. P. A. M. Bakkers, S. Das Sarma, and L. P. Kouwenhoven, "Retraction note: Quantized Majorana conductance," *Nature*, vol. 591, no. 7851, pp. E30–E30, Mar 2021. [Online]. Available: https://doi.org/10.1038/s41586-021-03373-x

[103] D. van Delft and P. Kes, "The discovery of superconductivity," *Physics Today*, vol. 63, no. 9, p. 38–43, Sep. 2010. [Online]. Available: https://doi.org/10.1063/1.3490499

[104] F. London and H. London, "The electromagnetic equations of the supraconductor," *Proceedings of the Royal Society A: Mathematical, Physical and Engineering Sciences*, vol. 149, no. 866, pp. 71–88, 1935.

[105] M. Tinkham, *Introduction to Superconductivity*. Dover Publications, Inc. Mineola, New York., 2003.

[106] P. D. D. Gennes, *Superconductivity of Metals and Alloys*. Westview Press, 1999.

[107] F. London, *Superfluids*. John Wiley & Sons, Inc: New york., 1950.

[108] A. C. Rose-Innes and E. H. Rhoderick, *Introduction to Superconductivity*. Pergamon Press, 1988.

[109] A. B. Pippard and W. L. Bragg, "An experimental and theoretical study of the relation between magnetic field and current in a superconductor," *Proceedings of the Royal Society of London.*, vol. 216, no. 1127, pp. 547–568, 1953.

[110] M. Cyrot, "Ginzburg-Landau theory for superconductors," *Reports on Progress in Physics*, 1973.

[111] V. L. Ginzburg, "On superconductivity and superfluidity (what i have and have not managed to do), as well as on the 'physical minimum' at the beginning of the XXI century (december 8, 2003)," *Physics-Uspekhi*, vol. 47, no. 11, p. 1155–1170, nov 2004. [Online]. Available: https://doi.org/10.1070%2Fpu2004v047n11abeh001825

[112] V. L. Ginzburg and L. D. Landau, "On the theory of superconductivity," *Zh. Eksp. Teor. Fiz.*, vol. 20, p. 1064–1082, 1950.

[113] A. A. Abrikosov, "Nobel lecture: Type-II superconductors and the vortex lat-
       tice," *Reviews of Modern Physics*, vol. 76, 2004.

[114] J. D. Jackson, *Classical Electrodynamics*, 3rd ed.   New York: John Wiley &
       Sons, 1999.

[115] D. K. Cheng, *Field and Wave Electromagnetics*.   Massach.: Addison-Wesley,
       1983.

[116] B. D. Josephson, "Macroscopic field equations for metals in equilibrium,"
       Phys. Rev., vol. 152, p. 211–217, Dec 1966. [Online]. Available: https:
       //link.aps.org/doi/10.1103/PhysRev.152.211

[117] M. N. Wilson, *Superconducting Magnets*.   Oxford Science Publications, 1986.

[118] F. Hellman, E. M. Gyorgy, D. W. Johnson, H. M. O'Bryan, and R. C.
       Sherwood, "Levitation of a magnet over a flat type II superconductor," *Journal
       of Applied Physics*, vol. 63, no. 2, p. 447–450, 1988. [Online]. Available:
       https://doi.org/10.1063/1.340262

[119] D. R. Tilley and J. Tilley, *Superfluidity and Superconductivity*.   Bristol: Adam
       Hilger, 1990.

[120] A. L. Fetter and J. D. Walecka, *Quantum Theory of Many-Particle Systems*.
       New York: Dover., 2003.

[121] R. P. Feynman, R. B. Leighton, and M. Sands, *The Feynman lectures on physics*.
       New York, NY: Basic Books, 2010, vol. 3, originally published 1963-1965.
       [Online]. Available: https://cds.cern.ch/record/1494701

[122] B. Josephson, "Possible new effects in superconductive tunnelling," *Physics
       Letters*, vol. 1, no. 7, p. 251–253, 1962. [Online]. Available: http://www.
       sciencedirect.com/science/article/pii/0031916362913690

[123] H. Bruus and K. Flensberg, *Many-body quantum theory in condensed matter
       physics - an introduction*.   United States: Oxford University Press, 2004.

[124] A. A. Golubov, M. Y. Kupriyanov, and E. Il'ichev, "The current-phase relation
       in Josephson junctions," *Rev. Mod. Phys.*, vol. 76, p. 411–469, Apr 2004.
       [Online]. Available: https://link.aps.org/doi/10.1103/RevModPhys.76.411

[125] S. S. Hegde, G. Yue, Y. Wang, E. Huemiller, D. Van Harlingen, and
       S. Vishveshwara, "A topological Josephson junction platform for creating,
       manipulating, and braiding Majorana bound states," *Annals of Physics*, vol.
       423, p. 168326, 2020. [Online]. Available: https://www.sciencedirect.com/
       science/article/pii/S0003491620302608

[126] E. Prada, P. San-Jose, M. W. A. de Moor, A. Geresdi, E. J. H. Lee, J. Klinovaja, D. Loss, J. Nygård, R. Aguado, and L. P. Kouwenhoven, "From Andreev to Majorana bound states in hybrid superconductor–semiconductor nanowires," *Nature Reviews Physics*, vol. 2, no. 10, pp. 575–594, Oct 2020. [Online]. Available: https://doi.org/10.1038/s42254-020-0228-y

[127] R. C. Jaklevic, J. Lambe, A. H. Silver, and J. E. Mercereau, "Quantum interference effects in Josephson tunneling," *Phys. Rev. Lett.*, vol. 12, p. 159–160, Feb 1964. [Online]. Available: https://link.aps.org/doi/10.1103/PhysRevLett.12.159

[128] E. Maxwell, "Isotope effect in the superconductivity of mercury," *Physical Review*, vol. 78, 1950.

[129] L. N. Cooper, "Bound electron pairs in a degenerate Fermi gas," *Phys. Rev.*, vol. 104, p. 1189–1190, Nov 1956. [Online]. Available: https://link.aps.org/doi/10.1103/PhysRev.104.1189

[130] J. Bardeen, L. N. Cooper, and J. R. Schrieffer, "Microscopic theory of superconductivity," *Phys. Rev.*, vol. 106, p. 162–164, Apr 1957. [Online]. Available: https://link.aps.org/doi/10.1103/PhysRev.106.162

[131] J.-X. Zhu, *Bogoliubov de Gennes Methods and its Applications*. Springer, 2016.

[132] G. E. Blonder, M. Tinkham, and T. M. Klapwijk, "Transition from metallic to tunneling regimes in superconducting microconstrictions: Excess current, charge imbalance, and supercurrent conversion," *Phys. Rev. B*, vol. 25, pp. 4515–4532, Apr 1982.

[133] R. Holm and W. Meissner, "Messungen mit hilfe von flüssigem helium. xiii," *Zeitschrift für Physik*, vol. 74, no. 11, p. 715–735, Nov 1932. [Online]. Available: https://doi.org/10.1007/BF01340420

[134] B. Pannetier and H. Courtois, "Andreev reflection and proximity effect," *Journal of Low Temperature Physics*, vol. 118, pp. 599–615, 2000.

[135] T. M. Klapwijk, "Proximity effect from an Andreev perspective," *Journal of Superconductivity*, vol. 17, no. 5, p. 593–611, 2004. [Online]. Available: https://doi.org/10.1007/s10948-004-0773-0

[136] T. Schäpers, *Superconductor/Semiconductor Junctions*. Springer-Verlag Berlin Heidelberg, 2001.

[137] A. Andreev, "Thermal conductivity of the intermediate state of superconductors." *Journal of Experimental and Theoretical Physics*, vol. 46, pp. 1823–1828, 1964.

[138] C. W. J. Beenakker, "Quantum transport in semiconductor-superconductor microjunctions," *Phys. Rev. B*, vol. 46, p. 12841–12844, Nov 1992. [Online]. Available: https://link.aps.org/doi/10.1103/PhysRevB.46.12841

[139] K. Y. Bliokh, A. Y. Bekshaev, and F. Nori, "Extraordinary momentum and spin in evanescent waves," *Nature Commun.*, vol. 5, p. 3300, 2014.

[140] M. Antognozzi, C. R. Bermingham, R. L. Harniman, S. Simpson, J. Senior, R. Hayward, H. Hoerber, M. R. Dennis, A. Y. Bekshaev, K. Y. Bliokh, and F. Nori, "Direct measurements of the extraordinary optical momentum and transverse spin-dependent force using a nano-cantilever," *arXiv e-prints*, Jun 2015.

[141] J. C. J. Paasschens, M. J. M. de Jong, P. W. Brouwer, and C. W. J. Beenakker, "Reflection of light from a disordered medium backed by a phase-conjugating mirror," *Phys. Rev. A*, vol. 56, p. 4216–4228, Nov 1997. [Online]. Available: https://link.aps.org/doi/10.1103/PhysRevA.56.4216

[142] W. D. Montgomery, "Time reversal and vector phase conjugation," *Il Nuovo Cimento B (1971-1996)*, vol. 79, no. 1, p. 13–32, Jan 1984. [Online]. Available: https://doi.org/10.1007/BF02723834

[143] M. Nieto-Vesperinas and E. Wolf, "Phase conjugation and symmetries with wave fields in free space containing evanescent components," *J. Opt. Soc. Am. A*, vol. 2, no. 9, p. 1429–1434, Sep 1985. [Online]. Available: http://josaa.osa.org/abstract.cfm?URI=josaa-2-9-1429

[144] A. Y. Okulov, "Angular momentum of photons and phase conjugation," *Journal of Physics B Atomic Molecular Physics*, vol. 41, no. 10, p. 101001, May 2008.

[145] K. Atkins and I. Rudnick, *Progress in Low Temperature Physics*.   Amsterdam: North-Holland, 1970, vol. 6.

[146] S. Huberman, R. A. Duncan, K. Chen, B. Song, V. Chiloyan, Z. Ding, A. A. Maznev, G. Chen, and K. A. Nelson, "Observation of second sound in graphite at temperatures above 100 K," *Science*, vol. 364, no. 6438, p. 375–379, 2019. [Online]. Available: https://science.sciencemag.org/content/364/6438/375

[147] K. P. Sinha, C. Sivaram, and E. C. G. Sudarshan, "Aether as a superfluid state of particle-antiparticle pairs," *Foundations of Physics*, vol. 6, no. 1, p. 65–70, 1976. [Online]. Available: https://doi.org/10.1007/BF00708664

[148] P. A. M. Dirac, "A new classical theory of electrons," *Proceedings of the Royal Society of London. Series A. Mathematical and Physical Sciences*, vol. 209, no. 1098, p. 291–296, 1951. [Online]. Available: https://royalsocietypublishing.org/doi/abs/10.1098/rspa.1951.0204

[149] ——, "A new classical theory of electrons. II," *Proceedings of the Royal Society of London. Series A. Mathematical and Physical Sciences*, vol. 212, no. 1110, p. 330–339, 1952.

[150] M. P. Silverman and R. L. Mallett, "Dark matter as a cosmic Bose-Einstein condensate and possible superfluid," *General Relativity and Gravitation*, vol. 34, no. 5, p. 633–649, 2002. [Online]. Available: https://doi.org/10.1023/A:1015934027224

[151] S. Liberati and L. Maccione, "Astrophysical constraints on Planck scale dissipative phenomena," *Phys. Rev. Lett.*, vol. 112, p. 151301, Apr 2014. [Online]. Available: https://link.aps.org/doi/10.1103/PhysRevLett.112.151301

[152] L. Berezhiani and J. Khoury, "Dark matter superfluidity and galactic dynamics," *Physics Letters B*, vol. 753, p. 639–643, 2016. [Online]. Available: http://www.sciencedirect.com/science/article/pii/S0370269315010023

[153] P. W. Anderson, "Higgs, Anderson and all that," *Nature Physics*, vol. 11, no. 2, p. 93–93, 2015. [Online]. Available: https://doi.org/10.1038/nphys3247

[154] J. Goldstone, "Field theories with superconductor solutions," *Il Nuovo Cimento (1955-1965)*, vol. 19, no. 1, p. 154–164, 1961. [Online]. Available: https://doi.org/10.1007/BF02812722

[155] P. W. Higgs, "Broken symmetries and the masses of gauge bosons," *Phys. Rev. Lett.*, vol. 13, p. 508–509, Oct 1964. [Online]. Available: https://link.aps.org/doi/10.1103/PhysRevLett.13.508

[156] P. W. Anderson, "Plasmons, gauge invariance, and mass," *Phys. Rev.*, vol. 130, p. 439–442, Apr 1963. [Online]. Available: https://link.aps.org/doi/10.1103/PhysRev.130.439

[157] Y. Nambu, "Quasi-particles and gauge invariance in the theory of superconductivity," *Phys. Rev.*, vol. 117, p. 648–663, Feb 1960. [Online]. Available: https://link.aps.org/doi/10.1103/PhysRev.117.648

[158] A. J. Beekman, L. Rademaker, and J. van Wezel, "An introduction to spontaneous symmetry breaking," *SciPost Phys. Lect. Notes*, p. 11, 2019. [Online]. Available: https://scipost.org/10.21468/SciPostPhysLectNotes.11

[159] R. Shimano and N. Tsuji, "Higgs mode in superconductors," *Annual Review of Condensed Matter Physics*, vol. 11, no. 1, pp. 103–124, 2020. [Online]. Available: https://doi.org/10.1146/annurev-conmatphys-031119-050813

[160] T. D. Stanescu, R. M. Lutchyn, and S. Das Sarma, "Majorana fermions in semiconductor nanowires," *Phys. Rev. B*, vol. 84, p. 144522, Oct 2011. [Online]. Available: https://link.aps.org/doi/10.1103/PhysRevB.84.144522

[161] C.-K. Chiu, J. C. Y. Teo, A. P. Schnyder, and S. Ryu, "Classification of topological quantum matter with symmetries," *Rev. Mod. Phys.*, vol. 88, p. 035005, Aug 2016. [Online]. Available: https://link.aps.org/doi/10.1103/RevModPhys.88.035005

[162] T. D. Stanescu and S. Tewari, "Majorana fermions in semiconductor nanowires: Fundamentals, modeling, and experiment," *Journal of Physics: Condensed Matter*, vol. 25, no. 23, p. 233201, may 2013. [Online]. Available: https://doi.org/10.1088%2F0953-8984%2F25%2F23%2F233201

[163] X. Yuan, P. Caroff, F. Wang, Y. Guo, Y. Wang, H. E. Jackson, L. M. Smith, H. H. Tan, and C. Jagadish, "Antimony induced 112A faceted triangular GaAs1-xSbx/InP core/shell nanowires and their enhanced optical quality," *Advanced Functional Materials*, vol. 25, no. 33, p. 5300–5308, 2015.

[164] J. Hajer, M. Kessel, C. Brüne, M. Stehno, H. Buhmann, and L. Molenkamp, "Proximity induced superconductivity in CdTe-HgTe core-shell nanowires," *Nano Letters*, 2019.

[165] F. Haas, S. Dickheuer, P. Zellekens, T. Rieger, M. I. Lepsa, H. Lüth, D. Grützmacher, and T. Schäpers, "Quantum interferometer based on GaAs/InAs core/shell nanowires connected to superconducting contacts," *Semiconductor Science and Technology*, vol. 33, no. 6, p. 064001, apr 2018. [Online]. Available: https://doi.org/10.1088%2F1361-6641%2Faabc6d

[166] Y. Zhang, H. A. Fonseka, M. Aagesen, J. A. Gott, A. M. Sanchez, J. Wu, D. Kim, P. Jurczak, S. Huo, and H. Liu, "Growth of pure Zinc-blende GaAs(P) core–shell nanowires with highly regular morphology," *Nano Letters*, vol. 17, no. 8, pp. 4946–4950, Aug 2017. [Online]. Available: https://doi.org/10.1021/acs.nanolett.7b02063

[167] Y. Zhang, G. Davis, H. A. Fonseka, A. Velichko, A. Gustafsson, T. Godde, D. Saxena, M. Aagesen, P. W. Parkinson, J. A. Gott, S. Huo, A. M. Sanchez, D. J. Mowbray, and H. Liu, "Highly strained III–V–V coaxial nanowire quantum wells with strong carrier confinement," *ACS Nano*, vol. 13, no. 5, pp. 5931–5938, May 2019. [Online]. Available: https://doi.org/10.1021/acsnano.9b01775

[168] M. M. Sonner, A. Sitek, L. Janker, D. Rudolph, D. Ruhstorfer, M. Döblinger, A. Manolescu, G. Abstreiter, J. J. Finley, A. Wixforth, G. Koblmüller, and H. J. Krenner, "Breakdown of corner states and carrier localization

by monolayer fluctuations in radial nanowire quantum wells," *Nano Letters*, vol. 19, no. 5, pp. 3336–3343, May 2019. [Online]. Available: https://doi.org/10.1021/acs.nanolett.9b01028

[169] K. Pöyhönen, A. WeststrÖm, J. Röntynen, and T. Ojanen, "Majorana states in helical Shiba chains and ladders," *Phys. Rev. B*, vol. 89, p. 115109, Mar 2014.

[170] R. Wakatsuki, M. Ezawa, and N. Nagaosa, "Majorana fermions and multiple topological phase transition in Kitaev ladder topological superconductors," *Phys. Rev. B*, vol. 89, p. 174514, May 2014.

[171] N. Sedlmayr, J. M. Aguiar-Hualde, and C. Bena, "Majorana bound states in open quasi-one-dimensional and two-dimensional systems with transverse Rashba coupling," *Phys. Rev. B*, vol. 93, p. 155425, Apr 2016. [Online]. Available: https://link.aps.org/doi/10.1103/PhysRevB.93.155425

[172] K. A. Dick, C. Thelander, L. Samuelson, and P. Caroff, "Crystal phase engineering in single InAs nanowires," *Nano Letters*, vol. 10, no. 9, pp. 3494–3499, Sep 2010. [Online]. Available: https://doi.org/10.1021/nl101632a

[173] C. Daday, A. Manolescu, D. C. Marinescu, and V. Gudmundsson, "Electronic charge and spin density distribution in a quantum ring with spin-orbit and Coulomb interactions," *Phys. Rev. B*, vol. 84, p. 115311, Sep 2011. [Online]. Available: https://link.aps.org/doi/10.1103/PhysRevB.84.115311

[174] A. Bringer and T. Schäpers, "Spin precession and modulation in ballistic cylindrical nanowires due to the Rashba effect," *Phys. Rev. B*, vol. 83, p. 115305, Mar 2011. [Online]. Available: https://link.aps.org/doi/10.1103/PhysRevB.83.115305

[175] P. Wójcik, A. Bertoni, and G. Goldoni, "Enhanced Rashba spin-orbit coupling in core-shell nanowires by the interfacial effect," *Applied Physics Letters*, vol. 114, no. 7, p. 073102, 2019. [Online]. Available: https://doi.org/10.1063/1.5082602

[176] F. Peñaranda, R. Aguado, P. San-Jose, and E. Prada, "Even-odd effect and Majorana states in full-shell nanowires," *Physical Review Research*, vol. 2, no. 2, may 2020. [Online]. Available: https://doi.org/10.1103%2Fphysrevresearch.2.023171

[177] M. P. Nowak and P. Wójcik, "Probing andreev reflection reach in semiconductor-superconductor hybrids by Aharonov-Bohm effect," *Applied Physics Letters*, vol. 114, no. 4, p. 043104, 2019.

[178] T. D. Stanescu and S. Das Sarma, "Proximity-induced low-energy renormalization in hybrid semiconductor-superconductor Majorana structures," *Phys. Rev. B*, vol. 96, p. 014510, Jul 2017. [Online]. Available: https://link.aps.org/doi/10.1103/PhysRevB.96.014510

[179] G. Stenuit, S. Michotte, J. Govaerts, and L. Piraux, "Temperature dependence of penetration and coherence lengths in lead nanowires," *Superconductor Science and Technology*, vol. 18, no. 1, pp. 174–182, nov 2004. [Online]. Available: https://doi.org/10.1088%2F0953-2048%2F18%2F1%2F027

[180] N. N. Bogoliubov, "On a new method in the theory of superconductivity," *Nuovo Cim.*, vol. 7, pp. 794–805, 1958.

[181] M. Sato and Y. Ando, "Topological superconductors: A review," *Reports on Progress in Physics*, vol. 80, no. 7, p. 076501, may 2017. [Online]. Available: https://doi.org/10.1088%2F1361-6633%2Faa6ac7

[182] Q. Niu, D. J. Thouless, and Y.-S. Wu, "Quantized Hall conductance as a topological invariant," *Phys. Rev. B*, vol. 31, pp. 3372–3377, Mar 1985. [Online]. Available: https://link.aps.org/doi/10.1103/PhysRevB.31.3372

[183] X.-L. Qi and S.-C. Zhang, "Topological insulators and superconductors," *Rev. Mod. Phys.*, vol. 83, pp. 1057–1110, Oct 2011. [Online]. Available: https://link.aps.org/doi/10.1103/RevModPhys.83.1057

[184] J. C. Budich and B. Trauzettel, "From the adiabatic theorem of quantum mechanics to topological states of matter," *physica status solidi (RRL) – Rapid Research Letters*, vol. 7, no. 1-2, pp. 109–129, 2013. [Online]. Available: https://onlinelibrary.wiley.com/doi/abs/10.1002/pssr.201206416

[185] B. Nijholt and A. R. Akhmerov, "Orbital effect of magnetic field on the Majorana phase diagram," *Phys. Rev. B*, vol. 93, p. 235434, Jun 2016. [Online]. Available: https://link.aps.org/doi/10.1103/PhysRevB.93.235434

[186] V. Kaladzhyan, J. Despres, I. Mandal, and C. Bena, "Majorana fermions in finite-size strips with in-plane magnetic fields," *European Physical Journal B*, vol. 90, no. 11, p. 211, Nov 2017.

[187] J. Chen, P. Yu, J. Stenger, M. Hocevar, D. Car, S. R. Plissard, E. P. A. M. Bakkers, T. D. Stanescu, and S. M. Frolov, "Experimental phase diagram of zero-bias conductance peaks in superconductor/semiconductor nanowire devices," *Science Advances*, vol. 3, no. 9, 2017. [Online]. Available: https://advances.sciencemag.org/content/3/9/e1701476

[188] L. Fu and C. L. Kane, "Superconducting proximity effect and Majorana fermions at the surface of a topological insulator," *Phys. Rev. Lett.*, vol. 100, p. 096407, Mar 2008. [Online]. Available: https://link.aps.org/doi/10.1103/PhysRevLett.100.096407

[189] X.-P. Liu, Y. Zhou, Y.-F. Wang, and C.-D. Gong, "Characterizations of topological superconductors: Chern numbers, edge states and Majorana zero modes," *New Journal of Physics*, vol. 19, no. 9, p. 093018, sep 2017. [Online]. Available: https://doi.org/10.1088%2F1367-2630%2Faa8022

[190] M. Sekania, S. Plugge, M. Greiter, R. Thomale, and P. Schmitteckert, "Braiding errors in interacting Majorana quantum wires," *Phys. Rev. B*, vol. 96, p. 094307, Sep 2017. [Online]. Available: https://link.aps.org/doi/10.1103/PhysRevB.96.094307

[191] A. Nag and J. D. Sau, "Diabatic errors in Majorana braiding with bosonic bath," *Phys. Rev. B*, vol. 100, p. 014511, Jul 2019. [Online]. Available: https://link.aps.org/doi/10.1103/PhysRevB.100.014511

[192] F. Harper, A. Pushp, and R. Roy, "Majorana braiding in realistic nanowire Y-junctions and tuning forks," *Phys. Rev. Research*, vol. 1, p. 033207, Dec 2019. [Online]. Available: https://link.aps.org/doi/10.1103/PhysRevResearch.1.033207

[193] F. Setiawan, C.-T. Wu, and K. Levin, "Full proximity treatment of topological superconductors in Josephson-junction architectures," *Phys. Rev. B*, vol. 99, p. 174511, May 2019. [Online]. Available: https://link.aps.org/doi/10.1103/PhysRevB.99.174511

[194] T. D. Stanescu, R. M. Lutchyn, and S. Das Sarma, "Soft superconducting gap in semiconductor-based Majorana nanowires," *Phys. Rev. B*, vol. 90, p. 085302, Aug 2014. [Online]. Available: https://link.aps.org/doi/10.1103/PhysRevB.90.085302

[195] A. Jacobs, R. Kümmel, and H. Plehn, "Proximity effect, Andreev reflections, and charge transport in mesoscopic superconducting/semiconducting heterostructures," *Superlattices and Microstructures*, vol. 25, no. 5, pp. 669–681, 1999. [Online]. Available: https://www.sciencedirect.com/science/article/pii/S0749603699907188

[196] A. I. D'yachenko and I. V. Kochergin, "Proximity-effect theory in thick NS sandwiches," *J. Low Temp. Phys.*, vol. 84:3-4, 8 1991.

[197] C. van Haesendonck, L. V. den Dries, Y. Bruynseraede, and A. Gilabert, "On the spatial dependence of the order parameter in superconducting proximity

sandwiches," *Journal of Physics F: Metal Physics*, vol. 11, no. 11, pp. 2381–2388, nov 1981. [Online]. Available: https://doi.org/10.1088/0305-4608/11/11/019

[198] H. Meissner, "Proximity effect between superconducting and normal metals," *Stevens Institute of Technology*, 1971. [Online]. Available: https://ntrs.nasa.gov/citations/19720004977

[199] J. Clarke, "The proximity effect between superconducting and normal thin films in zero field," *Journal de Physique Colloques*, vol. 29, no. C2, pp. C2–3–C2–16, 1968. [Online]. Available: https://hal.archives-ouvertes.fr/jpa-00213516

[200] C. Jünger, A. Baumgartner, R. Delagrange, D. Chevallier, S. Lehmann, M. Nilsson, K. A. Dick, C. Thelander, and C. Schönenberger, "Spectroscopy of the superconducting proximity effect in nanowires using integrated quantum dots," *Communications Physics*, vol. 2, no. 1, p. 76, 2019. [Online]. Available: https://doi.org/10.1038/s42005-019-0162-4

[201] W. L. McMillan, "Theory of superconductor—normal-metal interfaces," *Phys. Rev.*, vol. 175, pp. 559–568, Nov 1968. [Online]. Available: https://link.aps.org/doi/10.1103/PhysRev.175.559

[202] L. Gor'kov, "Energy spectrum of superconductors. [quantum field theory]," *Sov. Phys. - JETP (Engl. Transl.); (United States)*, vol. 7:3, 1 1958.

[203] Y. Nambu, "Quasi-particles and gauge invariance in the theory of superconductivity," *Phys. Rev.*, vol. 117, pp. 648–663, Feb 1960. [Online]. Available: https://link.aps.org/doi/10.1103/PhysRev.117.648

[204] G. Deutscher and P. de Gennes, "Proximity effects," *pp 1005-34 of Superconductivity. Vols. 1 and 2. Parks, R. D. (ed.). New York, Marcel Dekker, Inc., 1969.*, 10 1969.

[205] D. S. Falk, "Superconductors with plane boundaries," *Phys. Rev.*, vol. 132, pp. 1576–1590, Nov 1963. [Online]. Available: https://link.aps.org/doi/10.1103/PhysRev.132.1576

[206] H. van Houten and C. Beenakker, "Andreev reflection and the Josephson effect in a quantum point contact: An analogy with phase-conjugating resonators," *Physica B: Condensed Matter*, vol. 175, no. 1, pp. 187–197, 1991, analogies in Optics and Micro-Electronics. [Online]. Available: https://www.sciencedirect.com/science/article/pii/092145269190712N

[207] A. Martin and J. F. Annett, "The importance of self-consistency in determining interface properties of SIN and DIN structures," *Superlattices*

and Microstructures, vol. 25, no. 5, pp. 1019–1031, 1999. [Online]. Available: https://www.sciencedirect.com/science/article/pii/S0749603699907097

[208] J. Ridderbos, M. Brauns, F. K. de Vries, J. Shen, A. Li, S. Kölling, M. A. Verheijen, A. Brinkman, W. G. van der Wiel, E. P. A. M. Bakkers, and F. A. Zwanenburg, "Hard superconducting gap and diffusion-induced superconductors in Ge–Si nanowires," *Nano Letters*, vol. 20, no. 1, pp. 122–130, Jan 2020. [Online]. Available: https://doi.org/10.1021/acs.nanolett.9b03438

[209] W. S. Cole, S. Das Sarma, and T. D. Stanescu, "Effects of large induced superconducting gap on semiconductor Majorana nanowires," *Phys. Rev. B*, vol. 92, p. 174511, Nov 2015. [Online]. Available: https://link.aps.org/doi/10.1103/PhysRevB.92.174511

[210] J. Klinovaja and D. Loss, "Composite Majorana fermion wave functions in nanowires," *Phys. Rev. B*, vol. 86, p. 085408, Aug 2012. [Online]. Available: https://link.aps.org/doi/10.1103/PhysRevB.86.085408

[211] J. Osca and L. m. c. Serra, "Majorana modes in smooth normal-superconductor nanowire junctions," *Phys. Rev. B*, vol. 88, p. 144512, Oct 2013. [Online]. Available: https://link.aps.org/doi/10.1103/PhysRevB.88.144512

[212] S. Arabas, D. Jarecka, A. Jaruga, and M. Fijałkowski, "Formula translation in Blitz++, NumPy and modern Fortran: A case study of the language choice tradeoffs," *Scientific Programming*, vol. 22, p. 201–222, 2014.

[213] A. Kringhøj, G. W. Winkler, T. W. Larsen, D. Sabonis, O. Erlandsson, P. Krogstrup, B. van Heck, K. D. Petersson, and C. M. Marcus, "Andreev modes from phase winding in a full-shell nanowire-based transmon," *Phys. Rev. Lett.*, vol. 126, p. 047701, Jan 2021. [Online]. Available: https://link.aps.org/doi/10.1103/PhysRevLett.126.047701

[214] F. Maier, J. Klinovaja, and D. Loss, "Majorana fermions in Ge/Si hole nanowires," *Physical Review B*, vol. 90, no. 19, Nov 2014. [Online]. Available: http://dx.doi.org/10.1103/PhysRevB.90.195421

[215] Ö. Gül, H. Zhang, J. D. S. Bommer, M. W. A. de Moor, D. Car, S. R. Plissard, E. P. A. M. Bakkers, A. Geresdi, K. Watanabe, T. Taniguchi, and L. P. Kouwenhoven, "Ballistic Majorana nanowire devices," *Nature Nanotechnology*, vol. 13, no. 3, pp. 192–197, 2018. [Online]. Available: https://doi.org/10.1038/s41565-017-0032-8

[216] O. Millo and G. Koren, "What can Andreev bound states tell us about superconductors?" *Philos. Trans. Royal Soc. A*, vol. 376, no. 2125, p. 20140143, 2018.

[217] O. Erlandsson, D. Sabonis, A. Kringhøj, T. W. Larsen, P. Krogstrup, K. D. Petersson, and C. M. Marcus, "Parity switching in a full-shell superconductor-semiconductor nanowire qubit," 2022. [Online]. Available: https://arxiv.org/abs/2202.05974

[218] D. Sabonis, O. Erlandsson, A. Kringhøj, B. van Heck, T. W. Larsen, I. Petkovic, P. Krogstrup, K. D. Petersson, and C. M. Marcus, "Destructive Little-Parks effect in a full-shell nanowire-based transmon," *Phys. Rev. Lett.*, vol. 125, p. 156804, Oct 2020. [Online]. Available: https://link.aps.org/doi/10.1103/PhysRevLett.125.156804

[219] W. A. Little and R. D. Parks, "Observation of quantum periodicity in the transition temperature of a superconducting cylinder," *Phys. Rev. Lett.*, vol. 9, p. 9–12, Jul 1962. [Online]. Available: https://link.aps.org/doi/10.1103/PhysRevLett.9.9

[220] P. San-Jose, C. Payá, C. M. Marcus, S. Vaitiekėnas, and E. Prada, "Theory of Caroli-de Gennes-Matricon analogs in full-shell nanowires," 2022. [Online]. Available: https://arxiv.org/abs/2207.07606

[221] D. S. Golubović, W. V. Pogosov, M. Morelle, and V. V. Moshchalkov, "Little-Parks effect in a superconducting loop with a magnetic dot," *Phys. Rev. B*, vol. 68, p. 172503, Nov 2003. [Online]. Available: https://link.aps.org/doi/10.1103/PhysRevB.68.172503

[222] A. A. Eremko, L. S. Brizhik, and V. M. Loktev, "On the theory of the Schrödinger equation with the full set of relativistic corrections," *Low Temperature Physics*, vol. 44, no. 6, p. 573–583, 2018.

[223] B. Berche, E. Medina, and A. López, "Spin superfluidity and spin-orbit gauge symmetry fixing," *EPL (Europhysics Letters)*, vol. 97, no. 6, p. 67007, mar 2012. [Online]. Available: https://doi.org/10.1209/0295-5075/97/67007

[224] R. Gurtler and D. Hestenes, "Consistency in the formulation of the Dirac, Pauli, and Schrödinger theories," *Journal of Mathematical Physics*, vol. 16, no. 3, pp. 573–584, 1975. [Online]. Available: https://doi.org/10.1063/1.522555

[225] Y. A. Bychkov and É. I. Rashba, "Properties of a 2D electron gas with lifted spectral degeneracy," *Soviet Journal of Experimental and Theoretical Physics Letters*, vol. 39, p. 78, Jan. 1984.

[226] G. Dresselhaus, "Spin-orbit coupling effects in zinc blende structures," *Phys. Rev.*, vol. 100, pp. 580–586, Oct 1955. [Online]. Available: https://link.aps.org/doi/10.1103/PhysRev.100.580

[227] R. Winkler, *Spin-orbit Coupling Effects in Two-Dimensional Electron and Hole Systems*, ser. Springer Tracts in Modern Physics. Springer Berlin Heidelberg, 2003.

[228] H. Wu, D. W. L. Sprung, and J. Martorell, "Electronic properties of a quantum wire with arbitrary bending angle," *Journal of Applied Physics*, vol. 72, no. 1, pp. 151–154, 1992. [Online]. Available: http://scitation.aip.org/content/aip/journal/jap/72/1/10.1063/1.352176

[229] R. Ul Haq and L. H. Kauffman, "Z2 topological order and topological protection of Majorana fermion qubits," *Condensed Matter*, vol. 6, no. 1, 2021. [Online]. Available: https://www.mdpi.com/2410-3896/6/1/11

[230] E. Hitzer, C. Lavor, and D. Hildenbrand, "Current survey of Clifford geometric algebra applications," *Mathematical Methods in the Applied Sciences*, vol. n/a, no. n/a, 2022. [Online]. Available: https://onlinelibrary.wiley.com/doi/abs/10.1002/mma.8316

[231] E. Bayro-Corrochano, "A survey on quaternion algebra and geometric algebra applications in engineering and computer science 1995–2020," *IEEE Access*, vol. 9, p. 104326–104355, 2021.

[232] D. Hestenes, *A Unified Language for Mathematics and Physics.* Dordrecht: Springer Netherlands, 1986, pp. 1–23. [Online]. Available: https://doi.org/10.1007/978-94-009-4728-3_1

[233] W. E. Baylis, Ed., *Clifford (Geometric) Algebras.* Birkhäuser Boston, 1996. [Online]. Available: https://doi.org/10.1007%2F978-1-4612-4104-1

[234] G. Sobczyk, "Periodic table of geometric numbers," 2020. [Online]. Available: https://arxiv.org/abs/2003.07159

[235] M. Z. Hasan and C. L. Kane, "Colloquium: Topological insulators," *Rev. Mod. Phys.*, vol. 82, pp. 3045–3067, Nov 2010. [Online]. Available: https://link.aps.org/doi/10.1103/RevModPhys.82.3045

[236] C. Cafaro and S. Mancini, "A geometric algebra perspective on quantum computational gates and universality in quantum computing," *Advances in Applied Clifford Algebras*, vol. 21, no. 3, p. 493–519, feb 2011. [Online]. Available: https://doi.org/10.1007%2Fs00006-010-0269-x

[237] T. F. Havel and C. J. L. Doran, "Geometric algebra in quantum information processing," in *Quantum computation and information (Washington, DC, 2000)*, ser. Contemp. Math. Amer. Math. Soc., Providence, RI, 2002, vol. 305, p. 81–100. [Online]. Available: https://doi.org/10.1090/conm/305/05217

[238] Y. Sharf, D. G. Cory, S. S. Somaroo, T. F. Havel, E. Knill, R. Laflamme, and W. H. Zurek, "A study of quantum error correction by geometric algebra and liquid-state NMR spectroscopy," *Molecular Physics*, vol. 98, no. 17, p. 1347–1363, 2000. [Online]. Available: https://doi.org/10.1080/002689700413604

[239] S. S. Somaroo, D. G. Cory, and T. F. Havel, "Expressing the operations of quantum computing in multiparticle geometric algebra," *Physics Letters A*, vol. 240, no. 1-2, p. 1–7, mar 1998. [Online]. Available: https://doi.org/10.1016%2Fs0375-9601%2898%2900010-3

[240] C. Doran and A. Lasenby, *Geometric Algebra for Physicists*. Cambridge University Press, 2003.

[241] A. Macdonald, *Linear and Geometric Algebra*, ser. Geometric Algebra & Calculus. CreateSpace Independent Publishing Platform, 2010.

[242] J. Pozo and G. Sobczyk, "Geometric algebra in linear algebra and geometry," *Acta Applicandae Mathematicae*, vol. 71, pp. 207–244, 01 2002.

[243] D. Hestenes and G. Sobczyk, *Clifford algebra to geometric calculus: a unified language for mathematics and physics*. Springer Science & Business Media, 2012, vol. 5.

[244] A. Macdonald, *Vector and Geometric Calculus*, ser. Geometric Algebra & Calculus. CreateSpace Independent Publishing Platform, 2012.

[245] D. Hestenes, "Differential forms in geometric calculus," in *Clifford Algebras and their Applications in Mathematical Physics*, F. Brackx, R. Delanghe, and H. Serras, Eds. Dordrecht: Springer Netherlands, 1993, pp. 269–285.

[246] T. Alho, "Coordinate free integrals in geometric calculus," *Advances in Applied Clifford Algebras*, vol. 27, no. 1, pp. 423–437, Mar 2017. [Online]. Available: https://doi.org/10.1007/s00006-016-0655-0

[247] L. Burns, "Maxwell's equations are universal for locally conserved quantities," *Advances in Applied Clifford Algebras*, vol. 29, no. 4, p. 62, Jul 2019. [Online]. Available: https://doi.org/10.1007/s00006-019-0979-7

[248] H. Bhatia, G. Norgard, V. Pascucci, and P.-T. Bremer, "The Helmholtz-Hodge decomposition—A survey," *IEEE Transactions on Visualization and Computer Graphics*, vol. 19, no. 8, pp. 1386–1404, 2013.

[249] W. Sprössig, "On Helmholtz decompositions and their generalizations—An overview," *Mathematical Methods in the Applied Sciences*, vol. 33, no. 4, pp. 374–383, 2010. [Online]. Available: https://onlinelibrary.wiley.com/doi/abs/10.1002/mma.1212

[250] D. H. Kobe, "Helmholtz theorem for antisymmetric second-rank tensor fields and electromagnetism with magnetic monopoles," *American Journal of Physics*, vol. 52, no. 4, pp. 354–358, 1984. [Online]. Available: https://doi.org/10.1119/1.13668

[251] E. Cartan and M. Nadjafikhah, *É. Cartan - Exterior Differential Systems and its Applications - Translated form French in to English by M. Nadjafikhah*, 02 2014.

[252] R. Bott and L. Tu, *Differential Forms in Algebraic Topology*, ser. Graduate Texts in Mathematics. Springer New York, 2013.

[253] J. Harrison, "Stokes' theorem for nonsmooth chains," *Bulletin of the American Mathematical Society*, vol. 29, 09 1993.

[254] S. Gull, A. Lasenby, and C. Doran, "Imaginary numbers are not real— The geometric algebra of spacetime," *Foundations of Physics*, vol. 23, no. 9, pp. 1175–1201, Sep 1993. [Online]. Available: https://doi.org/10.1007/BF01883676

[255] Y. Huang and N. C. Leung, "A uniform description of compact symmetric spaces as Grassmannians using the magic square," *Mathematische Annalen*, vol. 350, no. 1, pp. 79–106, May 2011. [Online]. Available: https://doi.org/10.1007/s00208-010-0549-8

[256] D. Hestenes, *Space-Time Algebra*. Springer International Publishing, 2015.

[257] B. B. Mandelbrot and M. Frame, "A primer of negative test dimensions and degree of emtiness for latent sets," *Fractals*, vol. 17, no. 01, pp. 1–14, 2009. [Online]. Available: https://doi.org/10.1142/S0218348X09004211

[258] B. B. Mandelbrot, J. C. R. Hunt, O. M. Phillips, and D. Williams, "Random multifractals: Negative dimensions and the resulting limitations of the thermodynamic formalism," *Proc. R. Soc. A: Math. Phys. Eng. Sci.*, vol. 434, no. 1890, pp. 79–88, 1991.

[259] I. A. Taimanov, "Finite-gap theory of the Clifford torus," *International Mathematics Research Notices*, vol. 2005, no. 2, pp. 103–120, 01 2005. [Online]. Available: https://doi.org/10.1155/IMRN.2005.103

[260] M. Kilian, M. Schmidt, and N. Schmitt, "On stability of equivariant minimal tori in the 3-sphere," *Journal of Geometry and Physics*, vol. 85, pp. 171–176, 2014, geometry of Partial Differential Equations and Integrability. [Online]. Available: https://www.sciencedirect.com/science/article/pii/S0393044014000977

[261] S. Brendle, "Embedded minimal tori in S3 and the lawson conjecture," *Acta Mathematica*, vol. 211, no. 2, pp. 177–190, Dec 2013. [Online]. Available: https://doi.org/10.1007/s11511-013-0101-2

[262] P. G. Tait, *Lectures on some recent advances in physical science*. London, Macmillan and co., 1876. [Online]. Available: https://archive.org/details/cu31924012325100/page/n313/mode/2up

[263] K. Klausen, *A Treatise on the Magnetic Vector Potential*. Springer International Publishing, 2020.

[264] B. Leurs, Z. Nazario, D. Santiago, and J. Zaanen, "Non-Abelian hydrodynamics and the flow of spin in spin–orbit coupled substances," *Annals of Physics*, vol. 323, no. 4, pp. 907–945, 2008. [Online]. Available: https://www.sciencedirect.com/science/article/pii/S0003491607000863

[265] J. M. Chappell, S. P. Drake, C. L. Seidel, L. J. Gunn, A. Iqbal, A. Allison, and D. Abbott, "Geometric Algebra for Electrical and Electronic Engineers," *Proceedings of the IEEE*, vol. 102, no. 9, p. 1340–1363, 2014.

[266] C. Cafaro and S. Ali, "The Spacetime Algebra Approach to Massive Classical Electrodynamics with Magnetic Monopoles," *Advances in Applied Clifford Algebras*, vol. 17, p. 23–36, 01 2007.

[267] W. M. Pezzaglia, *Clifford Algebra Derivation of the Characteristic Hypersurfaces of Maxwell's Equations*. Dordrecht: Springer Netherlands, 1994, p. 129–134. [Online]. Available: https://doi.org/10.1007/978-94-011-1896-5_4

[268] J. C. Baez, "The octonions," *Bull. Am. Math. Soc.*, vol. 39, pp. 145–205, 2002.

[269] A. Lasenby, "Some recent results for $SU(3)$ and octonions within the geometric algebra approach to the fundamental forces of nature," 2022. [Online]. Available: https://arxiv.org/abs/2202.06733

[270] C. Doran, D. Hestenes, F. Sommen, and N. Van Acker, "Lie groups as spin groups," *Journal of Mathematical Physics*, vol. 34, no. 8, pp. 3642–3669, 1993. [Online]. Available: https://doi.org/10.1063/1.530050

[271] R. Chacon and A. Fomenko, "Stokes' formula for Lie algebra valued connection and curvature forms," *Advances in Mathematics*, vol. 88, no. 2, pp. 258–300, 1991. [Online]. Available: https://www.sciencedirect.com/science/article/pii/000187089190009V

[272] B. Broda, "Non-Abelian Stokes theorem in action," *arXiv e-prints*, pp. math–ph/0 012 035, Dec. 2000.

[273] F. V. Gubarev, "Non-Abelian Stokes theorem for SU(2) gauge fields," *Physical Review D*, vol. 69, no. 11, jun 2004. [Online]. Available: https://doi.org/10.1103%2Fphysrevd.69.114502

[274] M. Hirayama and S. Matsubara, "Stokes theorem for loop variables of non-Abelian gauge field," *Progress of Theoretical Physics*, vol. 99, no. 4, pp. 691–706, 04 1998. [Online]. Available: https://doi.org/10.1143/PTP.99.691

[275] M. Hirayama and M. Ueno, "Non-Abelian Stokes theorem for Wilson loops associated with general gauge groups," *Progress of Theoretical Physics*, vol. 103, no. 1, pp. 151–159, jan 2000. [Online]. Available: https://doi.org/10.1143%2Fptp.103.151

[276] M. Hirayama, M. Kanno, M. Ueno, and H. Yamakoshi, "Non-Abelian Stokes theorem for loop variables associated with nontrivial loops," *Progress of Theoretical Physics*, vol. 100, no. 4, pp. 817–830, oct 1998. [Online]. Available: https://doi.org/10.1143%2Fptp.100.817

[277] I. Y. Aref'eva, "Non-Abelian Stokes formula," *Theoretical and Mathematical Physics*, vol. 43, no. 1, pp. 353–356, Apr 1980. [Online]. Available: https://doi.org/10.1007/BF01018469

[278] G. Abramovici and P. Kalugin, "Clifford modules and symmetries of topological insulators," *International Journal of Geometric Methods in Modern Physics*, vol. 09, no. 03, p. 1250023, 2012. [Online]. Available: https://doi.org/10.1142/S0219887812500235

Appendix A

Periodic Table of Topological Invariants and Cartan Labels

Symmetry	T^2	P^2	C^2	d=0	1	2	3	4	5	6	7
A	0	0	0	$\mathbb{Z}$	0	$\mathbb{Z}$	0	$\mathbb{Z}$	0	$\mathbb{Z}$	0
AIII	0	0	1	0	$\mathbb{Z}$	0	$\mathbb{Z}$	0	$\mathbb{Z}$	0	$\mathbb{Z}$
AI	+1	0	0	$\mathbb{Z}$	0	0	0	$2\mathbb{Z}$	0	$\mathbb{Z}_2$	$\mathbb{Z}_2$
BDI	+1	+1	0	$\mathbb{Z}_2$	$\mathbb{Z}$	0	0	0	$2\mathbb{Z}$	0	$\mathbb{Z}_2$
D	0	+1	0	$\mathbb{Z}_2$	$\mathbb{Z}_2$	$\mathbb{Z}$	0	0	0	$2\mathbb{Z}$	0
DIII	-1	+1	0	0	$\mathbb{Z}_2$	$\mathbb{Z}_2$	$\mathbb{Z}$	0	0	0	$2\mathbb{Z}$
AII	-1	0	0	$2\mathbb{Z}$	0	$\mathbb{Z}_2$	$\mathbb{Z}_2$	$\mathbb{Z}$	0	0	0
CII	-1	-1	1	0	$2\mathbb{Z}$	0	$\mathbb{Z}_2$	$\mathbb{Z}_2$	$\mathbb{Z}$	0	0
C	0	-1	0	0	0	0	$2\mathbb{Z}$	0	$\mathbb{Z}_2$	$\mathbb{Z}_2$	$\mathbb{Z}$
CI	+1	-1	1	0	0	0	$2\mathbb{Z}$	0	$\mathbb{Z}_2$	$\mathbb{Z}_2$	$\mathbb{Z}$

Table A.1: Classification of topological invariants in terms of Cartan symmetry labels **A-D**, see further Table A.2, and dimension d [84, 161]. The symmetry labels T, P, C respectively denote time reversal, particle-hole and chiral symmetry. The table repeats for dimensions above seven due to Bott periodicity.

Cartan label	$Cl_{p,q}$ extension	Classifying space X	$\pi_0(X)$
A	$C_d^{\mathbb{C}} \to C_{d+1}^{\mathbb{C}}$	$(U(N)/(U(k) \times U(m))) \times \mathbb{Z}$	$\mathbb{Z}$
AIII	$C_{d+1}^{\mathbb{C}} \to C_{d+2}^{\mathbb{C}}$	$U(N)$	0
AI	$C_{d+1,1} \to C_{d+1,2}$	$(O(N)/(O(k) \times O(m))) \times \mathbb{Z}$	$\mathbb{Z}$
BDI	$C_{0,d+1} \to C_{1,d+1}$	$O(N)$	$\mathbb{Z}_2$
D	$C_{0,d} \to C_{1,d}$	$O(2N)/U(N)$	$\mathbb{Z}_2$
DIII	$C_{1,d} \to C_{2,d}$	$U(2N)/Sp(N)$	0
AII	$C_{2,d} \to C_{3,d}$	$(Sp(N)/(Sp(k) \times Sp(m))) \times \mathbb{Z}$	$\mathbb{Z}$
CII	$C_{d+3,0} \to C_{d+3,1}$	$Sp(N)$	0
C	$C_{d+2,0} \to C_{d+2,1}$	$Sp(N)/U(N)$	0
CI	$C_{d+2,1} \to C_{d+2,2}$	$U(N)/O(N)$	0

Table A.2: Cartan symmetry labels **A**-**D** in terms of Clifford algebra extensions for Dirac operators [278], classifying space X and its zeroth fundamental homotopy group π_0 [84, 161]. The symmetry of the classifying space denotes $N \times N$ Hermitian matrices with m positive and k negative unit eigenvalues. For generality $N \to \infty$.

Appendix B

List of Publications

1. Klausen, K.O., Sitek, A., Erlingsson, S.I., and Manolescu, A. (2020). Majorana Zero Modes in Nanowires with Combined Triangular and Hexagonal Geometry. *Nanotechnology* 31, 354001. DOI: 10.1088/1361-6528/ab932e

2. Klausen, K.O. (2020). Theory of Superconductivity. In: A Treatise on the Magnetic Vector Potential. *Springer, Cham.* DOI: 10.1007/978-3-030-52222-3_5

3. Torres, M.U., Klausen, K.O., Sitek, A., Erlingsson, S.I., and Manolescu, A. (2021) Electromagnetic field emitted by core–shell semiconductor nanowires driven by an alternating current. *Journal of Applied Physics* 130, 034301.
DOI: 10.1063/5.0055260

4. Klausen, K.O., Sitek, A., Erlingsson, S.I., and Manolescu, A. (2022). Electron-hole coherence in core-shell nanowires with partial proximity induced superconductivity. *arXiv*. DOI: 10.48550/arXiv.2206.04830

5. Klausen, K.O. (2022). Visualizing Stokes' theorem with Geometric Algebra. *arXiv*. DOI: 10.48550/arXiv.2206.07177

6. Klausen, K.O., Sitek, A., Erlingsson, S.I., and Manolescu, A. (2022). Flux-periodic oscillations in proximitized core-shell nanowires. *arXiv*.
DOI: 10.48550/arXiv.2209.13076

arXiv DOI are provided for papers in the publishing process at the time of writing.